



FEDERAL UNIVERSITY OF SANTA CATARINA
MATERIALS SCIENCE AND ENGINEERING GRADUATE PROGRAM (PGMAT)

Ruben Bentes de Oliveira Acevedo

**Production of Ti-6Al-4V – Stainless Steel 316L auxetic structures using Selective
Laser Melting (SLM) for high energy impact absorption applications**

Florianópolis

2020

Ruben Bentes de Oliveira Acevedo

**Production of Ti-6Al-4V – Stainless Steel 316L auxetic structures using Selective
Laser Melting (SLM) for high energy impact absorption applications**

Thesis subjected to the Graduate Program in
Materials Science and Engineering from the
Federal University of Santa Catarina to
obtain the degree Doctor of Philosophy
(PhD) in Materials Science and Engineering.
Advisor/Brazil: Prof. Dr. Márcio C. Fredel
Co-Advisor/Brazil: Dr. Edson Costa Santos

Florianópolis

2020

Work identification sheet

Ficha de identificação da obra elaborada pelo autor,
através do Programa de Geração Automática da Biblioteca Universitária da UFSC.

Acevedo, Ruben

Production of Ti-6Al-4V - Stainless Steel 316L auxetic structures using Selective Laser Melting (SLM) for high energy impact absorption applications / Ruben Acevedo ; orientador, Márcio Celso Fredel, coorientador, Edson Costa Santos, 2021.

168 p.

Tese (doutorado) - Universidade Federal de Santa Catarina, Centro Tecnológico, Programa de Pós-Graduação em Ciência e Engenharia de Materiais, Florianópolis, 2021.

Inclui referências.

1. Ciência e Engenharia de Materiais. 2. Selective Laser Melting. 3. Ti-6Al-4V. 4. Auxetic materials . 5. High energy applications . I. Fredel, Márcio Celso. II. Costa Santos, Edson. III. Universidade Federal de Santa Catarina. Programa de Pós-Graduação em Ciência e Engenharia de Materiais. IV. Título.

Ruben Bentes de Oliveira Acevedo

**Production of Ti-6Al-4V - SS auxetic structures using Selective Laser Melting (SLM)
for High Energy impact absorption applications**

O presente trabalho em nível de doutorado foi avaliado e aprovado por banca examinadora composta pelos seguintes membros:

Prof. Dr. Carlos Pérez Bergmann

UFRGS

Prof. Dr. Dachamir Hotza

UFSC

Prof. Dr. Eduardo Sousa Lima,

IME

Certificamos que esta é a **versão original e final** do trabalho de conclusão que foi julgado adequado para obtenção do título de doutor em Engenharia de Materiais.

Prof. Dr. João Batista Rodrigues Neto

Coordenador do Programa

Prof. Dr. Márcio Celso Fredel

Orientador

Florianópolis, 2020.

A mi madre, Rosa Acevedo, por la inspiración, alegrías y continua motivación.

Pour ma petite lionne Isis, son amour et son sourire mignon.

Дорогой длиною, Победа!

Solomon saith. There is no new thing upon the earth. So that as Plato had an imagination, that all knowledge was but remembrance; so Solomon giveth his sentence, that all novelty is but oblivion.

Francis Bacon: Essays LVIII

Cualquier destino, por más largo y complicado que sea, en realidad consiste en un solo momento: el que el hombre finalmente comprende quién es.

Jorge Luis Borges Acevedo: Funes el memorioso

ACKNOWLEDGEMENTS

Márcio Celso Fredel, Edson Costa Santos, Radek Kolman, Jiří Plešek, Jaroslav Joch, Guilherme Mariz de Oliveira Barra, Celso Peres Fernandes, Petr Sedlak, Jan Trnka and Zdenek Prevorovsky, for guidance and important teachings.

My family gave me a strong support, especially my father Anselmo Oliveira, my aunt Dilia Acevedo de González, my uncle Roberto Dall’Agnol for his wisdom, and, my great guide Nirvia Ravena. Friends for the good times and great learning at different times and places: Gabriela Corazza, Martina Novakova, Evgeniya Voronova, Arthur Grimaldi, Cesar Stupp, Fernando Machuca, Useche Inchauspe, Rogerio Campos, Rafael Veit, Rafael Pereira, Marcelo Barros, Chandra Prasad, Patrik Zima, Henrique Oliveira and Anderson Camargo.

I would like to thank my home institution UFSC, as well as the Institute of Thermomechanics of the Czech Academy of Sciences (IT-CAS), State University of Santa Catarina (UDESC), and Serviço Nacional da Indústria – Instituto SENAI de Inovação Laser (SENAI-ISI) Santa Catarina.

After the oral presentation of this work, which occurred on the 27th October 2020, I would like to especially thanks to the examination board Prof. Dr. Eduardo Sousa Lima, Prof. Dr. Dachamir Hotza and Prof. Dr. Carlos Pérez Bergmann, for their contribution to the advance of this research.

My graduation and PhD studies were carried out at the Federal University of Santa Catarina, with fundamental scholarships from CNPq and CAPES. These scientific institutions are essential for the maintenance of science development in Brazil, and they need to be defended against the will of mediocre governments which deliberately attack science.

RESUMO

Selective Laser Melting (SLM) é atualmente um dos métodos mais promissores em AM. O princípio do SLM é de sinterizar e fundir o pó camada por camada usando um feixe de laser. Esse processo traz várias possibilidades, como uma ampla gama de geometrias que podem ser produzidas, rápida fabricação, elevada precisão dimensional e alta densificação dos componentes, no entanto, ocorre a criação de grandes estresses residuais (RS). Por outro lado, materiais e estruturas auxéticas apresentam uma série de características originais (coeficiente de Poisson negativo - NPR, aprimorada resistência à indentação, elevado módulo de cisalhamento), o que torna essa classe de materiais bastante única. Entretanto, uma parte significativa da pesquisa em auxéticos ocorre com maior intensidade nos polímeros, tanto pela facilidade da obtenção dessa propriedade, quanto pela elevada disponibilidade de métodos de fabricação. Até o presente, pouco tem sido investigado sobre estruturas auxéticas metálicas obtidos por SLM. Associando as propriedades diferenciadas das ligas de titânio a geometrias com propriedades auxéticas, a fabricação por SLM permite obter diversas aplicações. O objetivo principal desta pesquisa é simular e manufaturar estruturas auxéticas baseadas em liga de Ti-6Al-4V por SLM. Enquanto prioridade secundária, vem a formulação de aplicações em absorção de impactos de alta energia. Resultados prévios de simulação numérica demonstraram o grande potencial da pesquisa em auxéticos: um projétil de calibre 7.62 mm com velocidade entre 100 m/s até 400 m/s pode ser totalmente neutralizado por uma estrutura auxética fabricada em Ti-6Al-4V.

Palavras-chave: SLM, Materiais Auxéticos, Titânio, Ti-6Al-4V, Aplicações em absorção de impactos de alta energia.

RESUMO EXPANDIDO

Introdução

A Manufatura Aditiva (AM) é um tema de pesquisa de ponta, com especial destaque para técnicas que permitem a produção de peças a partir de diferentes tipos de materiais (cerâmicas, metais, polímeros). Esses processos trazem a flexibilidade de criar estruturas complexas com propriedades mecânicas muito semelhantes às peças obtidas por métodos convencionais de fabricação. Dentre essas técnicas de AM, que podem fabricar protótipos e componentes mecânicos, algumas podem ser citadas (YADROITSEV, 2007): Sinterização Seletiva a Laser (SLS); Fusão seletiva a laser (SLM); Fusão de feixe de elétrons (EBM).

A fusão seletiva a laser (SLM) é uma das técnicas incluídas nos processos conhecidos anteriormente como Prototipagem Rápida (RP). Esta técnica foi desenvolvida na década de 90 no Fraunhofer ILT, uma década após a invenção da Sinterização Seletiva a Laser (SLS). O aparelho SLM convencional é mostrado na Figura 1 (TUCK, 2015): esta configuração básica é observada em máquinas de primeira geração e protótipos experimentais.

A flexibilidade do método SLM permite a fabricação de estruturas complexas à base de Ti-6Al-4V, as quais seriam difíceis de obter utilizando técnicas convencionais de fabricação, como metalurgia do pó e sinterização autopropagada de alta temperatura - SHS (AGRIPA, 2019). Ao alterar a geometria da estrutura, várias propriedades podem ser alteradas, incluindo resistência à força, tensão de escoamento e coeficiente de Poisson. Quando este último parâmetro torna-se negativo (Razão de Poisson Negativa), várias características e recursos aparecem: maior resistência à compressão; expansão em todas as dimensões sob tração.

As peças e materiais que contêm essa propriedade - Razão de Poisson Negativa (NPR) - são chamados de auxéticos. Até o momento, as estruturas e materiais auxéticos vêm adquirindo grande interesse em diversos campos de pesquisa: biomateriais; absorção de ruído; esportes; armaduras balísticas; aeronáutica e espacial; sensores (MEENA, 2019; YANG, 2017). Esta nova era de pesquisa para estruturas auxéticas é fortemente impulsionada pelo crescimento e disponibilidade de técnicas de AM (MEENA, 2019)

No escopo deste trabalho de pesquisa, uma armadura auxética protetora é proposta. Esta armadura tem um design de sanduíche composto por três camadas (cerâmica dura / estrutura auxética / Kevlar). Como uma alternativa importante aos componentes convencionais de defesa balística passiva, este sistema deve suportar o impacto de vários projéteis. Nesse sentido, duas questões de pesquisa foram elaboradas para compreender o desempenho de estruturas auxéticas: como essas estruturas auxéticas podem ser otimizadas? E como os parâmetros geométricos podem ser explorados para aumentar o NPR?

Para responder a esta questão de pesquisa e testar esta hipótese, foram estabelecidos objetivos gerais e específicos para atingir essas metas particulares.

Objetivos

O objetivo geral desta pesquisa é o seguinte: Criação, simulação e otimização de estruturas auxéticas utilizando o software de design 3D e simulação mecânica COMSOL e ANSYS

19.

Enquanto objetivos específicos para comprovar a hipótese de pesquisa: Fabricação de estruturas auxéticas por SLM a partir de Ti-6Al-4V e pó de aço inoxidável 316L; Caracterização de amostras auxéticas: análise microestrutural, ensaios mecânicos e XCT; Otimização dos parâmetros da estrutura para aumentar o desempenho em ensaios mecânicos, principalmente em compressão; Desenvolvimento de novas estruturas auxéticas visando alta resistência à compressão; Criação, simulação e otimização de modelos de armadura composta balística; Caracterização de amostras de armadura composta: testes mecânicos; testes balísticos.

Metodologia

Para atingir os objetivos desta pesquisa, propõe-se a seguinte metodologia:

A. Investigação bibliográfica no estado da arte atual em fusão seletiva a laser (SLM), Ti-6Al-4V, aço inoxidável e estruturas e materiais auxéticos: contexto e pesquisa atual na área.

B. Simulação e modelagem de estruturas auxéticas: com base no levantamento bibliográfico realizado na etapa A, diversas geometrias auxéticas são testadas quanto ao seu desempenho, utilizando os softwares de simulação mecânica COMSOL e ANSYS 19.

Como este é o último nível antes da produção de amostras (etapa C), um grande número de estruturas auxéticas deve ser completamente testado e ajustado para absorver o máximo de energia como parte de um sistema inovador de armadura balística.

C. Produção de peças de aço inoxidável Ti-6Al-4V e 316L usando SLM: seguindo a pesquisa e otimização de estruturas auxéticas na etapa B, os protótipos são fabricados usando CL20ES (ConceptLaser) e pós metálicos Ti64 (Tekna) descritos nas tabelas 18 e 19, respectivamente. De acordo com a disponibilidade da máquina e orçamento do projeto, várias amostras foram construídas em dois equipamentos SLM diferentes do SENAI ISI LASER: M2 Cusing (Figura 55 (a)) - esta máquina possui uma câmara de fabricação maior (250x250x280 mm) e foi usada para obter amostras SS316L - e SLM 125HL (Figura 55 (b)), que é totalmente dedicado à fabricação de Ti e possui uma câmara de fabricação mais compacta (125x125x125 mm), o que implica em um menor consumo de gás inerte (Argônio ou Hélio), otimizando custos de fabricação.

D. Caracterização de amostras (Difração de Raios-X; testes mecânicos; micro tomografia computadorizada (XCT) e microscopia eletrônica (Microscopia Eletrônica de Varredura - MEV): diversas análises foram realizadas para explorar microestrutura, fases, porosidade e propriedades mecânicas das peças fabricadas no item C. Por outro lado, caracterização mecânica como compressão estática usando uma máquina de ensaio universal (UTM) de bancada EMIC modelo DL 3000 (Figura 57 (a)) e testes dinâmicos (barra de divisão Hopkinson - Figura 57 (b)). a porosidade e densidade das amostras auxéticas são realizadas pelo método de Arquimedes: primeiro, o peso da amostra é medido no ar por uma balança Mettler-Toledo New Classic MS (Figura 57 (c)), e então, o peso em líquido (água) é obtido.

E. Otimização do modelo: com base nos itens B, C e D, os modelos geométricos e parâmetros SLM serão otimizados usando ANSYS 19, a fim de obter parâmetros que forneçam as propriedades mecânicas especificadas em nossa aplicação de armadura auxética (absorção de impacto de alta energia).

F. Outras aplicações: além do campo balístico, as inovações estão previstas para ocorrer também na área biomédica.

G. Realizar análise dos dados coletados, identificando a eficácia da metodologia proposta aplicada. Vários aspectos das amostras foram considerados: densidade, resistência mecânica, coeficiente de Poisson e limite de escoamento. Esses resultados foram comparados com os achados da literatura atual.

Resultados e discussão

Seguindo os resultados dos testes de compressão Ansys 17 com STR2 (Figura 68), novas geometrias foram investigadas visando um melhor desempenho mecânico e menos pontos de singularidades. Após este levantamento da literatura, uma nova estrutura auxética reentrante foi considerada com atenção - STR3. Foi apresentado pela primeira vez em um artigo de Evans et al (EVANS, 1994): apresenta grande facilidade de parametrização, propriedades mecânicas ajustáveis, alta compatibilidade de produção com a maioria dos processos AM, principalmente SLM e EBM. Em seguida, como os resultados das simulações preliminares demonstraram um grande potencial no regime elástico, o objeto de estudo foi finalmente determinado (Figura 69).

Finalizada a parametrização do STR3, vários testes no regime estático foram feitos para medir o coeficiente de Poisson. Nesse sentido, os parâmetros ideais para criar uma estrutura altamente auxética seriam $H / L = 4$ e $W = 0,1$ mm. Porém, à medida que as bielas se tornam mais finas, a fragilidade e a flexão são mais propensas a ocorrer, trazendo a necessidade de um maior entendimento sobre o comportamento de deformação (Figura 73). Uma parede mais espessa, na faixa $[0,3, 0,5]$ mm e $H / L = 2$, produz uma estrutura com desempenho auxético pronunciado (Figura 71, curvas em azul escuro e vermelho) e tem ganho significativo na resistência à compressão.

Como os testes estáticos provaram resultados satisfatórios, uma curta série de simulações dinâmicas foi implementada usando os seguintes parâmetros geométricos: $H / L = 2$; $w = 1$ mm e $\theta = 24^\circ$. Por meio do LSDYNA, um pacote de mecânica dinâmica do software ANSYS 19, é possível criar ensaios de lapso de tempo semelhantes aos testes balísticos. Nesta série de simulações, o STR3 - acoplado a uma placa fina de aço inoxidável - foi usado como peça de tiro para um cartucho de calibre padrão 7,62x39 mm, um padrão em fuzis AK-47 (ROSOBORONEXPORT, 2021), com massa de 9,0 g . Para velocidades iniciais abaixo ou iguais a 400 m / s (Figura 74 (a)), STR3 é capaz de absorver toda a energia de impacto e parar com sucesso a bala de 7,62x39 mm. Além disso, à medida que a velocidade do projétil aumenta, a deformação atinge níveis críticos, levando a danos progressivos das escoras (Figura 74 (b) e (c)) e, por fim, à falha mecânica do STR3 (Figura 74 (d)).

Considerações finais

As simulações ANSYS 19 do auxético Ti-6Al-4V STR3 apresentaram resultados promissores: um valor mínimo de $v = -5.75$ pode ser facilmente obtido definindo $H / L = 2.5$ e $W = 1$ mm, para $\theta = 12^\circ$. Além disso, a partir de nossas simulações de impacto balístico, STR3 foi capaz de absorver totalmente a energia de um projétil de 7.62 mm viajando a uma velocidade máxima de 400 m / s. Após este limite, STR3 sofre severa deformação plástica e a integridade mecânica fica comprometida.

Portanto, a hipótese formulada na Introdução (seção 1) foi confirmada: as estruturas auxéticas podem ser otimizadas e os parâmetros geométricos têm forte influência no NPR.

Conforme mencionado anteriormente, o processo de ensaios mecânicos ocorreu principalmente por meio de simulações numéricas, produzindo resultados que contribuíram para a demonstração de que a estrutura do STR3 possui propriedades auxéticas e grande potencial para aplicações balísticas.

Esta pesquisa representa uma contribuição para um tema bastante promissor, tanto no que diz respeito à tecnologia quanto à inovação. Diversas aplicações podem ser desenvolvidas, especialmente para resolver problemas práticos em aplicações balísticas.

A continuação desta pesquisa seguirá em diferentes frentes: novas geometrias auxéticas; simulações avançadas para verificar as propriedades dessas novas estruturas; otimização adicional de estruturas auxéticas; testes mais estáticos e dinâmicos, especialmente em relação à fadiga de alto ciclo e testes de canhões Taylor. Além disso, novas estruturas auxéticas Ti-6Al-4V otimizadas via simulação e experimentos serão produzidos usando SLM. Os parâmetros do processo serão revisados com o objetivo de melhorar o desempenho mecânico para aplicações balísticas.

Palavras-chave: SLM, Materiais Auxéticos, Titânio, Ti-6Al-4V, Aplicações em absorção de impactos de alta energia.

ABSTRACT

Selective Laser Melting (SLM) figures as one of the most promising Additive Manufacturing (AM) methods at present day. The principle of SLM is to sinter and melt powder layer by layer using a laser beam. This process brings many possibilities, such as a vast range of geometries that can be produced, rapid fabrication, high dimensional accuracy and high densification of parts, nevertheless, a significant amount of Residual Stresses (RS) are created. On the other hand, auxetic materials present a series of peculiar properties (Negative Poisson Ratio - NPR, enhanced indentation resistance, increased shear modulus), which make this class of materials very unique. Still, most of the research in auxetics is more intensive in polymers, because of the ease to obtain this property. Up to date, very little research has been done in auxetic metallic materials produced by SLM. Because of their unique combination of mechanical, physical and chemical properties, Titanium alloys represent a promising research subject. It is known that parts containing Ti and alloys are more easily fabricated using SLM. Associating titanium alloys unique properties with the proper geometries that lead to auxetic properties, SLM method can be used to create several applications. The first aim of this research is to simulate and manufacture re-entrant auxetic structures composed of Titanium - Ti-6Al-4V using SLM. The second aim is to formulate high energy absorption impact applications. Preliminary numerical simulation results illustrate the great potential of auxetics research: a 7.62 mm projectile traveling between 100 m/s to 400 m/s can be completely suppressed by a single Ti-6Al-4V auxetic structure.

Keywords: SLM, Auxetic materials, Titanium, Ti-6Al-4V, high energy absorption impact applications, Residual Stresses (RS).

Graphical Abstract

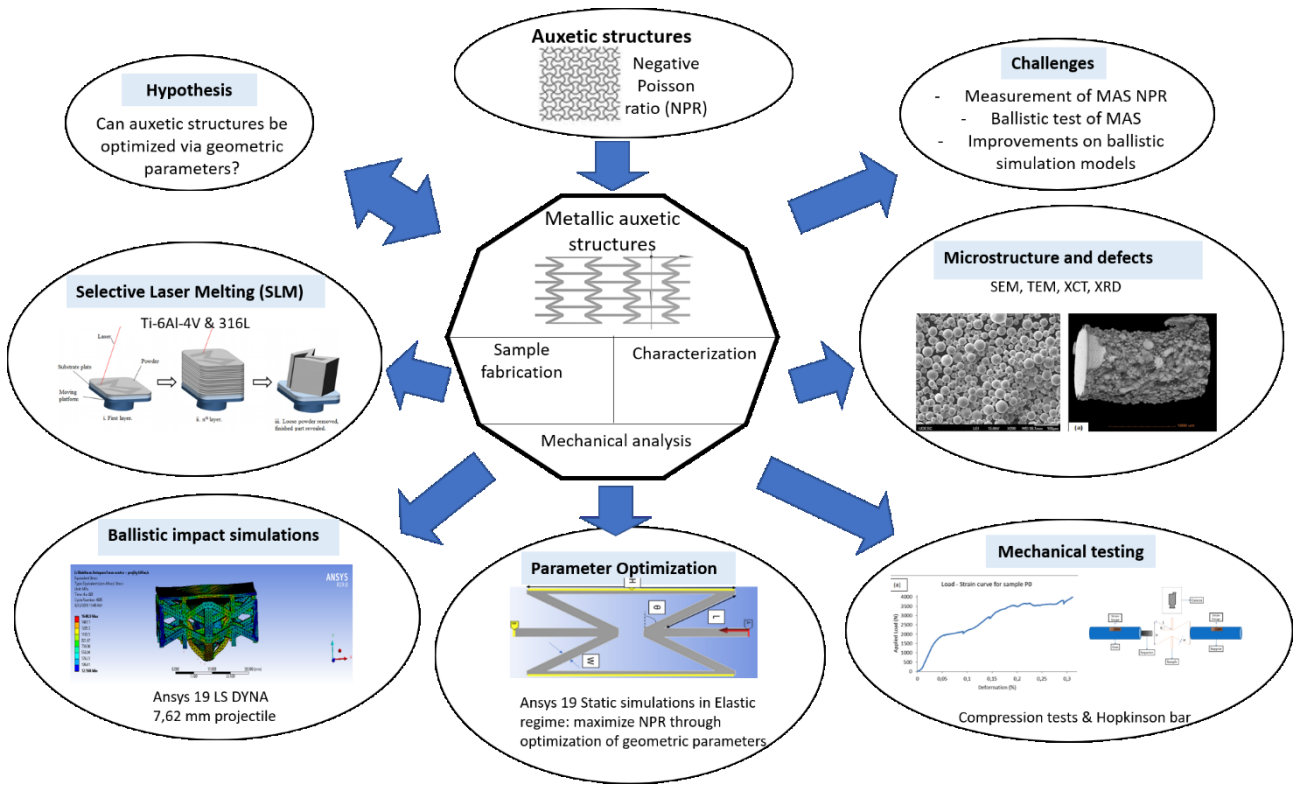


FIGURE INDEX

Figure 1 – Typical setup of a SLM machine.	22
Figure 2 – Typical setup of a SLM machine with preheating laser	23
Figure 3 – Hybrid CO ₂ laser - resistive element preheating mechanism	24
Figure 4 – Formation of object in SLM.	24
Figure 5 – Powder fusion process by a laser source.	25
Figure 6 – SLM structures, showing different lattice types.	26
Figure 7 – Airbus A320 fabricated with DMLS.	27
Figure 8 – Ti-6Al-4V phase diagram.	29
Figure 9 – a) Specific mechanical strength of Titanium alloys compared to other metals and CFRP; b) High-cycle fatigue of Ti-6Al-4V for different fabrication methods.	31
Figure 10 – Mechanical properties of Ti-6Al-4V samples produced by SLM, Powder Metallurgy (PM) and Wrought.	33
Figure 11 – Oriented martensite plates containing acicular hcp phase in SLM processed Ti-6Al-4V (a) and (c); (b) and (d) $\alpha - \beta$ microstructure in heat treated material.	34
Figure 12 – Parts fabricated by SLM.	35
Figure 13 – Stainless steel alloys and correspondent properties.	36
Figure 14 – Typical $v - \epsilon$ compression strain curve for a textile material (Simulation, Experiment and geometrical analysis).	39
Figure 15 – Mechanical behavior of (a) non-auxetic material and (b) auxetic material.	40
Figure 16 – Reentrant structures containing the auxetic effect.	41
Figure 17 – Comparison between a conventional material and an auxetic material under a specific applied load.	42
Figure 18 – Nike Knit auxetic sole.	43
Figure 19 – Metallic prosthesis showing displacement of the component after total shoulder arthroplasty.	44
Figure 20 – At left auxetic CAD models; in the right, EBM Ti-6Al-4V – Cu auxetic structures.	46
Figure 21 – Surface of EBM struts from auxetic structures.	47
Figure 22 – Stress - Strain curves for two different Ti-6Al-4V structures (D1 and D2).	48
Figure 23 – Failure behavior of EBM auxetic sample based on Ti-6Al-4V.	48
Figure 24 – EBM auxetic structures based on Ti-6Al-4V.	49
Figure 25 – Auxetic designs specifications.	50
Figure 26 – Stress - strain curves for different auxetic structures.	51
Figure 27 – Auxetic composite armor a) Dependency of the structure on the procedural parameters; b) Procedure of the powder laser scanning.	52
Figure 28 – Optimal SLM parameters: laser power, layer thickness and scan speed.	55
Figure 29 – a) Melting mechanisms related to process parameters; b) Laser scanning trajectory.	56
Figure 30 – Melting zones of Ti-6Al-4V.	57
Figure 31 – Optical absorption (%) of selected metals versus wavelength.	58
Figure 32 – Scanning strategies used in SLM TGM mechanism (a) - (c); Crack formation and delamination due to TGM (d) and (e).	59
Figure 33 – SLM support types: cone form (a); teeth form (b); cellular (c); lattice (d); I/IY (e).	62
Figure 34 – Laser beam reflection and absorption path in powder; Brownian motion.	63

Figure 35 – Heat transfer during SLM process of metals.	65
Figure 36 – TGM (a) – (c): crack formation and delamination due to TGM (d) and (e).	66
Figure 37 – Effects of Residual Stress in materials.	67
Figure 38 – TGM: Stresses and deformation during heating (a) and cooling down (b) in the irradiated zone.	68
Figure 39 – RS measurement techniques.	71
Figure 40 – RS measurement of samples by ultrasonic-based NDT.	73
Figure 41 – Defect detection using ultrasonic signals.	74
Figure 42 – Spatial resolution and penetration of different measurement techniques.	75
Figure 43 – Island scanning strategy for Inconel 718 parts.	76
Figure 44 – Density (a) and porosity (b) curves at different scan rate values.	80
Figure 45 – Hardness - scan rate behavior of SLM made Ti-6Al-4V parts.	80
Figure 46 – Influence of scan rate on densification for different layer thicknesses.	81
Figure 47 – Attainable density according to different scanning strategies (a); scanning strategies examples (b).	82
Figure 48 – Scan strategies: (a) lines scanning using antiparallel stripes [LS]; (b) Island scanning using PIR stripes [IS-PIR]; (c) Island scanning using random patterns [IS-RP]..	83
Figure 49 – Microstructure of as-built samples: (a) scan lines; (b) island scan PIR stripes; (c) island scan random patterns.	85
Figure 50 – Density dependency on scanning velocity and laser power for SLM made AlSi10Mg samples.	86
Figure 51 – Density behavior of Ti-6Al-4V parts processed by SLM with laser power and scanning speed.	87
Figure 52 – Norsk RPD process.	89
Figure 53 – Schematics of calculation mesh using bar elements.	92
Figure 54 – Stress concentration in joints of a plane wing.	93
Figure 55 – SLM apparatus: (a) M2 Cusing and (b) SLM 125HL.	96
Figure 56 – XCT & SEM microscopes: (a) ZEISS XRADIA 510 VERSA; (b) HITACHI TM3030; and, (c) JEOL JSM-6701F.	98
Figure 57 – Mechanical characterization and density measurement: (a) EMIC DL 3000 UTM; (b) Split-Hopkinson bar test; (c) Mettler Toledo MS balance.	99
Figure 58 – Cellular structure, geometry A -STR1, 120 mm of height, (a) view of yx plan, (b) view of zy plan, (c) transverse view.	102
Figure 59 – Simplified cube without internal diagonals, geometry B, 120 mm of edge.	102
Figure 60 – Cube with internal diagonals, geometry C, 120 mm of edge.	103
Figure 61 – Poisson’s coefficient in function of compressive deformation in geometry A.	105
Figure 62 – Poisson’s coefficient in function of compressive deformation in geometry B.	105
Figure 63 – Poisson’s coefficient in function of compressive deformation in geometry C.	106
Figure 64 – Stress distribution in geometry A, referring to the first major stress.	107
Figure 65 – Stress distribution in geometry B, referring to the first major stress.	107
Figure 66 – Stress distribution in geometry C, referring to the first major stress.	108
Figure 67 – Compression resistance in function of strut diameter for geometries A, B and C.	109
Figure 68 – Compression test in auxetic structure STR2.	110
Figure 69 – Auxetic structure STR3 and their geometric parameters in a 2D view.	111
Figure 70 – Poisson ratio dependence on angle theta and H/L ratio.	112
Figure 71 – Poisson ratio sensitivity on parameter W for H/L=2.	113

Figure 72 – Poisson ratio analytical and simulation results.	114
Figure 73 – Deformation and stress concentration after compression test in STR3.	114
Figure 74 – Dynamic test on STR3.	115
Figure 75 – Optical microscopy of CL20ES test piece.	117
Figure 76 – CL20ES powder SEM analysis: amplification of 100x (left) and 1000 x (right).	118
Figure 77 – Morphology and size measurements of CL20ES.	119
Figure 78 – CL20ES powder particles on SEM, 1000x magnification.	121
Figure 79 – EDS analysis of CL20ES powder.	123
Figure 80 – SLM machine M2 Cusing (ConceptLaser).	123
Figure 81 – Fabrication area inside M2 Cusing SLM machine (ConceptLaser).	124
Figure 82 – SLM samples before heat treatment - (a) auxetic geometry part; (b) cylindric dense parts.	124
Figure 83 – SLM samples after heat treatment - (a) porous parts (b) cylindric dense parts Mettler-Toledo balance used to measure sample porosity	124
Figure 84 – XCT analysis of SLM P _i samples: (a) P ₀ ; (b) P ₁ ; (c) P ₂ .	128
Figure 85 – Lateral cuts (a and b) of fragment (c) from porous SLM sample.	128
Figure 86 – Mechanical behavior of sample P ₀ under compression – (a) Load – strain curve; (b) elastic portion of compressive test.	129
Figure 87 – Ti-6Al-4V powder particles analyzed by SEM-FEG.	131
Figure 88 – SLM Machine 125HL (SLM Solutions).	131
Figure 89 – Auxetic SLM Ti-6Al-4V samples with support structure on the building plate.	134
Figure 90 – AgieCharmilles CUT 20 P WEDM equipment.	134
Figure 91 – Heat treatment under argon atmosphere for Ti-6Al-4V auxetic samples.	135
Figure 92 – Ti-6Al-4V STR3 auxetic samples: (a) STR3 sample containing support structure before heat treatment; (b) STR3 sample without supports, after heat treatment described in Figure 91.	136
Figure 93 – Distribution of Porosity of Ti-6Al-4V samples measured by Archimedes method	137
Figure 94 – Split-Hopkinson bar test setup of STR3	139
Figure 95 – Split-Hopkinson bar test of STR3	140
Figure 96 – Armor plates from ballistic vests	140
Figure 97 – Armor models using ceramic plates and polymer auxetic structures (a) composite auxetic structures (b), (c), and (d)	141
Figure 98 – Composite armor model containing an auxetic metallic component with graded porosity	143
Figure 99 – Auxetic multilayer design	144
Figure 100 – Composite armor including hard ceramic plate, auxetic metallic interlayer and a thin kevlar layer	145

TABLE INDEX

Table 1 – Properties of Titanium and Ti-6Al-4V.	30
Table 2 – Stainless steel types and main grades.	36
Table 3 – Properties of selected stainless steels and other alloys.	37
Table 4 – ν values for different materials.	38
Table 5 – Auxetic materials examples.	41
Table 6 – Geometric parameters of Ti-6Al-4V auxetic structures.	47
Table 7 – Mechanical properties for Ti-6Al-4V D1 and D2 structures.	49
Table 8 – Mechanical properties of different auxetic designs.	50
Table 9 – Laser and scanning parameters in SLM method.	53
Table 10 – Powder material properties in SLM process.	54
Table 11 – Environmental parameters in SLM process.	54
Table 12 – Laser types and intrinsic characteristics.	58
Table 13 – Sources of error in measurement of RS.	69
Table 14 – Methods for relieving of Residual stresses.	70
Table 15 – Field of application for NDT in materials characterization	72
Table 16 – Strategies of in situ RS reduction.	76
Table 17 – Properties of Ti-13Zr-13Nb and Ti-6Al-4V.	91
Table 18 – CL20ES SS powder features.	95
Table 19 – Ti-6Al-4V powder datasheet (Ti64).	95
Table 20 – Deformation of geometry A in Z & Y axis.	103
Table 21 – Deformation of geometry B in X & Y axis	104
Table 22 – Deformation of geometry C in X & Y axis.	104
Table 23 – Height/diameter ratio for structures and struts diameter.	109
Table 24 – Absorbed energy on STR3 after ballistic impact.	115
Table 25 – Histogram related to circular diameter and grain volume.	120
Table 26 – Histogram related to roundness (aspect ratio).	120
Table 27 – Histogram related to suavity.	121
Table 28 – Results from EDS analysis of CL20ES chemical composition.	122
Table 29 – Features from M2 Cusing SLM machine.	124
Table 30 – SLM processing parameters employed in CL20ES sample fabrication.	125
Table 31 – Heat treatment of SLM made samples.	126
Table 32 – Parameters of acquisition for ZEISS XRADIA VERSA XCT equipment.	127
Table 33 – Analysis of pores and porosity of P ₀ , P ₁ , P ₂ samples.	128
Table 34 – Setup of compression tests for P _i samples.	130
Table 35 – Main features of SLM Solutions 125HL.	133
Table 36 – Fabrication parameters for Ti-6Al-4V samples by SLM.	133
Table 37 – Porosity of auxetic Ti-6Al-4V samples measured by Archimedes method.	148

ABBREVIATION INDEX

AM – Additive Manufacturing
CAD/CAM – Computer Aided Design/ Computer Aided Manufacturing.
DMLS - Direct Metal Laser Sintering.
EBM – Electron Beam Melting.
FDM – Fused Deposition Modelling.
FEM – Finite Element Method.
NPR – Negative Poisson Ratio.
PROMETHEE – Preference Ranking Organization Method for Enrichment Evaluations
PVB – Polyvinyl Butyral.
RP – Rapid Prototyping.
RS – Residual Stress.
SEM – Scanning Electron Microscope.
SLM – Selective Laser Melting.
SLS – Selective Laser Sintering.
SS – Stainless Steel.
SS-316L – Stainless Steel 316L alloy.
TEM – Transmission Electron Microscope.
Ti-6Al-4V – Titanium alloyed with 6% of Aluminum and 4% of Vanadium.
Ti-13-13 – Titanium alloyed with 13% of Zirconium and 13% of Niobium.
V – Scanning Speed (mm/s).
XCT – X-Ray Computed Microtomography.
 ν – Poisson coefficient [no dimension].

SUMMARY

1.	INTRODUCTION	22
2.	RESEARCH OBJECTIVES	28
3.	STATE OF THE ART	29
3.1	MATERIALS OF INTEREST IN SLM	29
3.1.1	Ti-6Al-4V	29
3.1.2	Processing Ti-6Al-4V via SLM	32
3.1.3	Stainless steel	35
3.2	AUXETIC MATERIALS/STRUCTURES: CONCEPT AND INTEREST	37
3.2.1	Behavior of auxetic structures	39
3.2.1.1	<i>Auxetic structures applications</i>	42
3.2.1.2	<i>Auxetic structures in tissue engineering</i>	44
3.2.2	Present research in auxetic structures	46
3.2.3	Auxetic High Energy absorption impact applications	51
3.3	PARAMETER INFLUENCE IN SLM PROCESS	52
3.3.1	Laser power	55
3.3.2	Scan speed and scan strategies	59
3.3.3	Metal powder specifications	60
3.3.4	Support structures.....	61
3.4	PHENOMENA IN SLM PROCESSING	63
3.4.1	Oxidation	63
3.4.2	Absorption and reflection	63
3.4.3	Heat transfer	64
3.4.4	Phase transition	66
3.4.5	Residual Stresses	66
3.4.5.1	<i>RS measurement methods</i>	70
3.4.5.2	<i>RS measurement cases</i>	72
3.4.5.3	<i>RS in-situ measurement/monitoring</i>	73
3.4.5.4	<i>RS in-process control</i>	75
3.4.5.5	<i>RS post-process control</i>	78
3.5	PARAMETER INFLUENCE ON PART PROPERTIES	79
3.5.1	Scanning rate and scanning strategies	79
3.5.2	Microstructure	84
3.5.3	Scanning speed and laser power	85
3.6	SLM PERSPECTIVES AND ENHANCEMENTS	88
3.7	SIMULATION USING FEM	91
4.	MATERIALS AND METHODS	94
5.	RESULTS AND DISCUSSION	101
5.1	SIMULATION OF AUXETIC STRUCTURES	101
5.2	FABRICATION OF AUXETIC METALLIC SAMPLES	116
5.2.1	Characterization of stainless steel powder	116
5.2.1.1	<i>Chemical composition analysis of stainless steel powder</i>	122

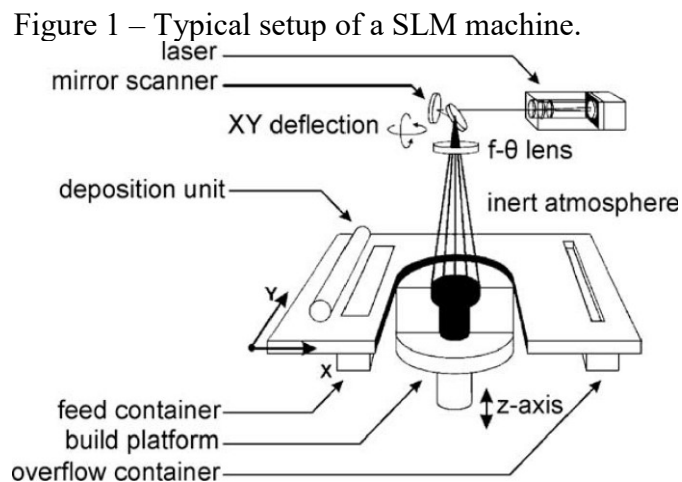
5.2.2	Fabrication of SS samples.....	122
5.2.2.1	<i>XCT characterization of SS-316L samples.....</i>	126
5.2.2.2	<i>Compression tests of SS-316L samples.....</i>	129
5.2.3	Characterization of Ti-6Al-4V powder.....	130
5.2.4	Fabrication of Ti-6Al-4V samples.....	131
5.2.4.1	<i>Porosity of Ti-6Al-4V samples.....</i>	135
5.2.4.2	<i>Mechanical tests of Ti-6Al-4V samples.....</i>	138
	<i>Static tests.....</i>	138
	<i>Split-Hopkinson bar test: dynamic behavior of auxetic samples.....</i>	138
5.3	BUILDING HIGH ENERGY IMPACT RESISTANT ARMOR MODELS.....	139
6.	CONCLUSIONS.....	146
7.	FUTURE WORK.....	147
8.	ANNEX.....	148
9.	REFERENCES.....	149
10.	APPENDIX – SCIENTIFIC PRODUCTION IN PhD PERIOD (2015 - 2020).....	164

1 INTRODUCTION

Additive Manufacturing (AM) is a high edge research subject, with special emphasis to techniques which allow the production of parts starting from different types of materials (ceramics, metals, polymers). These processes bring the flexibility of creating complex structures with mechanical properties very similar to parts obtained by conventional fabrication methods. Among these techniques of AM, which can fabricate prototypes and mechanical components, a few can be cited (YADROITSEV, 2007):

- Selective Laser Sintering (SLS).
- Selective Laser Melting (SLM).
- Electron Beam Melting (EBM).
- Laser Metal Deposition (LMD).
- Electron Beam Direct Manufacturing.
- Wire Arc Additive Manufacturing.
- Direct Metal Laser Sintering (DMLS).

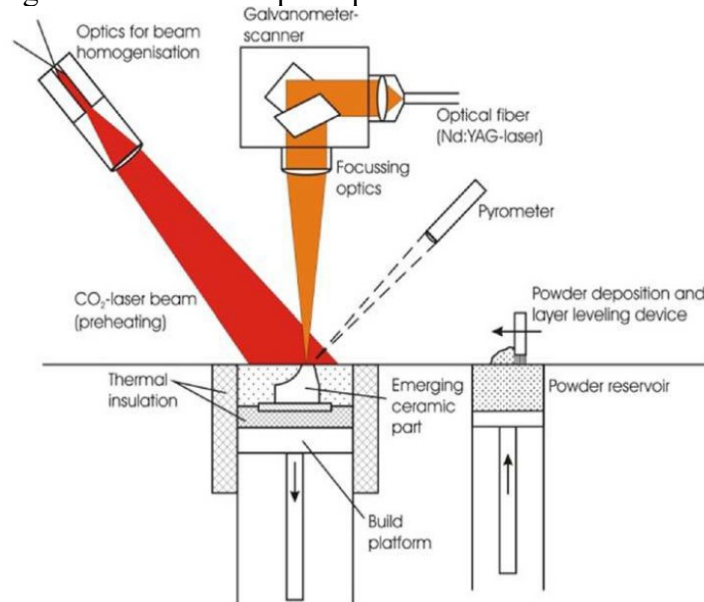
Selective Laser Melting (SLM) is one of the techniques included in former known as Rapid Prototyping (RP) processes. This technique was developed in 90's at Fraunhofer ILT, one decade after the invention of Selective Laser Sintering (SLS). Conventional SLM apparatus is displayed in Figure 1 (TUCK, 2015): this basic setup is observed in first generation machines and experimental prototypes.



Reference: (TUCK, 2015).

The principle of SLM is to sinter and melt powder particles using a laser (typically fiber, Nd-YAG or CO₂ laser). Figure 2 shows the construction of a metallic part using SLM. A typical SLM machine setup includes a moving build platform; a build chamber under vacuum (Argon, Helium or Nitrogen are the most used); optics to focus the laser beam and change laser scan trajectories; a ruler to homogenize powder layers; and, in more modern apparatus, a secondary laser to preheat powder (typically CO₂, as they present lower power output – under 50 W). This additional laser beam performs preheating of the powder and softens thermal gradients created during SLM process.

Figure 2 – Schematic principle of SLM machine.

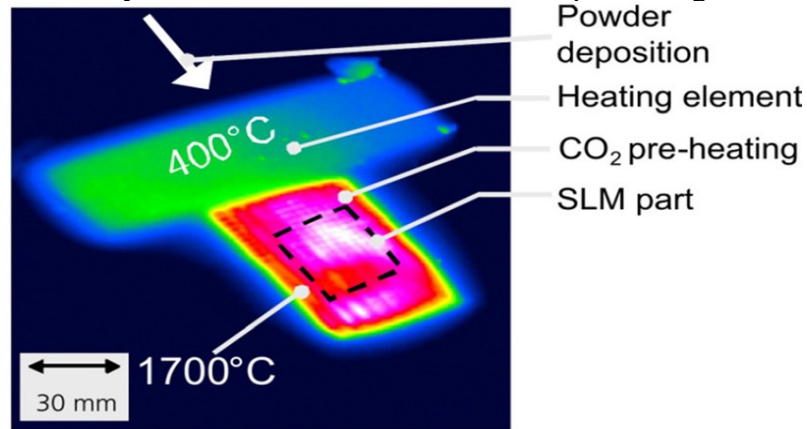


Reference: (HAGEDORN, 2011).

An alternative to preheat the powder is to introduce a heating coil in the powder feed chamber. This heating strategy produces a more homogeneous thermal gradient: compared to the CO₂ laser beam, a heating coil could heat a greater amount of powder, since the laser beam has limited penetration in the powder layer, typically up to 10 μm .

Yap et al (YAP, 2015) proposed a hybrid preheating mechanism in which CO₂ laser is combined to a resistive element to reduce thermal gradients during SLM process. At first, recently deposited powder is preheated at 400 $^{\circ}\text{C}$ using a resistive element, then, powder in the immediate surroundings of fabrication zones are preheated at higher temperatures – around 1700 $^{\circ}\text{C}$ - by CO₂ laser (Figure 3).

Figure 3 – Detail of hybrid CO₂ laser - resistive element preheating mechanism.

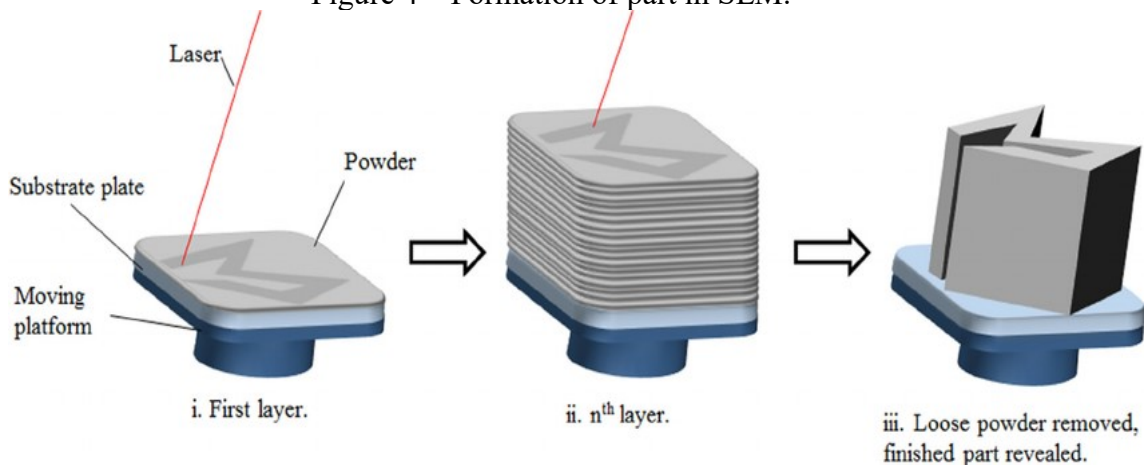


Reference: (YAP, 2015).

There are a few steps to be followed to create parts using SLM method:

- At first, a 3D CAD model is built and then a Standard Triangle Language (STL) file is obtained.
- After selecting part geometry and support structures, composition must be defined. Then, powder material is fed at the building chamber.
- After setting laser parameters (power, scanning strategies, hatch distance and mean time to build one layer) and the powder layer thickness, building begins.
- Following STL model, the part will be built layer by layer. After each layer is completed, building platform lows down and a new layer is added and linked to the previous one by sintering and melting until the part is complete (Figure 4).

Figure 4 – Formation of part in SLM.



Reference: (YAP, 2015).

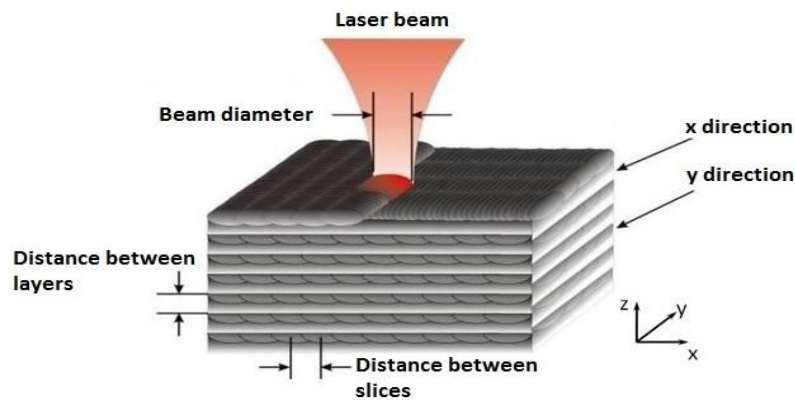
- After complete cooling of the part, loose powder is removed, revealing the finished part. As a final step, the part fabricated by SLM has to be separated from the build platform and this is performed by Wire Electrical Discharge Machining (WEDM or wire-cut EDM) This technique provides a good precision cut but suffers from limited productivity and it is restricted to conductive materials (GRIGORIEV, 2019).

- Furthermore, it is possible to perform an optimization of fabrication parameters, following specifications (geometry and composition), as well as preliminary simulation results of the object under construction.

In SLM process, powder particles are selectively molten to form a solid object. In this sense, as high-density parts are created, there is no requirement for further fabrication steps (THIJS, 2010).

Figure 5 details melting of the powder by the laser beam. As the laser advances, more particles are molten and sintered, forming a layer of SLM object (SONG, 2012). This pattern is repeated until the last layer is formed and the part is ready for WEDM.

Figure 5 – powder fusion process by a laser source.



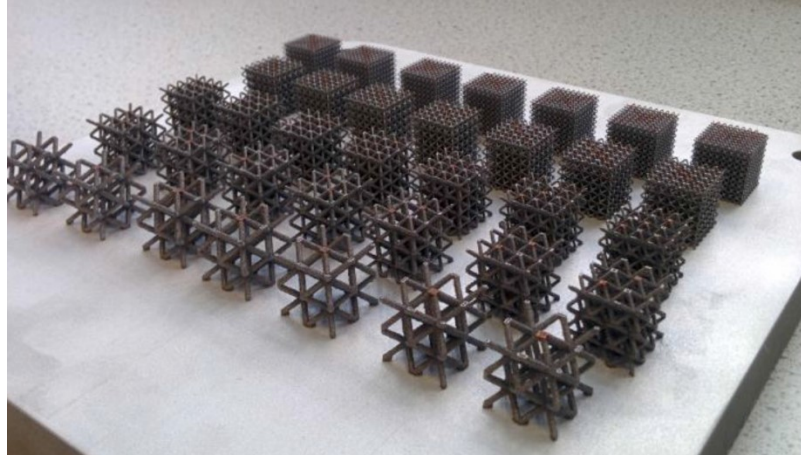
Reference: Adapted from (THIJS, 2010).

In the present research development of Additive Manufacturing, SLM has found greater use in metals such as aluminum alloys, titanium (pure and alloys), stainless steel, cobalt-chrome alloys and also nickel alloys (Inconel, Nitinol, Hastelloy X). All these materials must be in powder with spherical form exhibiting specific flow characteristics (BREMEN, 2012).

Regarding geometry, SLM can produce many complex parts with high accuracy. Complex objects made using SLM are shown in Figure 6 (TUCK, 2015): each part has a

different lattice type and controlled porosity. Furthermore, due to the high dimensional precision and microstructural control, there is a strong potential to create parts with gradient of properties and composition, in parallel with Functionally Graded Materials (FGM).

Figure 6 – SLM-made structures, showing different lattice types.



Reference: Adapted from (TUCK, 2015).

Frequently, the choice to create free form models helps directly the aeronautic, aerospace and nuclear industries, for example, in the creation of ribs with huge gaps for mass relieving, created through Topological Optimization Method (TOM), without any loss to the mechanical resistance of parts. In a study developed by Airbus in the A380 model, using TOM and Finite Element Method (FEM) simulations, it was possible to reduce the plane mass around 10 kg, only considering brackets (FISCHER, 2003).

AM processes allow the development of parts with fewer assemblies (monolithic parts) and a more sustainable fabrication, with the reduction of material wasting. Figure 7 shows a titanium bracket made by Direct Metal Laser Sintering (DMLS) process. In this case, a plane bracket geometry was modified by TOM, which provided a new part with increased mechanical resistance in combination with lower mass, an absolute demand in the aeronautic industry.

Figure 7: Airbus A320 Bracket fabricated with DMLS.



Reference: Adapted from (FISCHER, 2003).

Also, in order to provide a broad understanding of different techniques in Additive Manufacturing, it is worth to compare SLM and Electron Beam Melting (EBM). SLM presents a higher solidification rate than EBM, since no pre-heating is applied to the growing part and the working zone. As a result, the microstructure of SLM parts are finer in detriment of larger residual stresses. Pre-heating allows the remelting of just-consolidated substrate, avoiding wetting due to oxide films. Regarding EBM, this process uses pre-heating, at about 600 °C to reduce thermal gradients and residual stresses (LIMITED, 2015). Due to its high affinity on oxygen nitrogen and hydrogen, Ti and its alloys have to be processed under inert gases such as Argon and Helium, to avoid oxidation and other undesired reactions.

The flexibility of SLM allows the fabrication of complex structures based on Ti-6Al-4V, which would be difficult to obtain using conventional fabrication techniques such as powder metallurgy and self-propagating high temperature sintering - SHS (AGRIPA, 2019). By changing structure geometry, several properties can be changed, including strength resistance, yield stress and Poisson's ratio. When this last parameter becomes negative (Negative Poisson Ratio), several characteristics and features appear: greater resistance to compression; expansion in all dimensions under traction.

Parts and materials that contain this property – Negative Poisson Ratio (NPR) – are called auxetic. Up to date, auxetic structures and materials are acquiring great interest in several fields of research: biomaterials; noise absorption; sports; armor; aeronautic and spatial; sensors (MEENA, 2019; YANG, 2017). This new research era for auxetic structures is strongly pushed by the growth and availability of AM techniques (MEENA, 2019)

In the scope of this research work, a protective auxetic armor is proposed. This armor has a sandwich design composed of three layers (hard ceramic/auxetic structure/Kevlar). As an important alternative to conventional passive ballistic defense

components, this system has to endure the impact of several projectiles. In this sense, two research questions were elaborated to understand the performance of auxetic structures: how these auxetic structures can be optimized? And, how geometric parameters can be explored to increase NPR?

To fulfill this research question and test this hypothesis, general and specific objectives were established to achieve these particular targets.

2 RESEARCH OBJECTIVES

The general objective of this research is the following:

- Creation, simulation and optimization of auxetic structures using 3D design and mechanical simulation software COMSOL and ANSYS 19.

Moreover, several specific objectives are set to accomplish research hypothesis:

- Fabrication of auxetic structures by SLM from Ti-6Al-4V and 316L stainless steel powder.
- Characterization of auxetic samples: microstructure analysis, mechanical tests and XCT.
- Optimization of structure parameters to increase performance in mechanical tests, especially in compression.
- Development of new auxetic structures aiming high compressive resistance.
- Creation, simulation and optimization of ballistic composite armor models.
- Characterization of composite armor samples: mechanical tests; ballistic tests.

3 STATE OF THE ART IN SLM

3.1 MATERIALS OF INTEREST IN SLM

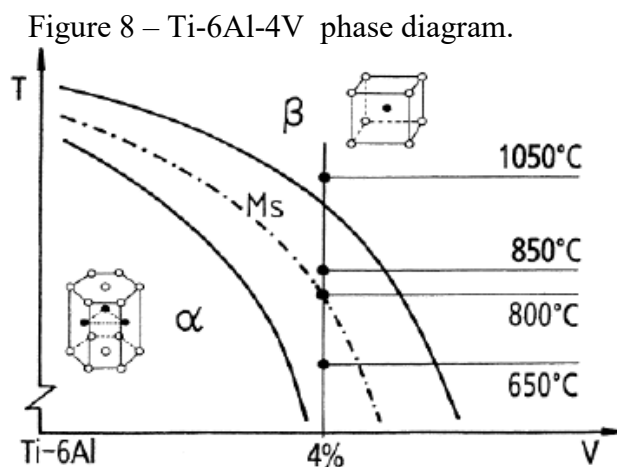
Up to date, only a few materials are available to use in SLM, among them the following can be cited: Ti-6Al-4V, Stainless steel (hot-work steel, stainless hot-work steel, precipitation hardening steel, 316L, 300), AlSi₁₀Mg, pure titanium, Nickel alloys (718 and 625), Cobalt-chromium alloys, Gold, Platinum, Silver alloys, bronze.

In the scope of this study, special emphasis will be given to Ti-6Al-4V, since it has remarkable mechanical properties. Complementarily, ordinary stainless steel (1.4404) is also studied as an alternative to titanium alloys.

3.1.1 Ti-6Al-4V

Titanium is an element of choice for most of aeronautical and biomedical applications. This element has a very high resistance to corrosion associated with a high strength to density ratio, the highest among all metals. In its unalloyed condition, titanium is as strong as steel but is 45% lighter (WWW.3DERS.ORG, 2014).

Pure Titanium crystallizes at low temperatures in hexagonal close-packed structure (hcp) and stays stable until 882 °C - it is referred as α -titanium. Above 882 °C, hexagonal close-packed structure transforms into body-centered cubic (bcc) structure that is stable until 1668 °C and it is referred as β titanium (Figure 8) (HAMPEL, 1968), (BANERJEE, 2007).



Reference: (DUCATO et al., 2013).

Ti-6Al-4V – titanium alloyed with 6% of aluminum and 4% of vanadium - is a well-known α - β titanium alloy: it was developed in the 1950 decade for aeronautical purposes. This alloy has a lower density compared to steel (50% less). Ti-6Al-4V offers a combination of high strength, light weight, high formability and corrosion resistance, which have made it a world standard in aerospace applications. Also, this alloy represents the highest titanium usage, accounting for 50% in titanium production industry (3DERS, 2014). Table 1 presents the main physical properties of pure Ti (grade 2) and Ti-6Al-4V (Extra Low Interstitial – ELI – high purity and suitable for biomedical applications) (SYSTEM).

Some of the many applications where this alloy has been used include aircraft turbine engine components, aircraft structural components, aerospace fasteners, high-performance automotive parts, marine applications, medical devices, and, sports equipment. Typically, it is mainly processed by hot working, nevertheless, in the past years there has been a growing use of Additive Manufacturing (AM) techniques such as SLM and Electron Beam Melting (EBM).

Table 1 – Properties of Titanium and Ti-6Al-4V.

Properties	Ti grade 2	Ti-6Al-4V ELI
Density (g/cm ³)	4.51	4.43
Poisson ratio	0.33	0.34
Tensile ultimate strength (MPa)	570	1020
Tensile yield strength (MPa)	540	950
Modulus of elasticity (GPa)	103	120
Elongation at break (%)	21	14
Reduction of area (%)	55	40
Fatigue strength @ 600 MPa (cycles)	-	>10E ⁶

Reference: (SYSTEM Ti grade 2, 2018; SYSTEM Ti-6Al-4V, 2018).

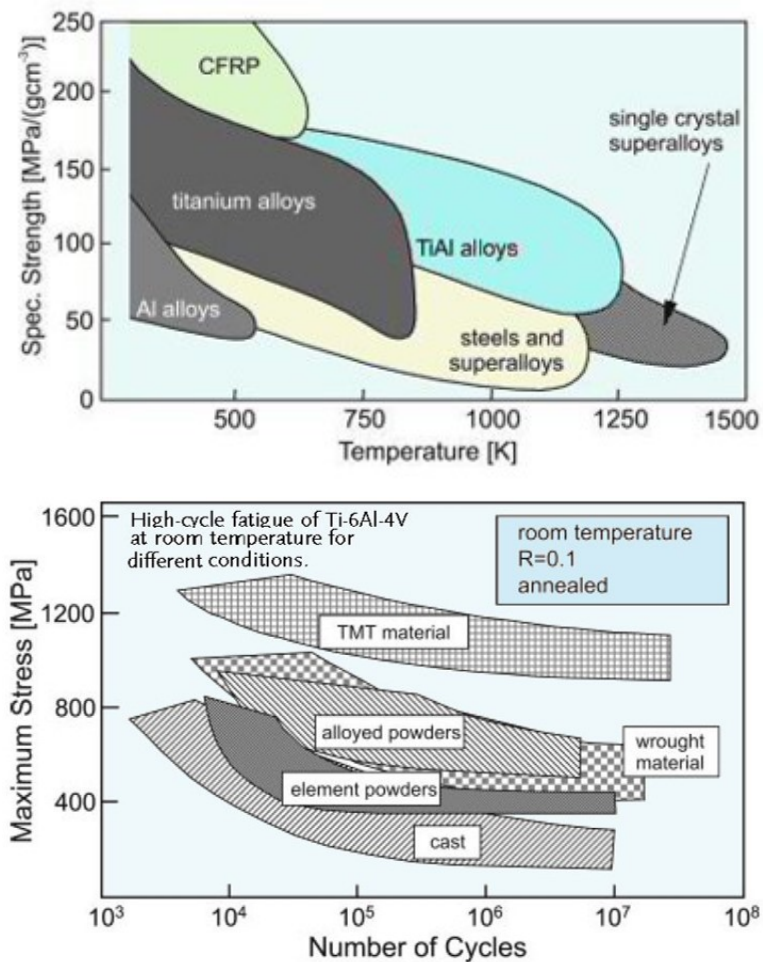
Ti and its alloys can be grouped into three categories according to the predominant phase in their microstructures: α , α - β or β . There are a lot of alloying elements that added to titanium tend to stabilize either α or β beta phase (BANERJEE, 2007).

Compared to other alloys, especially steels and Aluminum, Titanium alloys have higher specific mechanical strength in a temperature range between 625 K and 1200 K (Figure 9 a). Below 625 K, only Carbon Fiber Reinforced Plastic (CFRP) overcomes titanium alloys in specific mechanical strength (LEYENS, 2003).

Regarding high-cycle fatigue (Figure 9 b), Ti-6Al-4V properties are strongly influenced by fabrication condition (cast or wrought) and powder type (alloyed or element).

In each case, mechanical surfaces have significant differences, which is reflected in contrasting fatigue behavior (LEYENS, 2003). To counter low fatigue resistance, mechanical surface treatments can be employed such as Laser Shock Peening (LSP), which introduces an important amount of compressive stresses (SONNTAG, 2015).

Figure 9 – a) Specific mechanical strength of Ti alloys compared to other metals and CFRP. b) High-cycle fatigue of Ti-6Al-4V for different settings.



Reference: (LEYENS, 2003).

3.1.2 Processing Ti-6Al-4V via SLM

SLM presents many advantages regarding conventional methods. As a first remark, the use of a Computer Aided Design (CAD) brings flexibility to produce complex geometries associated with high accuracy.

Advantages of SLM regarding conventional methods (GOKULDOSS, 2017):

- Almost no limitation on geometry types.
- Several materials, especially Ti-6Al-4V, are easier to fabricate via SLM.
- Materials availability in SLM is actively growing: titanium (pure, Ti-6Al-4V, and TiNi); stainless steels (316L, 304, 18Ni-300, 17-4PH); cobalt-chrome alloys (Co-Cr-W, Co-Cr-Mo); nickel alloys (Inconel 718, 939, 625); aluminum alloys (Al-xSi, Al-Si-10Mg); copper (Cu-10Sn); and, composites (Ti-TiB, Al-12Si-TMN, TiC/Inconel 718, Inconel 625/TiB₂).

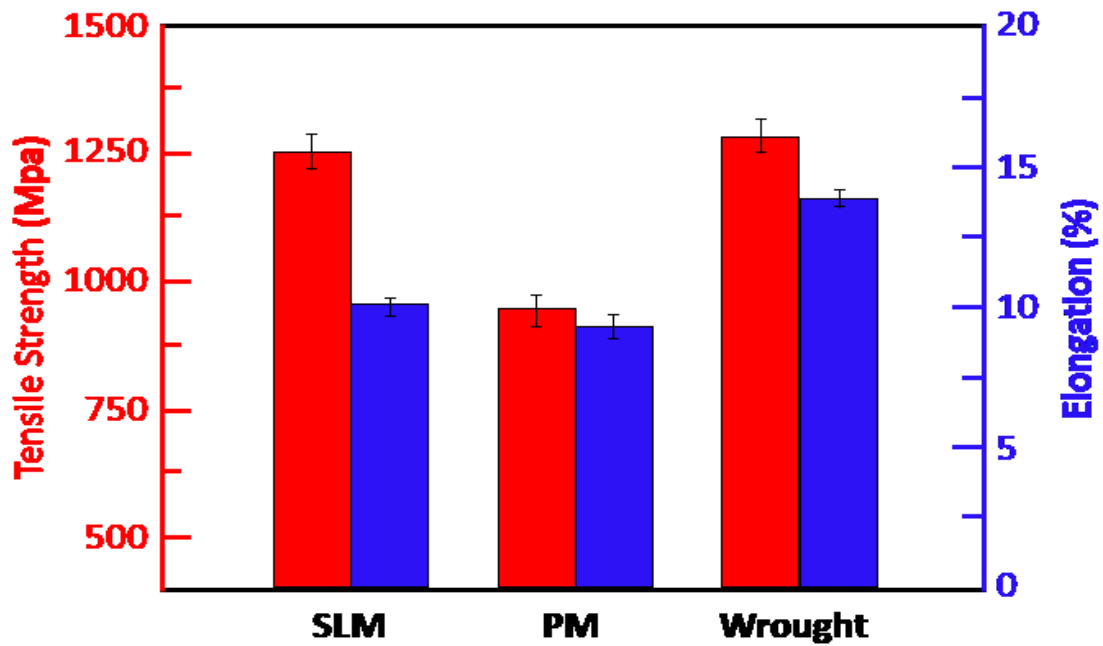
- High densification of parts.
- High dimensional precision.
- Controlled atmosphere with N₂, He or Ar, which avoids oxidation while melting.

Despite all these advantages, there are still some challenges to be considered (GOKULDOSS, 2017):

- High rate of shrinkage of parts, due to important thermal gradients.
- Fabrication time is typically high and parts are limited in size.
- A big amount of powder is required to fabricate parts. Still, some of this powder can be recovered and reused in the process. Nevertheless, this can bring contamination and properties changes to the initial powder and powder reuse is not well defined.

Figure 10 shows tensile strength of Ti-6Al-4V SLM-produced parts (HE, 2018). This value is compared to samples obtained by wrought technique (around 1250 MPa), and, are greater than specimens fabricated by Powder Metallurgy (around 950 MPa). In the other hand, regarding elongation SLM and PM have equivalent values – around 10 %; whilst wrought samples have significantly higher Elongation values of approximately 14%.

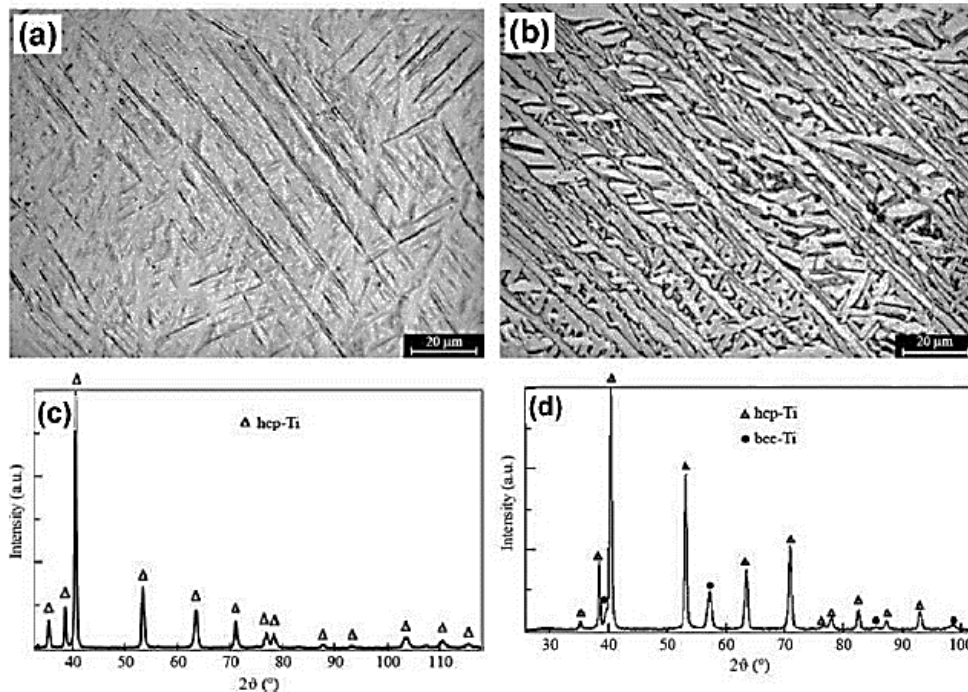
Figure 10 – Mechanical properties of Ti-6Al-4V samples produced by SLM, Powder Metallurgy and Wrought.



Reference: (HE., 2018).

As Ti-6Al-4V is processed by SLM, it acquires a martensitic structure (Figure 8). The matrix is composed of acicular hcp- α -phase, without presence of bcc- β -phase (Figures 11a and 11c). Still, as a specific heat treatment is applied, microstructure is refined, β -phase returns and Ti-6Al-4V becomes $\alpha+\beta$ again (Figures 11b and 11d). Moreover, due to RS and incomplete homologous wetting, microcracks are formed in the final part (HAMPEL, 1968).

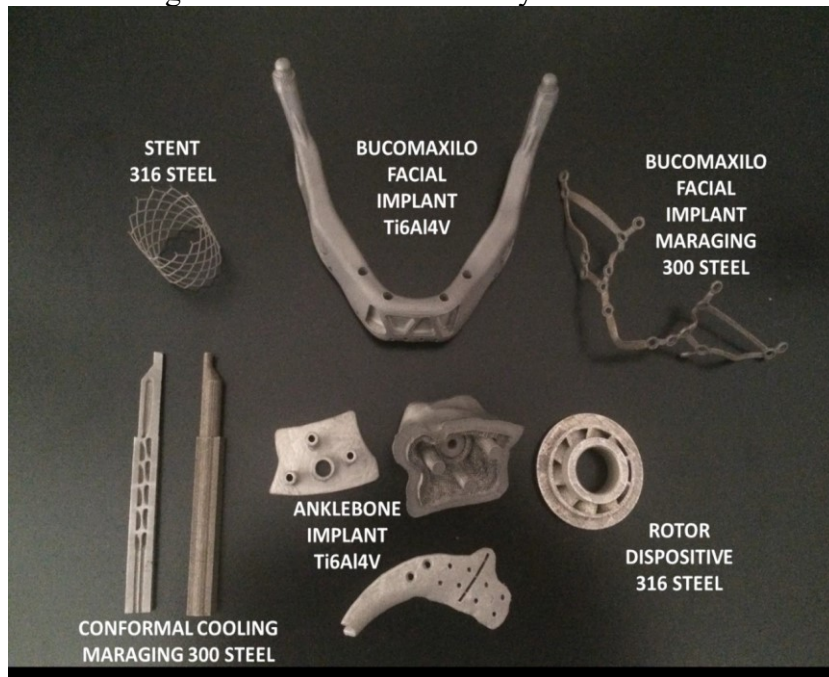
Figure 11 - oriented martensite plates containing acicular hcp phase in SLM processed Ti-6Al-4V; (b) and (d) biphasic α - β microstructure in heat treated material.



Reference: adapted from (GU, 2012).

Figure 12 show parts fabricated by SLM. Such specimens have complex geometries, which reveals the astonishing potential of AM: a Ti-6Al-4V buccomaxillary facial implant custom made following specifications from Computer Tomography (CT), created to substitute maxilla loss after accidents or disease (cancer, acute osteoporosis); a 316L steel stent for optimized bloodflow, typically used in arteries close to the heart (NHS, 2018); a Maraging 300 Steel buccomaxillary facial implant aimed to provide support for the region around the nose; a Ti-6Al-4V ankle bone implant used to recover regions affected by calcaneus (heel) cancer (CSIRO, 2014). Finally, steel parts (300 Maraging and 316L), composed of regular cavities to optimize cooling and fluid flux. As such, these complex features cannot be obtained by conventional methods, especially Computer Numerical Control Machining (CNC) (THOMAS, 2020).

Figure 12 – Parts fabricated by SLM.



Reference: Own authorship, 2018.

3.1.3 Stainless Steel (SS)

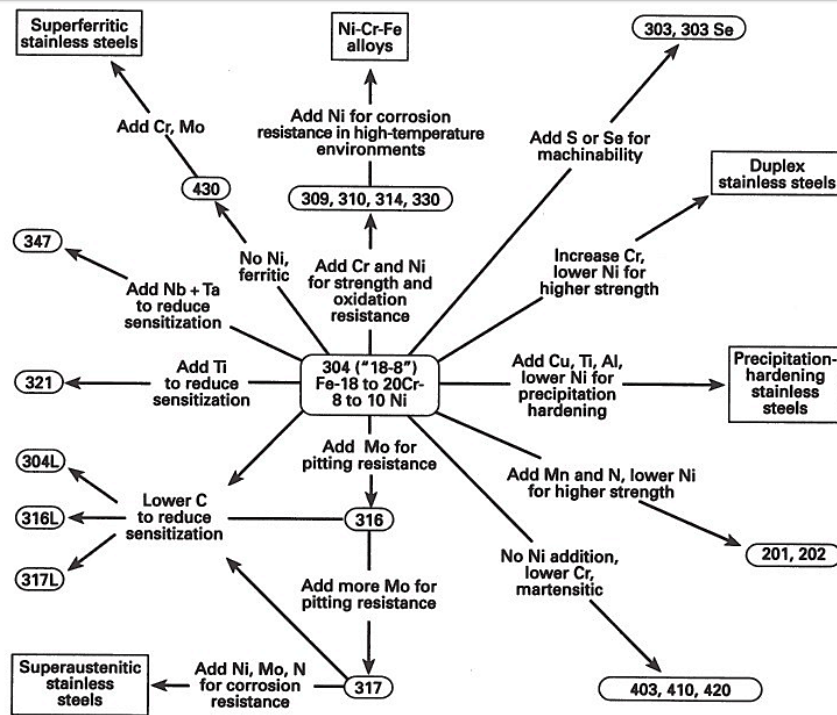
As a first approach to our study, SS was chosen for its properties and high cost effectiveness. Since the auxetic property is verified when a proper geometry is implemented, the choice of the material is not the first criterion of choice.

Steel has become a material of choice for several applications since it presents interesting properties such as: cost effectiveness; ease of fabrication and processing; easily recyclable.

By adding a specific percentage of chromium - at least 12% - according to American Society of Metals (ASM) - steel acquires a higher resistance to corrosion and it becomes stainless steel. This property is achieved by the formation of an invisible thin film of chromium oxide in the surface of the steel. Besides, stainless steel can be alloyed with several other elements: molybdenum, nickel, manganese, copper, titanium, silicon, niobium, selenium, aluminum, among others (DAVIS, 2001).

There is a great variety of stainless steels. Figure 13 shows numerous possibilities of alloying and the corresponding properties for each case (DAVIS, 2001)

Figure 13 – Stainless steel alloys and related properties.



Reference: Adapted from (DAVIS, 2001).

Stainless steels are divided into five categories: austenitic, ferritic, martensitic, duplex and precipitation hardenable (PH). Table 2 shows the main grades of each stainless-steel category (DAVIS, 2001).

Table 2 – Stainless steel types and main grades.		
SS type	Grade	Composition / Characteristics
Austenitic	Fe-Cr-Ni (AISI 300 series and alloys)	16 – 22% Cr; 10 – 22% Ni; low quantities of Mo, Ti, N
	Fe-Cr-Mn-Ni (AISI 200 series and alloys)	5 – 18% Mn;
Ferritic	Standard 400 series alloys	11 – 27% Cr; 0,08 – 20% C; low quantities of Al, Nb, Ti
	Superferritics (low C and N)	Up to 30% Cr; up to 4% Mo; up to 2%
Martensitic	Standard 400 series	11 – 18% Cr; up to 1,2% C; low quantities of Mn and Ni
	Non - standard	Free machining grades; heat resistant grades; gear and bearing grades
Duplex	2205 alloys	22 – 25% Cr; 5 – 7% Ni; up to 4% Mo
Precipitation Hardenable	Cr – Ni alloys with low quantities of Al, Cu and Ti	Can be divided into martensitic, semi-austenitic and austenitic

Reference: (DAVIS, 2001).

Comparing to ordinary steel and other steel alloys, stainless steel presents some similarities, which are summarized in Table 3.

Table 3 – Properties of selected stainless steels and other alloys.

Steel type	E (GPa)	Yield strength 0,2 % offset (MPa)	Ultimate tensile strength (MPa)	Density (g/cm ³)
Type 304 (austenitic SS)	193	241	586	8.00
Type 316L	193	205	515	8.03
S32950 (Duplex SS)	192 - 200	570	760	7.80
S45500 (PH SS)	200	793	1000	7.80
AISI 1080 (Carbon steel)	200	455	821	7.87
Type 6061 (Al alloy)	69	55	124	2.70

Reference: (DAVIS, 2001).

Therefore, SS presents similar properties to common/alloyed steel. Its main advantage is the higher resistance to corrosion. Also, SS can be formed in similar modes as standard steel (carbon/alloyed steel). Moreover, steels such as Maraging MS1, SS Types 300, 15-5 and 17-4 PH1 are widely used in AM processes, especially Direct Metal Laser Sintering (MET, 2017).

Compared to Titanium and its alloys, SS has as main advantage an ease in fabrication and a minor price per kilogram.

3.2 AUXETIC MATERIALS/STRUCTURES: CONCEPT AND INTEREST

An auxetic material has as its main characteristic a negative Poisson ratio (represented by acronym NPR - Negative Poisson Ratio) (BAKER, 2011).

Typically, most of the materials have a Poisson coefficient between 0.2 and 0.4. Table 4 shows several values of Poisson coefficient for different materials (MOTT, 2009).

More recently, authors reported the existence of auxetic nanomaterials: black phosphorus (JIANG, 2014); orthorhombic arsenic (HAN, 2015); borophane (KOU, 2016); GeSe and SnS (HANAKATA, 2016); narrow graphene ribbons (JIANG, 2016) and semifluorinated graphene (QIN, 2017); MoSe₂, MoTe₂, WSe₂, WTe₂, TcTe₂, ReSe₂, ReTe₂ (YU, 2017).

Still, more analytical and mechanical developments are required to understand how auxeticity affects nanomaterials properties (ZHANG, 2020), and, how to effectively control NPR in these structures (PARK, 2017).

Table 4 – ν values for different materials.

Material	Poisson's coefficient (ν)
Titanium (dentistry use alloy)	0.30 – 0.31
Gold	0.45
Stainless Steel 18 – 8	0.30
Glasses	0.18 – 0.30
Natural rubber	0.499
Cork	0.0

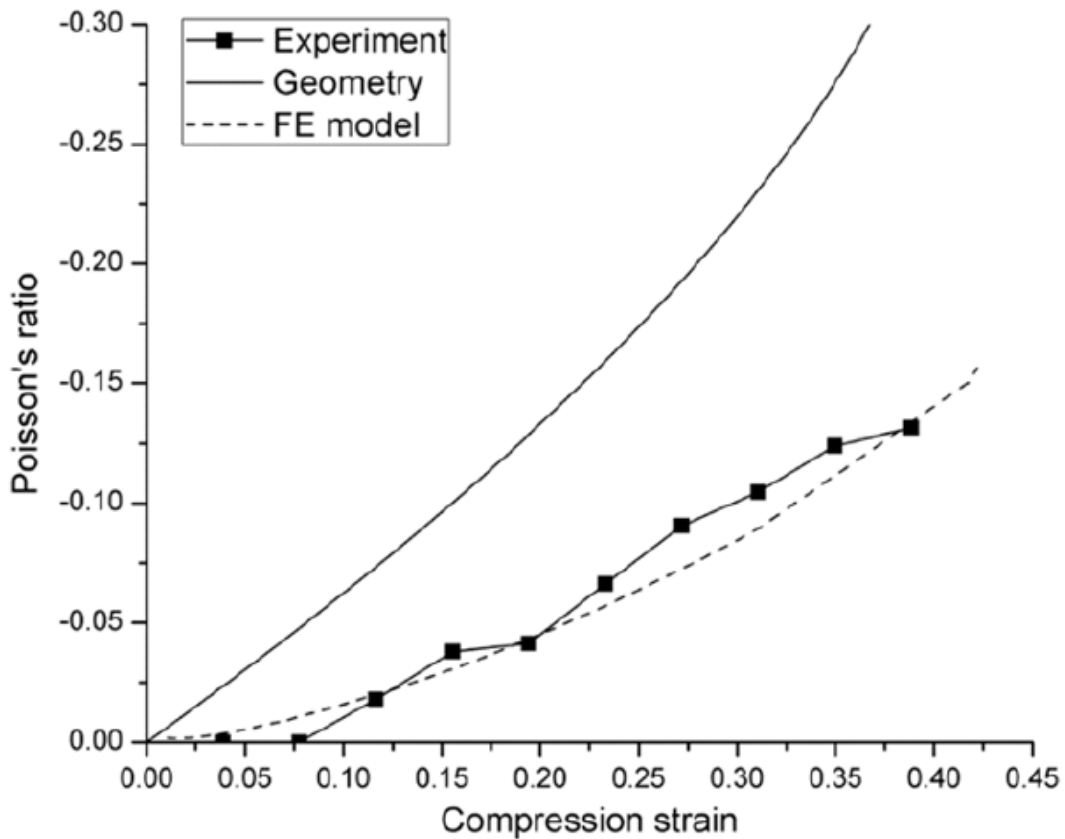
Reference: Adapted from (MOTT, 2009; HIBBELER, 2011).

Poisson's coefficient is a non-dimensional ratio defined as the fraction between longitudinal elongation and lateral compression after a uniaxial traction effort. This coefficient allows the characterization of matter contraction perpendicular to the applied effort direction (MOTT, 2009). Considering isotropic materials, the values for this elastic constant are comprised in the $[-1, 0.5]$ interval. The maximum value of ν is 0.5 and it corresponds to the case of an incompressible material (natural rubber), whilst the $\nu = 0$ case is correlate to a very little or zero lateral expansion after a compression effort, as it is observed for cork. For anisotropic materials, Poisson's coefficient can be under/over its isotropic limits: auxetic PTFE can have a Poisson ratio of -12.00 (1200% of expansion/shrinkage in a specified direction).

- $$\nu = - \frac{\varepsilon_{axial}}{\varepsilon_{extension}}$$
 where ε_{axial} is the axial deformation (<0 for traction; >0 for compression). $\varepsilon_{extension}$ is the transverse deformation (>0 for traction, <0 for compression);
- $\frac{1}{2} > \nu > -1$ (isotropic case);
- Auxetic Materials present $\nu < 0$

Moreover, Poisson's coefficient is defined for a given range of deformation (under the elastic regime), there is to say, it is not constant under any stress value. This parameter has a dependence on the applied strain, which is represented in Figure 14 for a textile material under compression (GE, 2013).

Figure 14 – Typical ν – compression strain curve for a textile material (Simulation, Experiment and geometrical analysis).



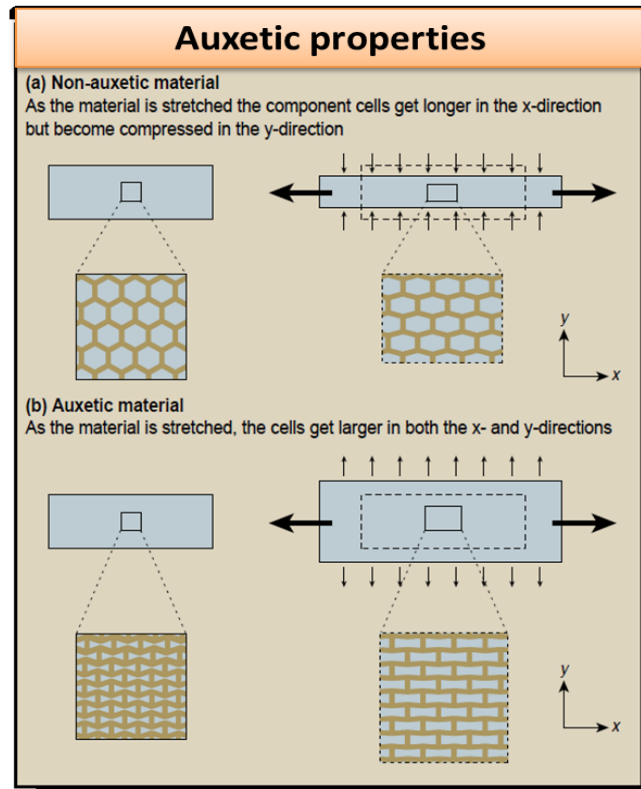
Reference: (GE; HU; LIU, 2013).

Finally, Poisson's ratio is also dependent on time and temperature, which causes expansion or shrinkage according to the variability of material properties (MAY, 1988; CARNEIRO, 2016).

3.2.1 Behavior of auxetic structures

Figure 15 presents the behavior of two distinct structures: in (a) a conventional material is uniaxially pulled, its internal structure is elongated in x direction while in y direction a compression is observed; in the case of an auxetic material (b), under uniaxial tensile effort, the internal structure of the material is elongated both in x and y direction, which is explained by the Negative Poisson Ratio (NPR) (ALDERSON, 1999).

Figure 15 – Mechanical behavior of (a) non-auxetic material and (b) auxetic material.

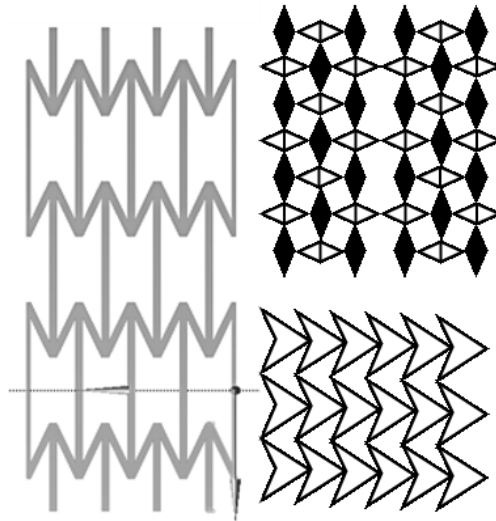


Reference: Adapted from (ALDERSON, 1999).

The NPR property is essentially provided by the geometry of the structure, and, in few cases, by the material properties. To observe the auxetic effect in a given material, there is a huge variety of structures which can be chosen in order to obtain this unique feature (BAKER, 2011). Figure 16 shows some of the structures tested and proposed in the literature, as a common feature, they have tunable geometric parameters and important gaps inside the material which are important during expansion as observed in Fig. 15 b) (LIU, 2010).

Besides, the auxetic properties are linked to the structure/geometry rather than intrinsic characteristics of the material (STEFFENS, 2012).

Figure 16 – Reentrant structures containing the auxetic effect.



Reference: Adapted from (LIU; HU, 2010).

Structures presented in Figure 16 were artificially designed; nevertheless, some materials naturally show NPR. Among these, several can be cited: Cadmium, Arsenic, Zinc, polyester (PE), polyurethane (PU), polytetrafluoroethylene (PTFE) foams, cat and cow skin, and cancellous bone (BAKER, 2011; MARDLING, 2020).

Table 5 show inherent auxetic materials and their respective Poisson's ratio.

Table 5 – Auxetic materials examples.

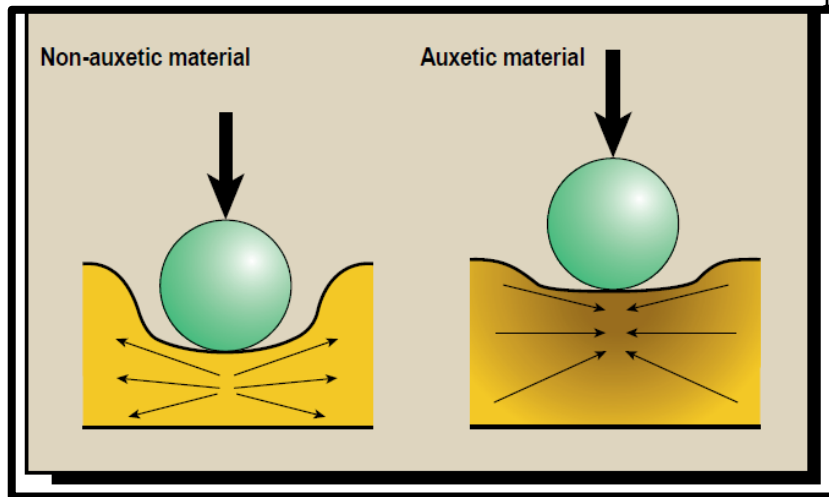
Material	Poisson's ratio (ν)
Iron pyrites	-0.14
PU foams	-0.70
Polytetrafluoroethylene (PTFE)	-12.00
Carbon fiber laminates	-0.13
Polypropylene fiber	-0.60
Pyrolytic graphite	-0.21
Cadmium oxalate	-0.26
Zinc oxalate	-0.29

Reference: (ALDERSON, 1999; COLMENERO, 2020).

Auxetic materials/structures present highly differentiated properties comparing to conventional materials. In the case of hardness, auxetic materials have a greater resistance to indentation: an auxetic structure contracts laterally when hit by an object, occurring a

material flow towards the impact point, instead of a dispersion of matter escaping from this point in the case of a conventional structure. Then, the auxetic structure will be denser in this point and, therefore, more resistant to indentation, as observed in Figure 17 (ALDERSON, 1999).

Figure 17 – Comparison between a conventional and an auxetic structure under impact loading.



Reference: Adapted from (ALDERSON, 1999).

In addition, the auxetic effect provides many advantages to the structures, such as: greater fracture toughness (K_{IC}), higher shear strength, higher capacity to absorb energy and higher damping capacity (impacts, sound waves, plastic deformation) (ALDERSON, 1999).

3.2.1.1 Auxetic structures applications

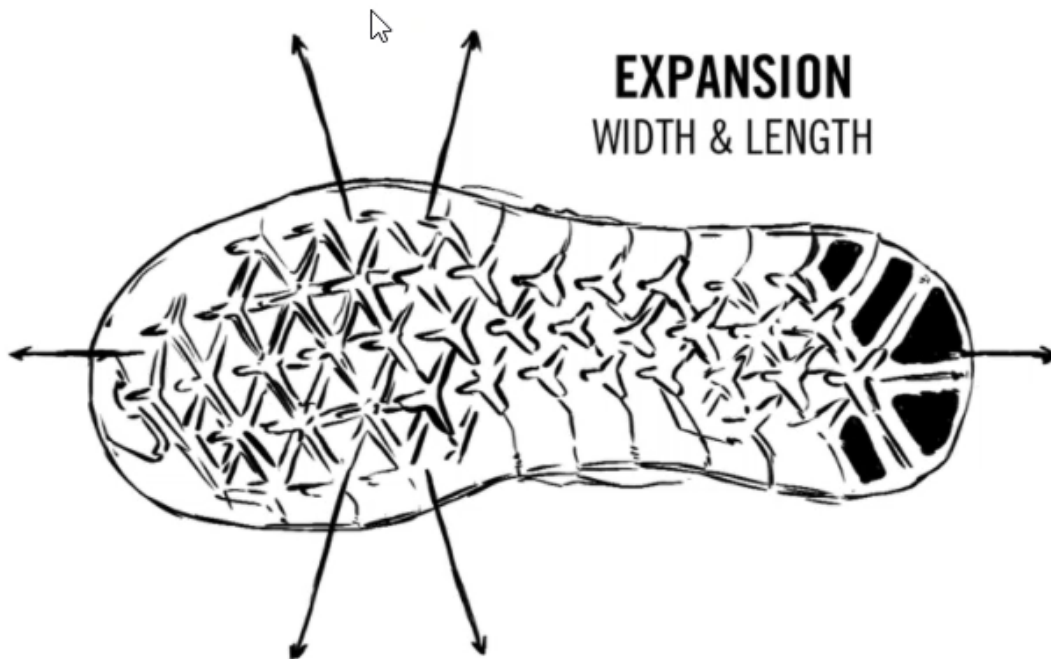
Present research in auxetic materials and structures raises great interest in many technologic sectors: biomedical, armor protection, sensors. Moreover, there is a growing variety of armor applications, which can be explored in the near future:

- Auxetic ceramics: by modifying the ceramic structure, fracture toughness would increase significantly (MOTT, 2009; BAKER, 2011);
- Auxetic armor: bearing in mind the greater resistance to indentation of auxetic structures, a new generation of lighter protective ballistic armor and helmets is being developed by companies of military equipment and textile sectors (BAKER, 2011);
- Biomedical implants with auxetic structure: a blood vessel containing an auxetic metallic stent could have an increase in its thickness as a response to a pulse of blood

flowing through it, resisting to an eventual rupture due to wall thinning (LIU, 2010); Orthopaedical devices such as an auxetic polyurethane cervical collar intended to treat several cervical spine pathologies were also proposed in the literature (PANICO, 2017)

- Auxetic tissues and foams: textile industry searches to increase quality and the durability of their products. A great investment has been made in the conception of textile materials with higher added technology – higher work life, higher durability, higher corrosion resistant, lower weight (HIBBELER, 2011). Adaptive children clothes by Petit Pli® have been developed using auxetic geometries (PAOLETTI, 2021). Complementarily, several advances in auxetic foams for shoes have been observed: Nike developed a specific line of shoes called Knit (Figure 18) which use a patented auxetic sole (CROSS, 2016). Under Armour also developed innovations on their shoes creating auxetic skins and soles (TORONJO, 2015).

Figure 18 - Nike Knit auxetic sole.



Reference: adapted from (NIKE, 2018).

- Sensors/actuators: since auxetic materials have a high-volume ability, they are being used to enhance sensitivity of piezoelectric devices (BAUGHMAN, 1998).

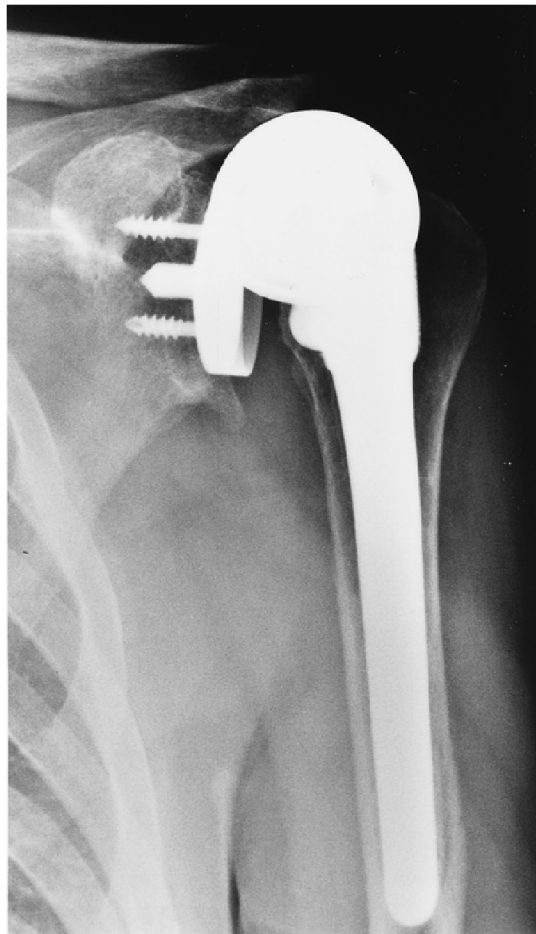
3.2.1.2 Auxetic structures in tissue engineering

Besides armor applications, auxetic structures can be also employed as biomaterials. Bone tissue can be described, in the Materials Science point of view, as a composite structure composed of 90 – 95% collagen fibers and 5 - 10% extracellular matrix (HALL, 2011). One of its main characteristics is to respond to external stimulus, both physical and chemical, in order to tolerate the function demands of the human body. Therefore, auxetic structures can be considered as smart materials, as they are able to modify their shape and contain multimaterial setups that bring further degrees of freedom to fabrication (SCARPA, 2016). Materials with auxetic structure can answer in a contra-intuitive manner to mechanical forces, becoming more resistant as an increasing force is applied to it and thicker when pulled uniaxially due to NPR property (ALDERSON, 1999; EVANS, 2000).

Many biomedical applications are possible using this interesting type of structure: devices for arterial recanalization and the promising field of bone defects filling in orthopedic surgeries or even in prostheses capable of becoming more resistant and resilient in specific points where it is necessary with the increase of mechanical effort. This makes possible the fabrication of lighter and more resistant prostheses or even in osteosynthesis materials (materials used in fracture reparation of osteotomies, plates, screws and intramedullary rods) more resistant to fatigue. In the following a detailed description of each one of these possibilities (WIRTH, 1996).

- Filling of bone defects: in some orthopedic surgeries, such as the case of tumors or osteotomies (bone cuts), in order to realign bone tissues, creeps or empty spaces are formed and need to be filled. Biologic material can be used as bone graft or porous titanium blocks can be inserted in these spaces and it will gradually adhere to the adjacent bone in the border of the bone defect. However, it is expected that beyond having a porous surface for bone adhesion, a component (Figure 19) made of an auxetic material would become more resistant after being compressed and also expand and contract with micro movements (according to the forces applied to it). In this way making the bone could be stimulated to grow and adhere in less time with higher efficiency (WIRTH, 1996).

Figure 19 – Metallic prosthesis showing displacement of the component after total shoulder arthroplasty.



Reference: Adapted from (WIRTH, 1996).

- Arthropathies: when some articulation is degenerated, with an important wear causing pain and function limitation, one of the treatment options is the articulation substitution for prostheses, such as hip, knee, shoulder or ankle. With time, wear occurs in these prosthesis' components, that can lead to loosness, important metal ion release and prosthesis degradation (HANAWA, 2004), prosthesis detachment, making necessary a prosthesis review and further observation or its eventual substitution. However, in the changing process, bone tissue loss can occur in the surrounding area (MARDLING, 2020). With auxetic structures, lighter prostheses may be produced, which answer to mechanical forces being applied to it and which are also more resistant in specific points where higher strength is required, in this sense, an innovative intervertebral disc containing auxetic honeycomb structure can be applied to avoid disc protrusion and nerve injury (MARTZ,

2005). More recently, this auxetic design has been enhanced including two discs with auxetic lattice structure linked by a pivot point (SABATINO, 2014).

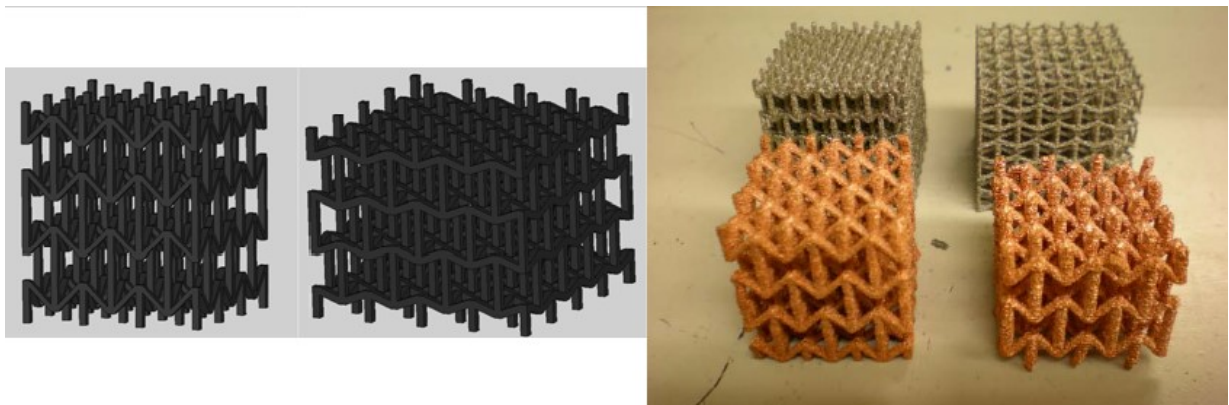
- New osteosynthesis materials: in the breakdown of a bone, many times it is necessary some type of temporary support to keep it in the right position while consolidation and healing occurs. This is done by using plates, screws or intramedullary rods. According to Rockwood (WIRTH; 1996), the main issue about principles of fracture treatment, after implanting an osteosynthesis material begins bone tissue consolidation in parallel with fatigue phenomena of the implant. The biggest problem happens when the implant fails by fatigue (or another failure mechanism) before the complete consolidation of bone tissue. Among the reasons for fatigue is the production of indentations during the implant process. One of the main characteristics of auxetic materials is a greater resistance to indentations.

3.2.2 Present research in auxetic structures

Given the geometry and a specified material, SLM can be used to create complex structures, which can show auxetic properties. In the literature, no studies were found over the production of auxetic structures by SLM.

Nevertheless, two complementary studies from *Yang et al* (YANG, 2011; 2012) present the production of Ti-6Al-4V and Cu auxetic structures using Electron Beam Melting (EBM). These structures were proven to be auxetic with Poisson's ratio of -0.5 and -1.5 for different geometry parameters. Figure 20 shows the aforementioned structures.

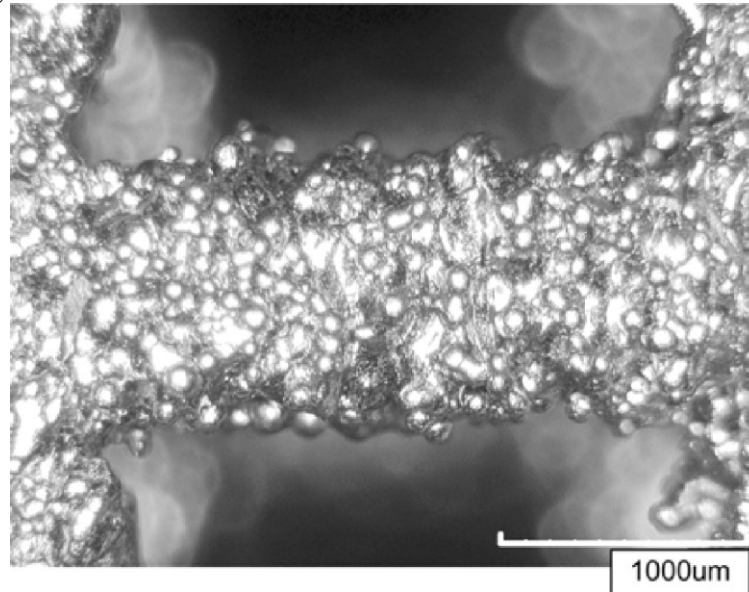
Figure 20 – At left auxetic CAD models; right-side: EBM Ti-6Al-4V and Cu auxetic structures.



Reference: Adapted from (YANG, 2011).

The surface of finished parts presented a very high roughness, due to intense heat dissipation during EBM process. As a direct consequence of high thermal flux during production, balling effect appears. Figure 21 reveals the surface of Ti-6Al-4V part made by EBM.

Figure 21 – Surface of EBM struts from auxetic structures.



Reference: (YANG, 2012).

In this same study, *Yang et al.* (YANG, 2012) performed mechanical tests on Ti-6Al-4V and Copper samples. The former presented a failure mechanism under compression similar to a brittle material. Two different designs were tested, D1 and D2. Geometric parameters are presented in Table 6:

Table 6 – Geometric parameters of Ti-6Al-4V auxetic structures.

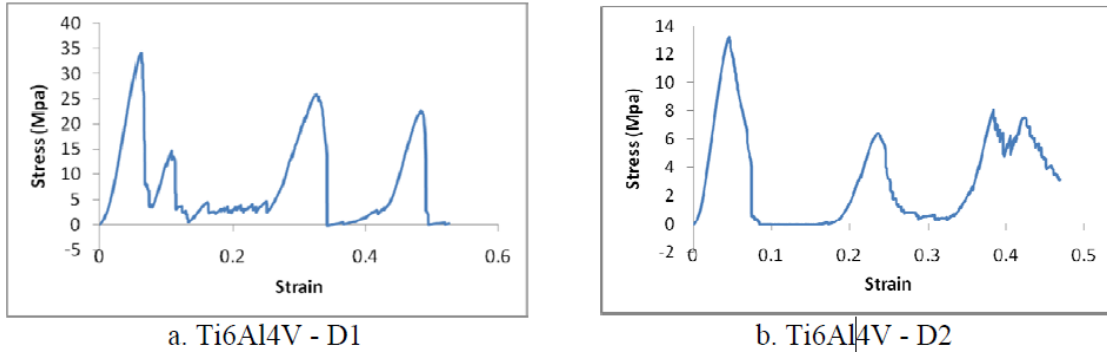
Design	Compressive Strength (MPa)	E (MPa)	Energy absorption / volume (MJ/m ³)	Energy absorption / weight (kJ/kg)	Poisson's ratio (ν)
D1	31.8 ± 1.3	2.2 ± 0.6	0.6 ± 0.2	1.0 ± 0.3	-0.463
D2	12.9 ± 0.5	0.6 ± 0.1	0.4 ± 0.1	0.8 ± 0.1	-1.496

Reference: (YANG, 2012).

Moreover, since the structure repeats itself within a given range, the stress-strain curve presents a cyclic behavior (Figure 22). The abrupt decrease in stress results from the breaking of each auxetic structure layer (Figure 23). After breaking one layer, loading

becomes more stable and, as the next layer is reached, stress increases dramatically until layer damage is critical.

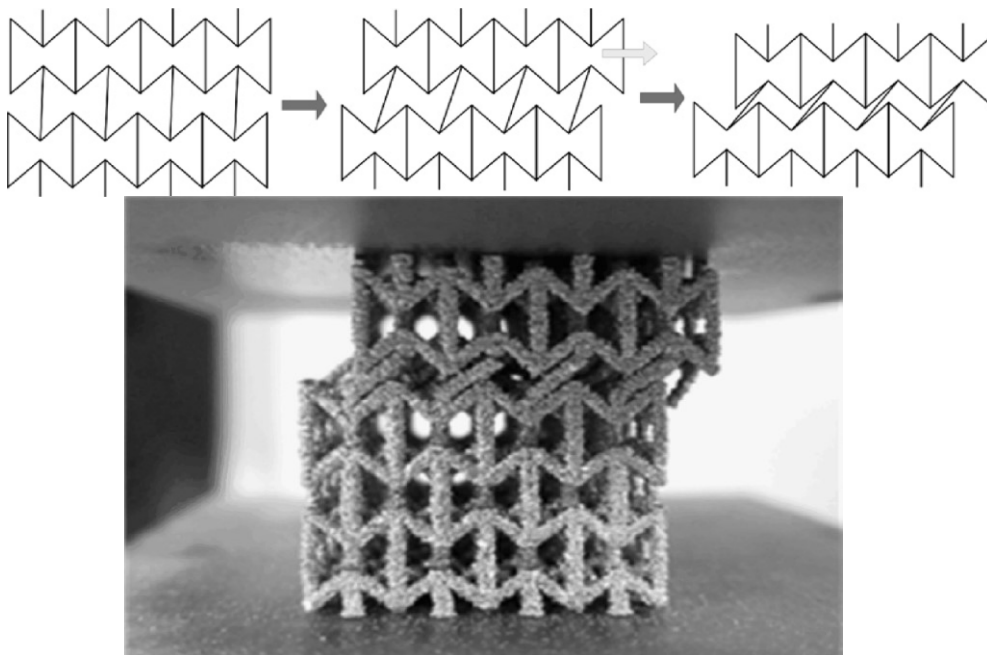
Figure 22 – Stress - Strain curves for two different Ti-6Al-4V structures (D1 and D2).



Reference: (YANG, 2011).

Structure failure behavior is represented on Figure 23: struts linking each layer of the auxetic parts are progressively damaged until plastic deformation occurs.

Figure 23 – Failure behavior of EBM auxetic sample based on Ti-6Al-4V.



Reference: adapted from (YANG, 2011).

Mechanical properties for Ti-6Al-4V D1 and D2 samples were calculated and summarized in Table 7: Variations in geometric parameters of the structures resulted in

different degrees of auxeticity. Structure D2 presents lower strength and elastic moduli compared to structure D1. Nevertheless, regarding energy absorption, both designs are comparable. Finally, the authors argue that, for energy absorption applications, structures with higher \NPR are preferable, i.e., D2.

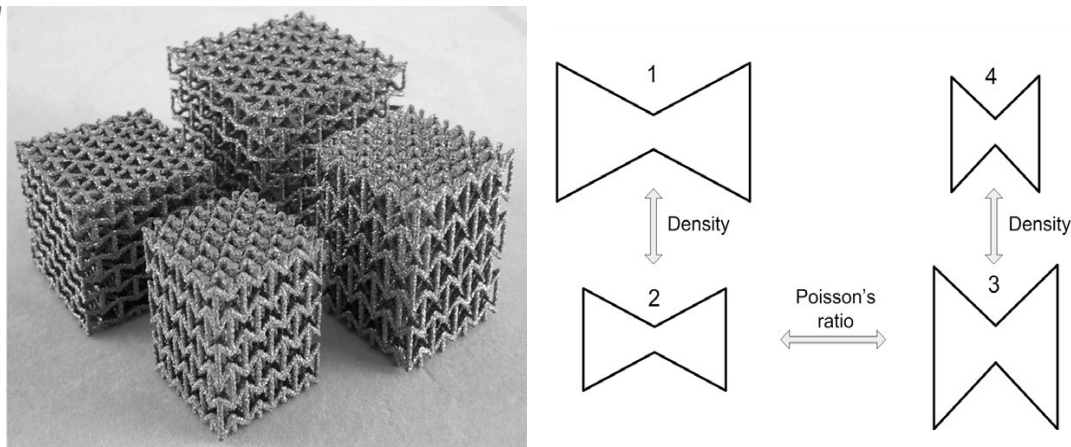
Table 7 – Mechanical properties for Ti-6Al-4V D1 and D2 structures.

Design	Compressive Strength (MPa)	E (MPa)	Energy absorption / volume (MJ/m ³)	Energy absorption / weight (kJ/kg)	Poisson's ratio (ν)
D1	31.8 ± 1.3	2.2 ± 0.6	0.6 ± 0.2	1.0 ± 0.3	-0.463
D2	12.9 ± 0.5	0.6 ± 0.1	0.4 ± 0.1	0.8 ± 0.1	-1.496

Reference: (YANG et al., 2011).

In another study, *Yang et al.* (YANG, 2012) created auxetic structures based on Ti-6Al-4V using EBM. Implementing an optimization routine of previously studied structures (YANG et al., 2011), four different designs were created, presented in Figure 24 (similar to those presented in Figure 23).

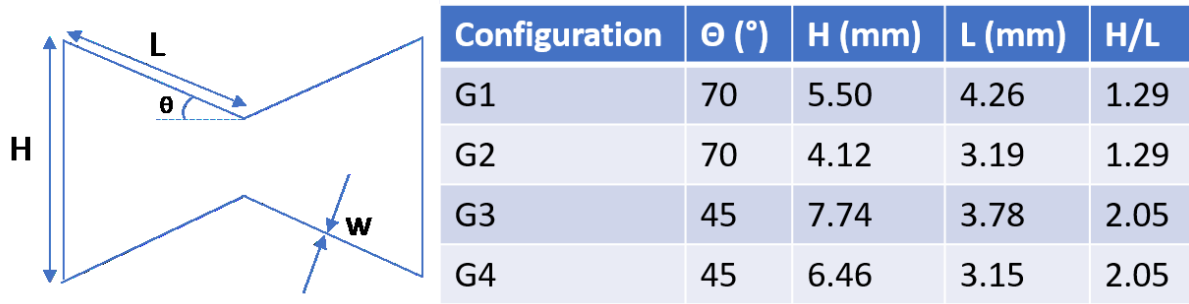
Figure 24 – EBM auxetic structures based on Ti-6Al-4V.



Reference: (YANG, 2012).

Geometries 1 and 2 presented different dimensions and density but the same ν : -0.367. Geometries 3 and 4 presented different dimensions and densities but the same ν : -1.899. Figure 25 reveals the designs and its main features: two H/L ratios were used – 1.29 and 2.05; angle theta was used in two values – 45° and 70°; finally, strut size was fixed as 0.8 mm for all designs.

Figure 25 – Auxetic designs specifications.



Reference: adapted from (Yang, 2012).

Structures G3 and G4 presented much higher compressive strength, elastic moduli and negative Poisson's ratio than the structures D1 and D2. Values of these mechanical properties are summarized in Table 8.

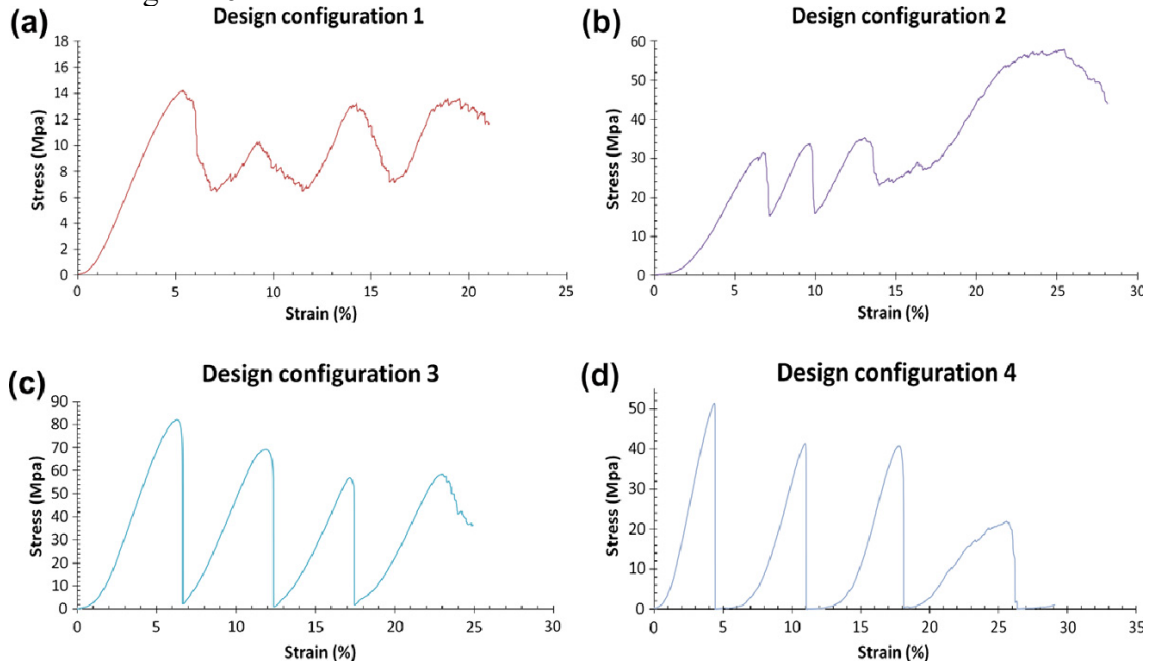
Table 8 – Mechanical properties of G1 – G4 auxetic structures.

Design	Compressive Strength (MPa)	E (MPa)	Relative density (%)	Poisson's ratio (ν)
G1	13.4 ± 0.7	529.8 ± 54.1	13.6 ± 0.2	-0.367
G2	30.2 ± 2.5	1180.6 ± 60.5	22.9 ± 0.1	-0.367
G3	49.3 ± 4.1	2980.3 ± 181.5	21.6 ± 0.4	-1.899
G4	76.3 ± 6.5	5085.3 ± 576.2	31.1 ± 0.5	-1.899

Reference: (YANG et al., 2012).

Stress strain curves for each auxetic structure are shown in Figure 26. Regarding the behavior of auxetic structures under compression (Figures 26 (a) – (d)), cycles of load and breaking are observed in all cases (as observed for samples D1 and D2). For designs 1 and 2, after the first layer is broken, the stress remains at a higher level. For design configuration 2, it can be assumed that at the maximal load, a densification of the structure occurs, maximizing compressive strength. Designs 3 and 4 reveal mechanical behaviors very similar to D1 and D2 cases.

Figure 26 – Stress - strain curves for different auxetic structures.



Reference: (YANG et al., 2012).

Usually, it was observed that Poisson ratio has a more significant influence on compressive strength and elastic modulus. *Alderson* (ALDERSON, 1999) stated that this was an intrinsic property from auxetic structures. On the other hand, density is more affected by geometry arrangement and strut size.

Another remarkable feature is that, by changing dimensional parameters (re-entrant strut angle and the ratio of vertical to reentrant strut length) ν can be easily modified. Added to that, strut length plays a significant role in density and compression strength. Therefore, by tuning all these parameters, a structure can be obtained with targeted values of strength or stiffness for a given application.

3.2.3 Auxetic high energy absorption impact applications

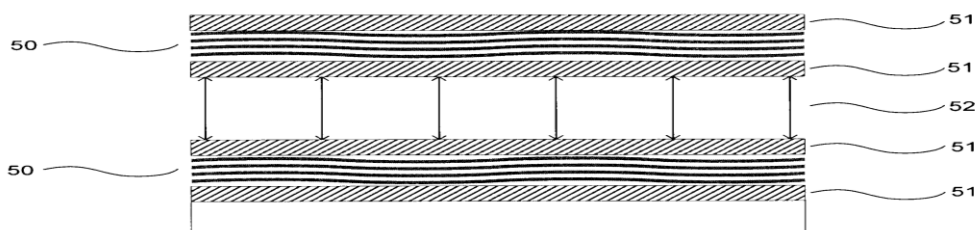
Based on the auxetic properties presented in section 3.2.1, there is a growing interest in developing specific applications in ballistic research

In the literature, up to date only one patent on auxetic armor was proposed: Composite auxetic armor by *Skertchly* (SKERTCHLY, 2011).

This patent includes at least a ceramic armor plate with an auxetic reinforcement that can be in fiber, knit or weaves form. According to the inventor, the auxetic component reduces cracking of the ceramic plate (SKERTCHLY, 2011).

Figure 27 reveals a section of the proposed auxetic armor: Element 50 is an auxetic layer; element 51 is a ceramic plate and element 52 is a junction to another part of the composite structure. Still, no claims are made regarding efficiency of the composite auxetic armor.

Figure 27 – Auxetic composite armor.



Reference: (SKERTCHLY, 2011).

3.3 PARAMETER INFLUENCE IN SLM

SLM presents a wide set of parameters, which must be well mastered to produce parts with controlled properties. Main parameters are laser power, scan speed, layer thickness, powder specifications (size distribution and morphology of particles), overlap rate and direction of building, sintering atmosphere. Some of these parameters can be modified (controllable - Ctrl) and others are pre-set from the SLM machine (predefined - Prdf). Table 9 summarizes main laser and scanning parameters present in SLM process (HANZL, 2015).

Table 9 – Laser and scanning parameters in SLM method.

Parameter	Description	Controllable (Ctrl) or Predefined (Prdf)
Average power (PL)	Measure of total energy output of a laser	Ctrl
Mode	Continuous wave or pulsed	Prdf
Peak power (Ppeak)	Maximum power in a laser pulse	Prdf
Pulse Width (PW)	Length of a laser pulse when operating in pulsed mode	Prdf
Frequency (f)	Pulses per unit time	Prdf
Wavelength (λ)	Distance between crests in laser electromagnetic waves	Prdf
Polarization	Orientation of electromagnetic waves in laser beam	Prdf
Beam quality (M)	Related to intensity profile and used to predict how well the beam can be focused and determine minimum theoretical spot size (=1 for a Gaussian beam)	Prdf
Intensity profile I (x,y,t)	Determines how much energy added at a specific location	Prdf
Spot size (dx and dy)	Length and width of elliptical spot (equal for circular spots)	Ctrl
Scan velocity (v)	Velocity at which laser moves across build surface	Ctrl
Scan/Hatch spacing (Ss)	Distance between neighboring laser passes	Ctrl
Scan strategy	Pattern in which the laser is scanned across the build surface (hatches, zig-zags, spirals) and associated parameters	Ctrl

Reference: Adapted from (HANZL, 2015).

Moreover, there is a specific set of parameters which are related to powder material properties. The properties of the powder material will influence the choice of several laser and scanning parameters. These properties are shown in Table 10 (Controlled: ctrl; Predefined: Prdf).

Table 10 – Powder material properties in SLM process.

Parameter	Description	Controllable or predefined
Bulk density (ρ_b)	Material density, limits maximum density of final component	Prdf
Thermal conductivity (k_b)	Measure of material's ability to conduct heat	Prdf
Heat capacity (c_p, b)	Measure of energy required to raise the temperature of the material	Prdf
Latent heat of fusion (L_f)	Energy required for solid-liquid and liquid-solid phase change	Prdf
Melting temperature (T_m)	Temperature at which material melts	Prdf
Boiling temperature (T_b)	Temperature at which material vaporizes	Prdf
Coefficient of thermal expansion (α)	Measure of volume change of material on heating or cooling	Prdf
Material absorptivity ($A_{b,m}$)	Measure of laser energy absorbed by the material, as opposed to that is transmitted or reflected	Prdf
Particle size distribution	Distribution of particle sizes, usually diameter, is a powder sample	Prdf

Reference: Adapted from (HANZL, 2015).

Another set of parameters which are related to sintering atmosphere must be also considered: type of inert gas, oxygen level, ambient temperature and pressure. These parameters are presented in Table 11.

Table 11 – Environment parameters in SLM process.

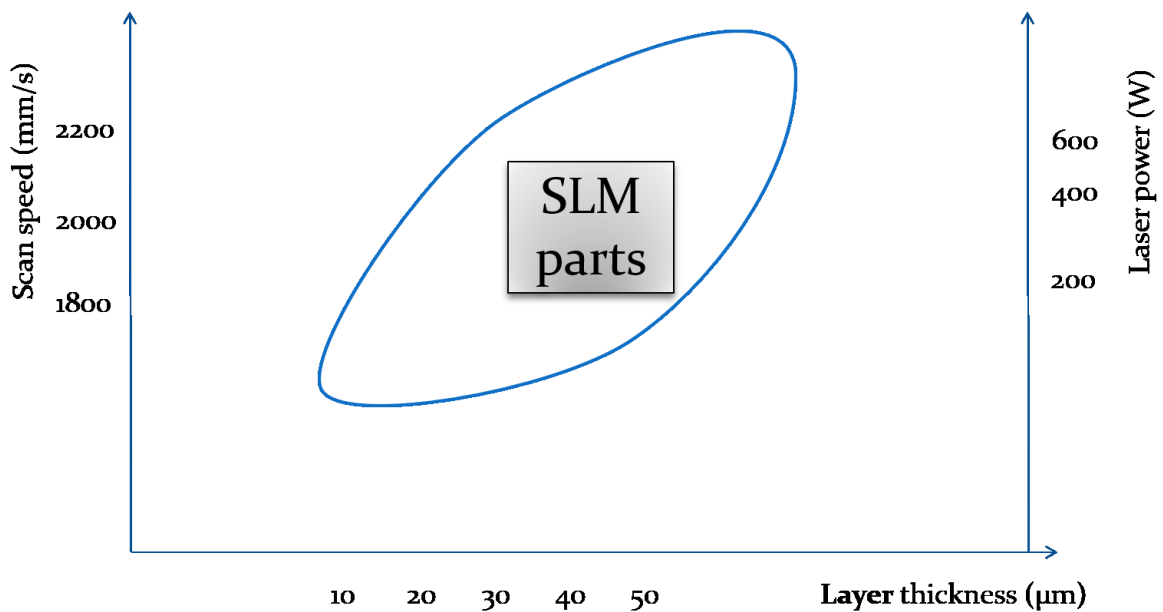
Parameter	Description	Controllable or predefined
Inert gas	Usually Ar or N ₂ , but may also be He, or another gas	Ctrl
Oxygen level (%O ₂)	Probably most important environmental parameter, oxygen can lead to oxide formation in metal, change wettability	Prdf
Ambient temperature (T_{amb})	May impact powder preheat and residual stress	Ctrl
Pressure (P)	Influence vaporization of metal as well as oxygen content	Ctrl

Reference: Adapted from (HANZL, 2015).

Part's mechanical properties will change for each set of SLM parameters. For instance, higher laser power can increase density and hardness, but it can also increase crack length, propagation and higher fragility to the fabricated part. For each material, there is a thin window to choose and optimize processing parameters to obtain a part with the

mechanical properties specified in its project/use: as such, three parameters – laser power’, layer thickness and scanning speed - among several present in SLM processing were analyzed in the literature. Typically, parameter values in SLM fabrication are found in the following intervals: laser power – 200 to 600 W; layer thickness – 30 to 50 μm ; and, scanning speed – 1800 to 2100 mm/s (Figure 28).

Figure 28 - Optimal SLM parameters: laser power, layer thickness and scan speed.



Reference: Own authorship, 2018.

SLM parameters are very specific to each class of material and also to a given geometry. Several cases have been related in the literature that, for a material fabricated with different geometries, there is a need to modify SLM parameters in order to obtain a dense part.

In a first approach, the following parameters will be considered: laser power and respective types; scan speed and scan strategies; powder specifications.

3.3.1 Laser power

In most cases, laser power and scan speed are interdependent since both determine the energy which will be transferred to the powder, causing it to melt and then promote sintering. *Gu et al.* (GU, 2008) considered the combination of laser power and scan speed in

Stainless Steel 316L parts with layer thickness of 20 μm produced by DMLS. For each set of these parameters, different types of melting are produced (Figure 29 (a)):

I. No melting: delivered beam energy was insufficient to melt the powder and, thus, a large amount of powder remained in its initial state or partially sintered.

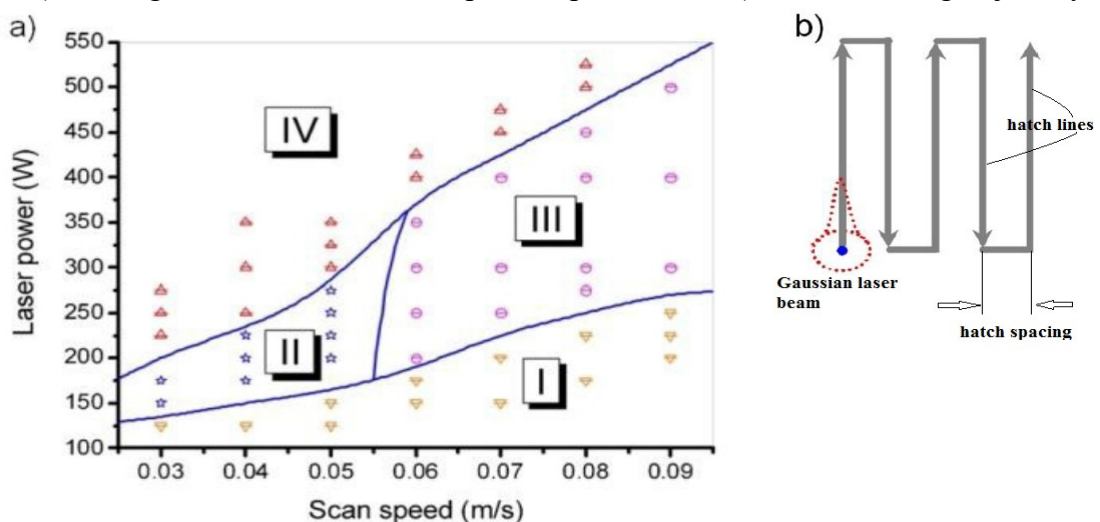
II. Partial melting: Medium beam performance in combination with a low scanning speed ($< 0.06 \text{ m/s}$) formed a liquid phase on the particles' surface. This phase will bake together the unmelted cores of particles into coarsened balls with about the diameter of the laser beam after crystallization. This surface shows the first type of balling phenomenon, as presented in Figure 21.

III. Melting with balling phenomenon: At a high laser output and a high scanning speed ($\geq 0.06 \text{ m/s}$) the shapes made by the melting track, as seen on the surface, were long, thin cylindrical lines, which later split up into rows of coarse beads. This was a result of the reduction of surface tension.

IV. Complete melting: The laser energy was so great that permanent tracks of molten metal material were created. The tracks formed continuous lines of fully melted compact solid surface.

Typical laser beam antiparallel trajectory is shown in Figure 29 (b): in each powder layer, the laser beam follows alternate hatch lines which are separated by the Ctrl-parameter scan/hatch space. This distance is greater than the powder zone irradiated by the laser beam.

Figure 29 – a) Melting mechanisms related to process parameters; b) Laser scanning trajectory.

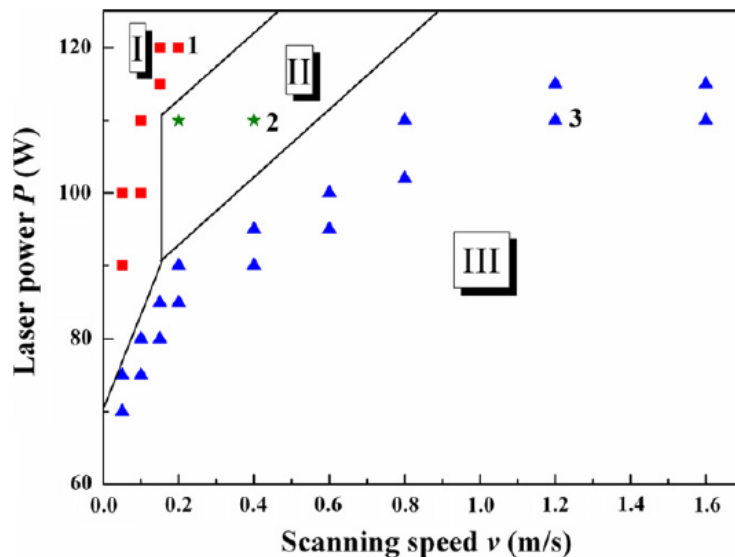


Reference: Adapted from (GU, 2008).

For other materials, such as Ti-6Al-4V, different ranges of values for laser power and scan speed apply: in normal conditions, 110 W and 400 mm/s (0.4 m/s) can create dense parts, with powder bed layer thickness of 50 μm (SONG, 2012). In a study by *Song et al* (SONG, 2012), several densification tracks were produced to understand melting mechanisms present in Ti-6Al-4V produced by SLM, as such, three different zones were identified (Figure 30):

- I. Melting with cracks: this track was produced with high laser power and low scanning speeds, creating large amount of RS, resulting in an average density 3.87 g/cm^3 .
- II. Continuous melting: ideal combination of energy input and scan speed, creating a track with few defects and low RS. In this zone, the highest density was observed – 4.13 g/cm^3 .
- III. Partial melting: in this track, laser power is insufficient to produce complete melting of Ti-6Al-4V powder, creating weak bonds between powder grains and large void regions, resulting in the lowest density of 2.91 g/cm^3

Figure 30- melting zones of Ti-6Al-4V.



Reference: Adapted from (SONG, 2012).

Moreover, both thermal conductivity and thermal capacity are temperature-dependent parameters. This implies that, at higher temperatures, melting occurs with more

ease. Therefore, an increasing laser power can theoretically perform faster production of parts.

Nevertheless, if an excessive laser power is applied, balling effect and thermal stresses will be increased leading to defects (cracks, porosity, voids, RS) formation. For each material, there is a set of optimal parameters for AM processing (GU, 2015).

In SLM method, several types of laser can be used, such as CO₂, Fiber, Nd:YAG, excimer. Nowadays, fiber laser has the greatest usage in SLM machines due to its versatility and lower acquisition operation costs compared to Nd:YAG and excimer types (CONTROLLASER, 2020). Material processing has an influence over the choice of the laser: since each laser has a specific wavelength it scatters different light frequencies. Table 12 summarizes laser types, nature, principle, wavelength, specific material application and power range.

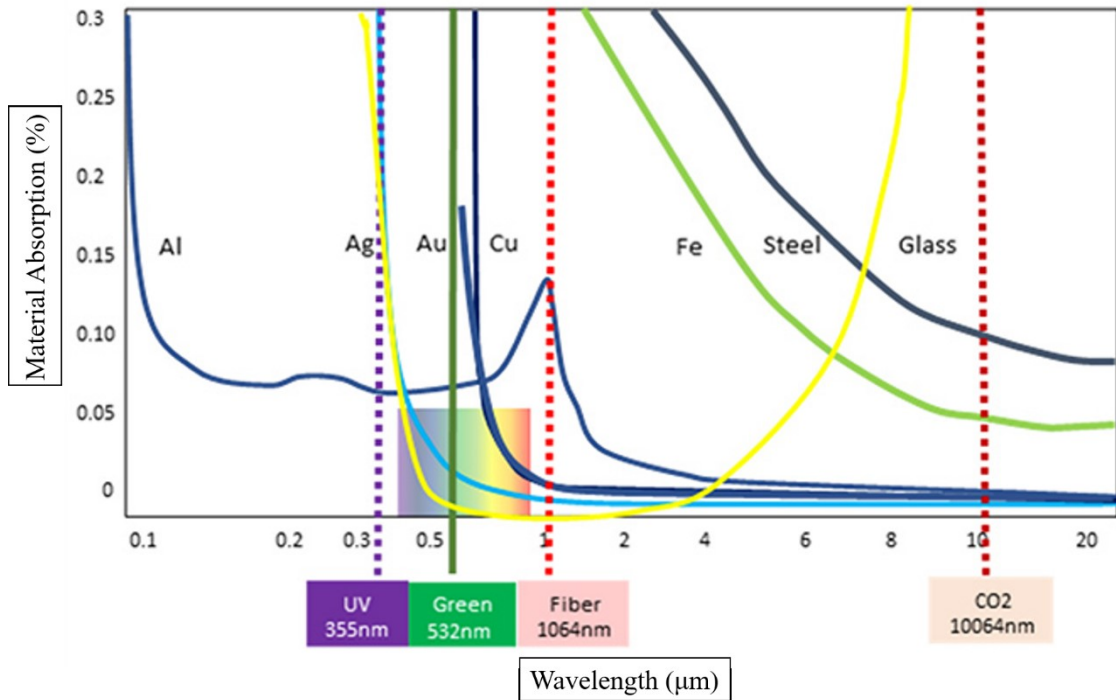
Table 12 – Laser types and intrinsic characteristics.

Laser type	Nature	Principle	Wavelength (nm)	Suited materials / application	Typical power range
CO ₂	Gas	Plasma ionization	10600	Polymers; glasses;	1 mW to 100 W
Fiber	Solid state	Doped (Er, Yb, Tm) optical fiber	1064	Metals	1 W to 20 kW
Nd:YAG	Solid state	Nd diffused in an Yttrium Aluminum Garnet	1030	Metals	10 W to 30 kW
Excimer	Solid state	Excited compounds (XeCl, KrF, ArF) that undergoes stimulated or spontaneous emission	126 - 360	Eye surgery; Photolithography; microelectronic devices	25 mW to 100 mW

Reference: (KRUTH, 2003; STEEN, 2003).

Fiber laser can operate in wavelengths of 0.25 – 2.25 μm, which is a region of optimal optical absorption for metals such as Iron, Copper and Aluminum. Figure 31 reveal the relation between optical absorption and wavelength for gold, aluminum, iron, steel, silver, copper and glass (CONTROLLASER, 2020).

Figure 31 – Optical absorption (%) of metals versus wavelength.



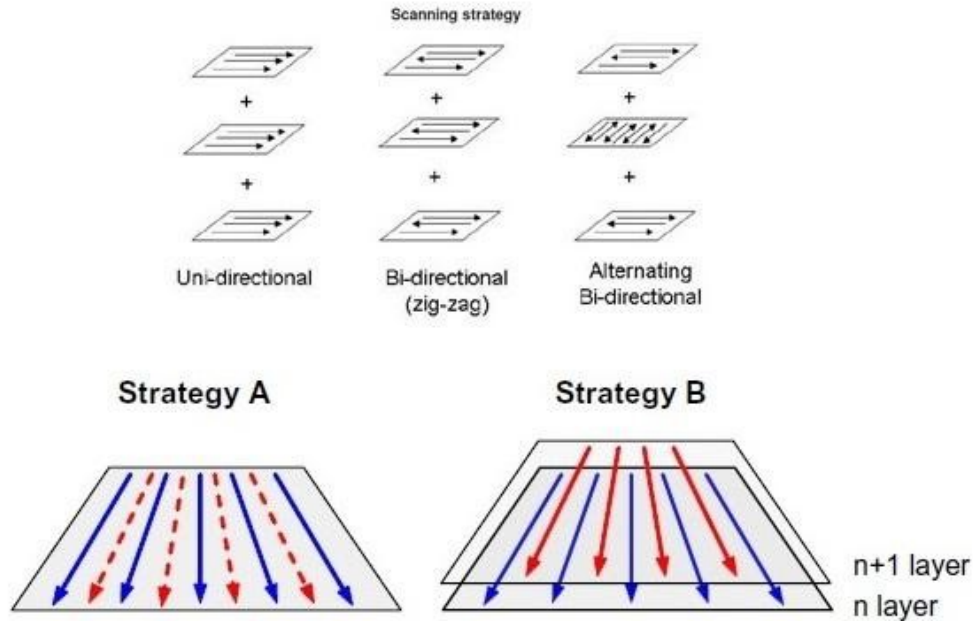
Reference: Adapted from (CONTROLLASER; 2020).

3.3.2 Scan speed and scan strategies

Scanning speed (V) corresponds to the speed by which the laser is brought to the powder bed. On the other hand, scanning strategies refer to the path followed by the laser beam in order to build an object. To build an object, a combination of several scan strategies and different scanning speeds can be applied (HANZL, 2015).

Many scanning strategies can be adopted, among them the most used are: zig-zag, unidirectional, bidirectional. Moreover, other scan strategies can apply, as Strategy A in which the laser alternates between higher intensity (blue lines) and lower intensity (red dashed lines) on the powder bed. In strategy B, a different approach is used: laser passes with different hatch spacing through powder layers. Each of these scan strategies have an influence on the sintered part properties, e.g., density, anisotropy and mechanical strength, as shown in Figure 32 (GIBSON, 2015).

Figure 32 – Scanning strategies used in SLM.



Reference: Adapted from (GIBSON, 2015).

3.3.3 Metal powder specifications

Metal powder plays a very important role in SLM process. Quality and characteristics of this powder will determine the properties of the final part. A poor prepared powder will generally imply in a high rate of manufacturing failure or in high concentration of defects, RS and fragility on the fabricated component.

Typically, it is desired that the powder used in SLM method follow a series of given specifications (THIJS, 2010):

- Powder prepared by atomization (gas or plasma atomization).
- Spherical or near-spherical particles generally favor close-packing, and, consequently a higher densification rate.
- A homogeneous size distribution (Gaussian distribution).
- High purity.
- A good flowability.
- Small grain size of particles (typically dozens of micrometers).

Additionally, thickness and orientation of each powder layer are important parameters of SLM processing. The choice of thickness has to be a compromise between building time and surface roughness (TUCK, 2015).

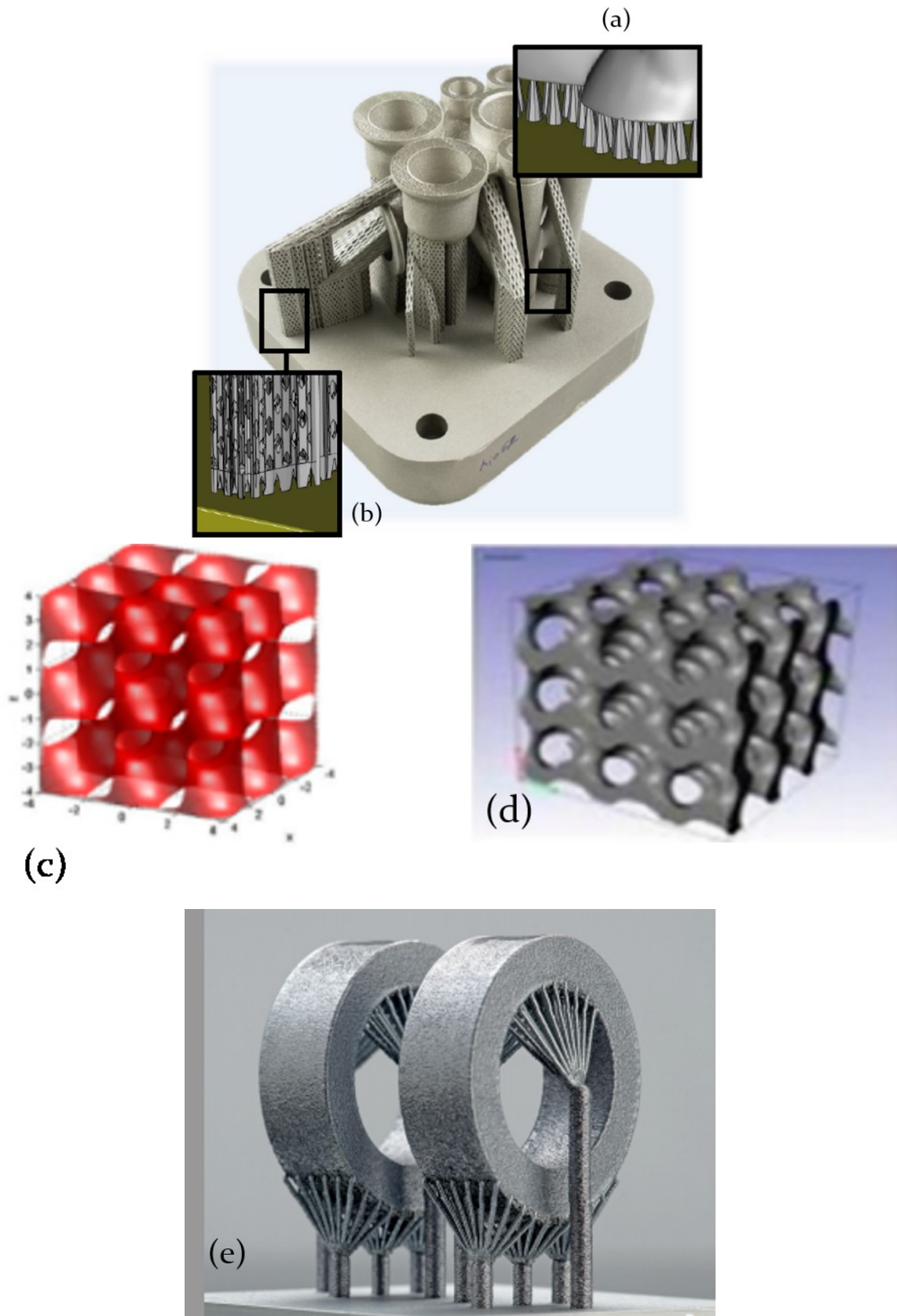
Chemical composition, size and morphology of particles, optical and absorption properties and heat transfer are also features that have to be considered in the powder specifications of SLM process (SONG, 2012).

3.3.4 Support types

In SLM, supports are substructures that have as main function the absorption of thermal stresses, optimization of heat flux, and, mechanical support and anchoring. There are two fundamental types: teeth form and cone form (Figure 33 (a) and (b)) (VTT/NURMI, 2017).

Teeth form is more fragile and easier to remove, whilst providing average anchoring. In the other hand, cone form is useful in critical zones as it adds strong anchoring to the part under fabrication. More recently, other substructures have been tested and proposed: cellular (Figure 33(c)), lattice (Figure 33 (d)) (JIANG, 2018) and Y/IY form (Figure 33 (e)) (ILT, 2016). Among those supports, type Y/IY (Figure 33(e)) has been proposed considering an urgent need in SLM fabrication: optimization of post-processing steps and higher precision in the removal of substructures through automated cutting (ILT, 2016).

Figure 33 - support types: cone form (a); teeth form (b); cellular (c); lattice (d); I/IY (e).



Reference: adapted from (ILT, 2016; JIANG, 2018; VTT/NURMI, 2017).

3.4 PHENOMENA IN SLM PROCESSING

3.4.1 Oxidation

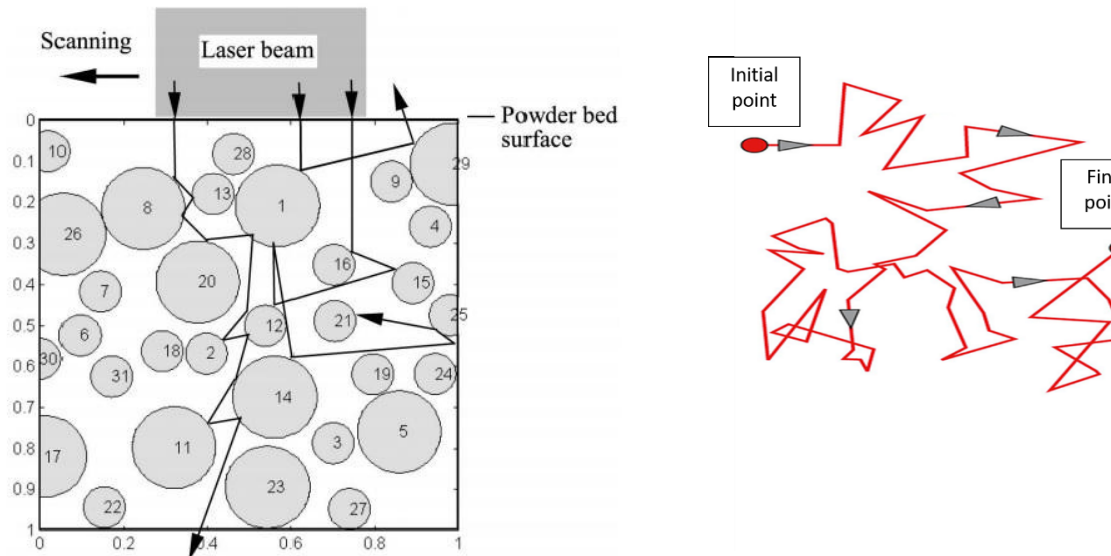
During SLM process, oxidation can occur in the absence of controlled atmosphere. More recently, SLM equipment have incorporated the option to introduce different gas types, high precision oxygen sensors and also produce primary vacuum. Inert gases such as argon, helium and nitrogen can prevent oxidation to occur even at higher temperatures.

Under the presence of high O₂ concentrations, oxide films can be formed during sintering. Nevertheless, it is generally accepted that oxide films have negligible effect on SLM as long as they are thin enough to be disrupted and stirred in the melt pool by the laser beam (GIBSON, 2015). Oxide film formation mechanism is different for each type of metal system or alloys, because every element has a specific oxygen affinity (EARNSHAW, 1997).

3.4.2 Absorption and reflection

SLM method is based on absorption of laser energy, thus, reflection and absorption play a very significant role. When the laser beam hits the powder, a part of it is reflected and another part is absorbed. The same process occurs to the particles of the powder: a series of reflections and absorptions is observed, creating a random path, similar as observed in Brownian motion (STEEN, 2003; FRITSCH, 2020). Both patterns can be observed in Figure 34.

Figure 34 – Laser beam reflection and absorption path in powder; Brownian motion.



Reference: Adapted from (STEEN, 2003; FRITSCH, 2020).

When the powder layer is thin enough (typically $30\ \mu\text{m}$), part of the laser beam can pass through the layer and its particles. The absorbed part of the beam will produce a great amount of heat that can sinter and molten the powder particles (GIBSON, 2015).

Additionally, some properties influence absorption and reflection in materials (GIBSON, 2015):

- Wavelength (each material has its specific absorbance/transmittance curves).
- Temperature.
- Angle of incidence.
- Surface roughness and films.

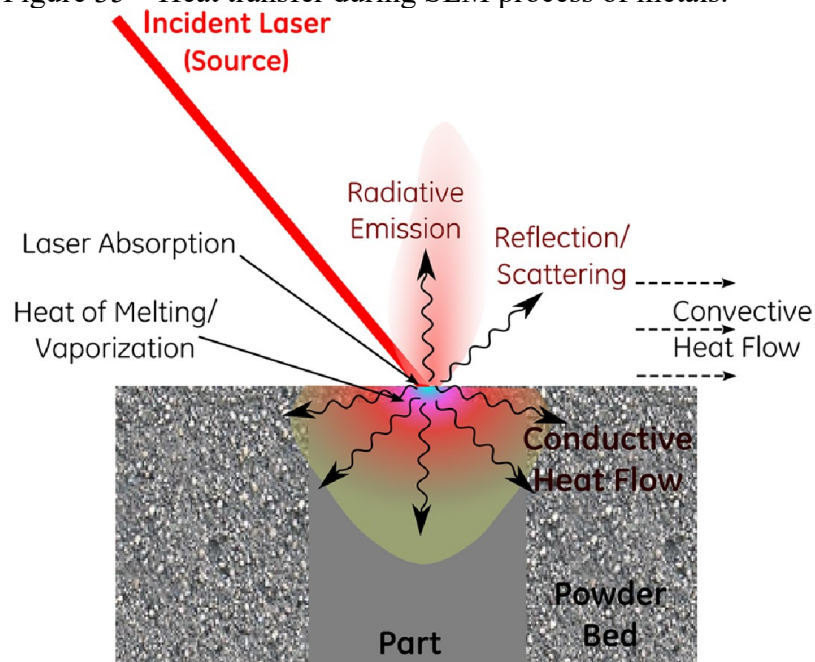
3.4.3 Heat transfer

Typically, a laser device can generate a great amount of heat in a very limited area (it is equivalent to the beam diameter plus a complementary radius). Temperature can raise up to 3500 K for a stationary laser (ZHOU, 2013).

Heat transfer depends on a series of thermal characteristics intrinsic to the powder material: heat capacity (C_p); thermal conductivity (K_T); and thermal diffusivity (α). Besides, the laser will only irradiate in a given volume, following successive reflection and absorption patterns as shown in Figure 35.

Figure 35 reveals a schematic representation of the interaction of the laser with the powder bed during SLM process: After the laser beam hits the surface of the powder bed, part of its energy is absorbed and another part is reflected or scattered. The absorbed energy generates heat, necessary to produce sintering and further melting of powder particles. Heat is propagated through the powder bed via a conductive heat flow. Depending on thermal and optical properties, a significant amount of reflection of the laser beam and also radiative emission can follow (SPEARS, 2016).

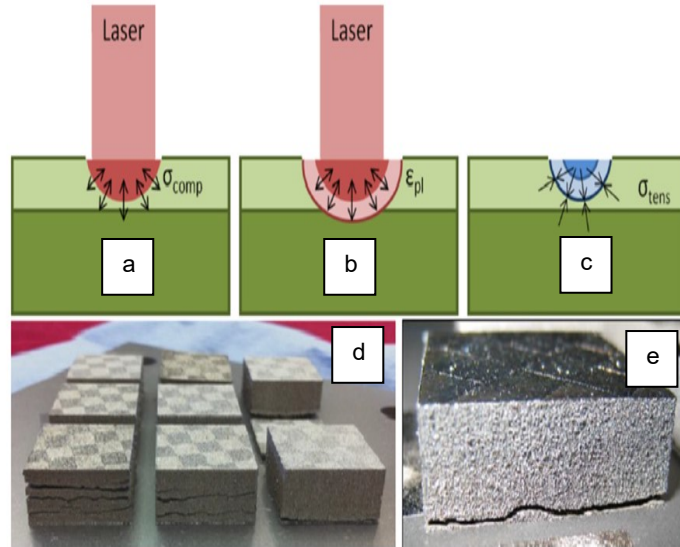
Figure 35 – Heat transfer during SLM process of metals.



Reference: (SPEARS, 2016).

A common consequence of excessive laser beam energy is the formation and propagation of cracks during the fabrication of parts, which is explained by the Thermal Gradient Mechanism (TGM), illustrated through Figure 36 (a) to (e): as the laser scans the powder bed (Figures 36 (a) - (c)), zones of compressive stresses are formed (Figure 36(a)). After heat propagation, a localized plastification zone is formed near the irradiated section of the powder bed (Figure 36(b)). As the temperature decreases, there is shrinkage of the molten powder and regions of tensile stresses are formed near the irradiated zones (Figure 36(c)). Finally, if RS concentrations are critical during fabrication, delamination and crack propagation take place in manufactured parts (Figures 36(d) and (e)). Such defects severely limit part mechanical performance and utility cycle (KEMPEN, 2014).

Figure 36 – TGM (a) - (c); Crack formation and delamination due to TGM (d) and (e).



Reference: adapted from (KEMPEN, 2014).

3.4.4 Phase transition

During SLM process, non-stoichiometric phases can be formed and can also be observed in the final part microstructure. Currently, the main issue is that phases formed during the SLM process cannot be predicted or controlled (GU, 2012).

A powerful tool to understand microstructure evolution and phase formation are numerical models such as Finite Element Method (FEM). These models simulate crystal nucleation and growth; the kinetics of mixing and melting would also be considered for different alloying elements at different temperatures (MOAT, 2009).

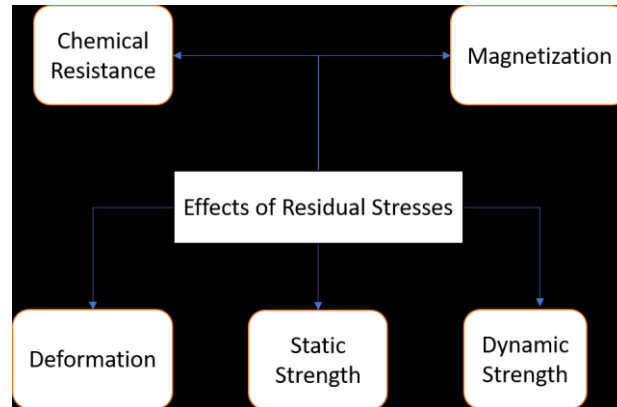
In Ti-6Al-4V processed by SLM, when cooling rate is superior to 410 K/s, martensitic transformation occurs: β phase BCC is converted to α phase HCP (YAP, 2015). This martensitic transformation and several other phases can also be obtained by means of specific heat treatments (HUANG, 2015).

3.4.5 Residual stresses (RS)

Residual stresses are self-equilibrating stresses which remain in the part after its manufacturing, even without supplementary thermal gradient and external forces. RS arise from misfits in the shape of parts, different regions, or different phases within a part, or even because of local variations of elastic constants, and thermal and mechanical properties (GUO,

2009). Also, these stresses can bring critical consequences on the part's properties: poor fatigue resistance, critical failure during operation, lower chemical resistance, lower magnetization, lower resistance to deformation, and diminished static and dynamic strength (Figure 37) (TANG, 2008).

Figure 37 – Effects of Residual Stress in materials.



Reference: Adapted from (TANG, 2008).

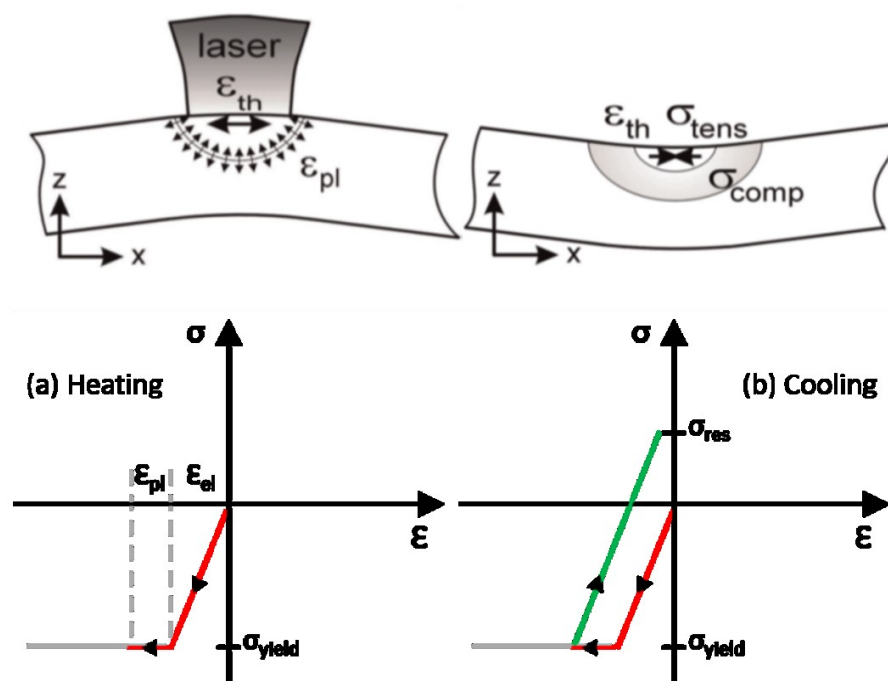
Service loading can also lead to the creation of RS and, consequently, originate inhomogeneous plastic deformation. These stresses can be found not only in the finished parts but also in the unprocessed raw material (PARRY, 2016). The origin of RS can be classified into four main categories (PARRY, 2016):

- Differential plastic flow.
- High cooling/heating rates (TGM).
- Phase transformations with volume change.
- Chemical-induced misfits.

In most of the AM processes, the rapid heating due to the source (laser/electron/plasma) leads to melting and solidification of the alloy (powder or wire-based). Repeated heating and cooling affect the local structure and properties of the components (OYELOLA, 2018). Because of such high cooling and heating rates, RS are produced, which may cause deformation, cracks and could limit the performance of materials produced by AM. Also, another direct consequence of RS is the strong anisotropic behavior that it creates in these materials (PARRY, 2016). The generation of a high quantity of RS in AM can be explained by the Temperature Gradient Mechanism (TGM) (Figure 38): Upon heating, the power source creates a series of local elastoplastic deformations (represented by

ϵ_{pl} , ϵ_{el}) and further tensile stress on the irradiated zone. In the cool down phase of the molten top layers, shrinkage occurs because of thermal contraction, leading to the generation of tensile and compressive RS regions (upper and lower layers, respectively) (OYELOLA, 2018; YAMAGUCHI, 2017). Since the AM process is very complex, TGM model represents a simplification of RS origin (YAMAGUCHI, 2017). Many factors affect the intensity and creation of RS: material properties (grain size, heat capacity, porosity/voids, phase composition), geometry of specimens, support structure (when required), and process parameters (laser/electron beam power, preheating type, scan strategies and speed, and layer thickness) (PARRY, 2016; YAMAGUCHI, 2017). In addition, many factors influence the estimation of RS. Those are summarized in Table 13 (PORTELLA, 2018).

Figure 38 – TGM. Stresses and deformation during heating (a) and cooling down (b) in the irradiated zone.



Reference: (YAMAGUCHI, 2017).

Residual stresses can be classified according to the length scale on which they occur (ABA-PEREA, 2016):

- Type I: Macro RS which equilibrate over large distances and cause a deformation of the part if boundary conditions are changed.

- Type II: Micro RS that occur over the grain scale due to the formation of different phases in the structure. They are frequently observed in a polycrystalline material because of the different grain orientation and the anisotropy of a crystal structure.
- Type III: Micro RS present within a grain (over atomic dimensions) and occur because of defects such as dislocations, vacancies or alien atoms distorting the crystal lattice in the crystal structure.

Table 13 – Sources of error in measurement of RS.

Sources of uncertainties and accuracy of calculation of Residual Stresses	Elastic constants Nonlinearity due to texture Stress gradients with depth Microstresses due to plastic deformation or grain interactions
--	---

Reference: (PORTELLA, 2018).

In AM processes - Directed Energy Deposition (DED) and Powder Bed Fusion (PBF) - some in-process strategies can be implemented to minimize RS (see section 3.4): By pre-heating the powder/wire, thermal gradients are minimized (GALLITELLI, 2014). Another alternative is to reduce scan tracks (in the case of laser or electron beam), leading to smaller thermal gradients (YAMAGUCHI, 2017; OYELOLA, 2018), which have a significant, direct or indirect, influence on RS distribution (KUDRYAVTSEV, 2011). Carlsson *et al.* (CARLSSON, 2001); b) proposed a power-law relation (Equation 1) for residual surface stress (uniaxial stress-strain), considering both theoretical and experimental analysis. This equation was tested for Al4120-14 and vessel steel A508B and proved to be in good agreement with experimental results (CARLSSON, 2001).

$$\sigma_{RS} = k \varepsilon^n \quad (1)$$

Typically, in AM processes, during manufacturing, stress can also be described in a nonlinear mechanical analysis, as follows (MEGAHED, 2016):

$$\nabla \cdot \sigma + F_{int}^{\vec{}} = 0 \quad (2)$$

$$\sigma = C \varepsilon \quad (3)$$

$$\varepsilon = \varepsilon_e + \varepsilon_p + \varepsilon_{th} \quad (4)$$

$$\varepsilon_e = \frac{1+\nu}{E} \sigma - \frac{\nu}{E} tr(\sigma) II ; \varepsilon_p = g(\sigma_Y) \quad \varepsilon_{th} = \alpha(\theta - \theta_0) \quad (5)$$

Where C is a tensor of material's stiffness, $g(\sigma_y)$ is a function depending on the material behavior and α is the material thermal dilation coefficient. As noted in equation (2), in solids, the gradient of all stresses is equilibrated by its internal forces. Deformation – equations (4) and (5) - is divided in three components: ε_e , which corresponds to the elastic regime and depends on Poisson ratio and Young modulus, ν and E , respectively; ε_p , plastic deformation, related to material behavior and specific properties under plastic regime; and, finally, a thermal component, ε_{th} , which is dependent on process temperature and material's thermal properties. Still, some more assumptions in the thermal component requires further analysis: radiation-derived phenomena, heat conductivity, thermal gradients formed during manufacturing. Simulation software such as Ansys and Simufact are progressing in the determination of the consequences of fast energy transfer in parts.

Lastly, for each AM process and material, there is a specific distribution of RS. Therefore, two samples from the same material produced by different techniques, e.g., EBM and SLM, will not present similar distribution of RS (KUDRYAVTSEV, 2011). In AM processes, stresses are higher in the perpendicular direction than in the scanning direction. In processes which EDM cutting is required (SLM and EBM), this operation introduces strong tensile stresses in the depth of around 40 μm from the cut surface (GUO, 2009). Post-processing techniques, however, are useful to reduce, redistribute, or even eliminate RS. These methods are described in Table 14 and are further discussed in section 3.4.5.5.

Table 14 – Methods for relieving of Residual stresses.

Mechanisms of reduction /redistribution /elimination of Residual Stresses	Type	Author(s)
	Peening: ultrasonic, laser shock, hammer, shot, heat treatment	(KUDRYAVTSEV, 2011)
	Machining	(GUZ', 2000)
	Explosive treatment	(GUZ', 2000)
	Reference: Own authorship, 2018.	

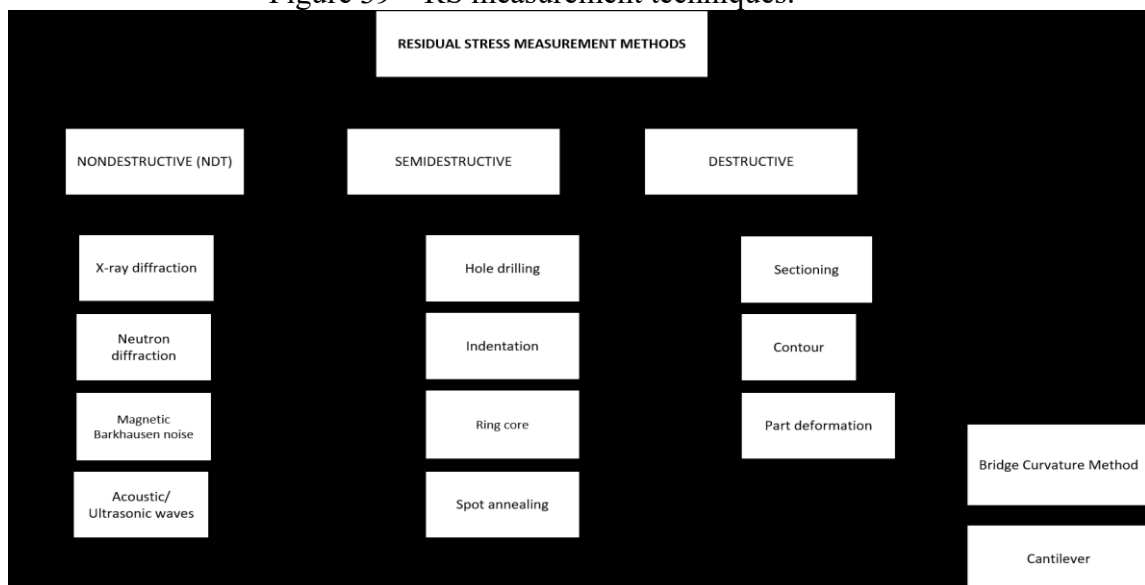
3.4.5.1 RS measurement methods

Fundamentally, RS measurement methods can be divided into three major groups: nondestructive, semi-destructive, and destructive. Some examples of each type are presented in Figure 36. The measurement process introduces a perturbation in the stress state of a sample, which is especially pronounced in destructive and semi-destructive cases. In all

cases, the residual strain is calculated and then, by linear elastic theory for homogeneous isotropic solids, residual stresses are obtained (GREEN, 1978).

In nondestructive methods (NDT), e.g. neutron diffraction and XRD (Figure 39), the crystal lattice strain is measured, and the corresponding residual stresses are estimated using elastic constants, assuming linear elastic deformation of the crystal lattice. NDT techniques can provide information on a series of material properties and characteristics, which are listed in Table 15. Typically, these methods bring great flexibility of use and repeatability, and high precision. Nevertheless, there are some disadvantages, such as limited penetration and reflection of waves/rays. Additionally, sample size can be critical in some cases and operation cost is a major concern, especially regarding neutron diffraction (WU, 2014). Destructive methods, such as sectioning, consist of removing specific portions of a sample to relieve residual stresses. Then, deformations are created, and the corresponding stresses can be determined. Typically, these methods require FEM tools to analyze deformation behavior and, then, obtain residual stress values (WU, 2014). As an intermediary case, semi-destructive methods (Figure 39) induce fewer properties modifications than destructive methods. Among those, hole drilling is the most used one. It consists of cutting a portion (hole) of a part and installing strain gauges to measure stress profiles. In most modern approaches, digital image correlation (DIC) can be coupled to hole drilling and provide more precise information on the stress behavior (BALDI, 2014).

Figure 39 – RS measurement techniques.



Reference: Own authorship, 2018.

As a complementary method to acquire more information on RS, Finite Element Method (FEM) simulations can be used. Different authors (ARCE, 2012; PARRY, 2016; PROTASOV, 2016) compared the results obtained by experiments with a linear elastic model created on a specific FEM software. In the majority of cases, it was considered that most of the properties of the materials are temperature-dependent. Using specific models from ABAQUS and ANSYS 19 software, thermal-induced stresses can be created, and the correlated effect on the part can be modeled.

Table 15 – Field of application for NDT in materials characterization.

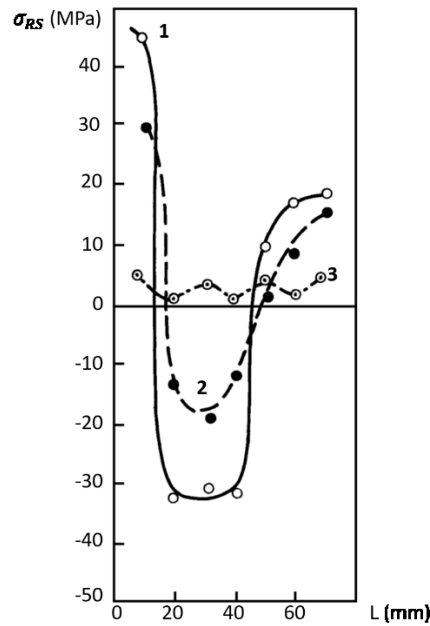
Mechanical properties	Physical properties
Tensile modulus	Microstructure
Shear modulus	Grain size
Tensile strength	Phase composition
Yield strength	Porosity/voids
Fracture toughness	Inclusions
	Anisotropy
Hardness	Hardening depth
	Residual stress
	Thermal history

Reference: Adapted from (VARY, 1978).

3.4.5.2 RS measurement cases

In a study by *Guz et al.* (GUZ', 2000), many parts were analyzed using ultrasonic-based NDT, also named as Ultrasonic Testing (UT), with an emphasis on biaxial RS measurement. A long strip made of Aluminum - 6% Magnesium (AMG6) was evaluated under the influence of different additional machining, aiming for RS relieving (Figure 40). Initially, a measurement of RS is made right after the deposition of a bead along the edge of the strip (curve 1). Then, the part is subjected to a stress of 50 % σ_y - yield stress (curve 2, first machining step) and, finally, a stress of 100% σ_y is applied (curve 3, second machining step). Considering all measured RS curves (Figure 40), it can be stated that progressive machining steps yield a decrease in RS.

Figure 40 – RS measurement of samples by UT.



Reference: Adapted from (GUZ', 2000).

In analogous cases, parts were subjected to heat and explosive treatments and were then measured by ultrasonic NDT. Measurements indicated a significant reduction of RS (both biaxial and triaxial) (GUZ', 2000). As most of the RS data acquisitions occur in finished parts, *Cerniglia et al.* (CERNIGLIA, 2015) performed an analysis of defects during fabrication of LMD (similar to DMLS) components: by combining the FEM approach with laser ultrasonic measurements, defects with size greater than 100 μm and depth up to 700 μm were successfully characterized. This same approach could be applied to study RS, including high precision analysis.

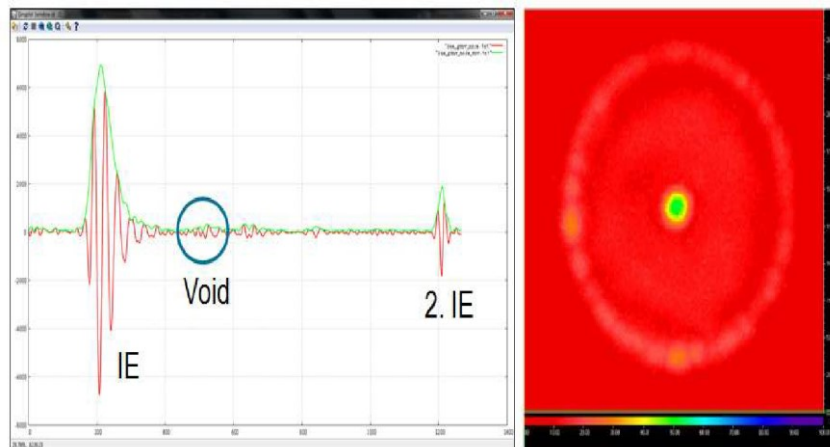
3.4.5.3 RS in-situ measurement/monitoring

Because of its compact setup, reliability and cost-effective characteristics, acoustic wave systems can be coupled to AM processes and monitor the fabrication of parts, layer by layer. A new generation of AM equipment is under development, including characterization methods to detect *in situ* imperfections and RS. Furthermore, by coupling this new equipment to detect imperfections and change AM process parameters, it will be possible to minimize defects, and, enhance fabrication quality in the finished part. Several types of defects, such as voids, impurities, porosities and cracks, can be detected by this

technique with spatial resolution and wave penetration around a few millimeters (ACEVEDO, 2020).

As each built layer is scanned by acoustic waves, acoustic spectra are obtained, and several perturbations reveal the presence of anomalies (Figure 41), and, with the proper setup, Residual Stresses can be detected (RIEDER, 2014). *Cerniglia et al.* (CERNIGLIA, 2013) proposed an in-line UT inspection device for Laser Powder Deposition (LPD, similar to the DMD process) components. The authors coupled an Nd:YAG pulsed laser (source of acoustic waves) and an interferometric unit (laser receiver) to the building chamber of the LPD machine. During fabrication of Inconel parts, several artificially-induced flaws were accurately detected using ultrasonic (Rayleigh) waves up to 30 MHz. The prototype proved to be competitive with X-Ray computed Tomography (XCT), with the additional advantage of inspecting each layer immediately after solidification. Nevertheless, some challenges need to be overcome, such as the enhancement of data exchange speed between LPD manufacturing unit and ultrasonic device. Additionally, surface effect is critical: Excessive surface roughness increases signal noise and does not produce relevant information (LI, 2016).

Figure 41 – Defect detection using ultrasonic signals.

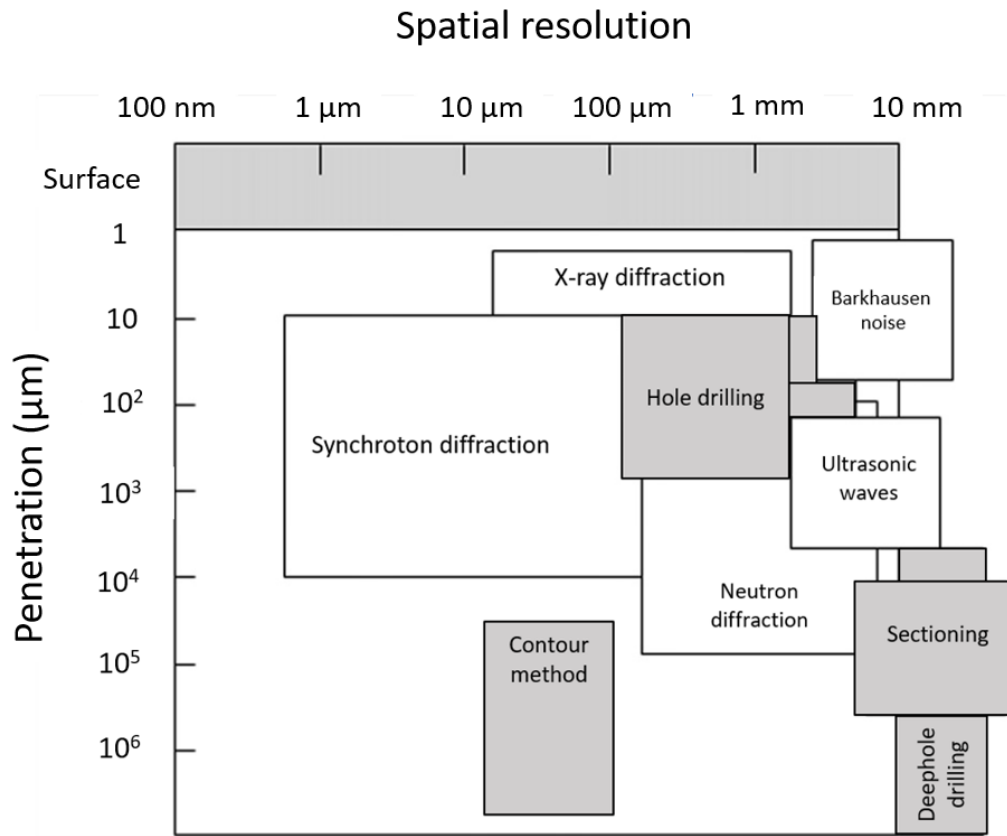


Reference: (RIEDER, 2014).

Despite several positive features of UT, such as the speed of measurement and wide use in large parts, important advances are required in the field of spatial resolution and surface effects: up to date, commercial devices are limited to a few millimeters in spatial resolution whilst XRD and synchrotron diffraction devices are able to reach beyond 100

μm (Figure 42) (ROSSINI, 2012). Moreover, due to surface influence, signal noise is a major drawback of this technique, which increases measurement error (ACEVEDO, 2020).

Figure 42 - spatial resolution and penetration of different measurement techniques.



Reference: Adapted from (ROSSINI, 2012).

3.4.5.4 RS in process control

Several methods, which are summarized in Table 16, can be used to reduce or even eliminate residual stresses: preheating of powder bed, IR cameras, Laser Shock Peening (LSP) and even specific algorithms for scan strategy control.

Among those, thermal control is the most widely applied in RS control. According to *Li et al.* (LI, 2016), preheating the powder at temperatures higher than 570 °C could eliminate RS and create beneficial compressive stresses. On the other hand, when the base plate was heated at 160 °C, a 40% reduction of RS was observed (LI, 2018). In yet another study, by *Buchbinder et al.* (BUCHBINDER, 2014), a preheating temperature of 250 °C was employed in AlSi₁₀Mg cantilevers made by SLM, which resulted in no defects or distortions and, also, due to lower thermal gradients, fewer RS were formed in these parts. Following

that developments, *Ali et al* (ALI, 2017) used several preheating temperatures in the range of 370 – 770 °C and found that in SLM part production, the minimum generation of RS was found using preheating temperature around 570 °C. Complementarily, at higher temperatures, 570 – 770 °C, compressive RS were observed in several samples. Moreover, cooling rates were diminished during fabrication, and, consequently, high yield strength (1176 MPa) parts were obtained.

Table 16 – Strategies of in situ RS reduction.

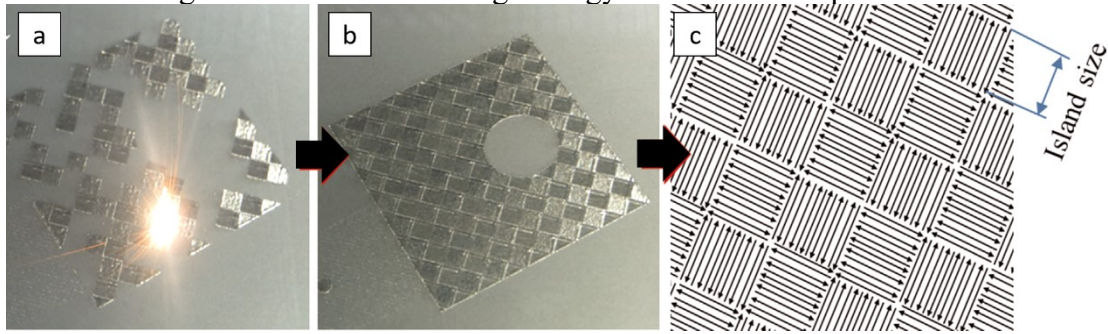
Mechanisms of RS reduction (in situ)	Mechanical control	Laser Shock Peening (LSP) Rolling
	Thermal control	Preheating of powder bed
	Scan strategy control	Algorithms (LaserCUSING®)
	Feedback control	IR cameras

Reference: Adapted from (LI, 2016).

The control of thermal gradients can tailor the formation of RS: some strategies can be applied, including specific algorithms which optimize scan trajectories, significantly reducing thermal stresses, e.g., QM modules (QMatmosphere, QMlaser, QMmeltpool, QMpowder), that are based in Lagrangian cameras, photodiodes and sensors developed by ConceptLaser (SPEARS, 2016). Besides, rescanning each layer promotes a 55% relief on RS (SHIOMI, 2004).

Lu et al. (LU, 2015) used a novel scanning strategy called “island” to create Inconel 718 parts by SLM, and, also to understand how this strategy can affect the microstructure, mechanical properties, and RS. This scanning strategy consists in separating one layer in many small portions —islands, and, then to randomly melt shorter scan tracks through the melt pool (Figures 43 a-c). It was found that parts made by 2x2 mm² islands presented less RS than other strategies, followed by 5x5, 7x7, and 3x3 mm² islands.

Figure 43 – Island scanning strategy for Inconel 718 parts.



Reference: Adapted from (LU, 2015).

Another approach to control and mitigate RS is the use of Laser Shock Peening (LSP), creating compressive stresses to cancel out preexisting tensile stresses. This method can be implemented during AM processing: as each layer is finished, LSP is performed on the present layer, minimizing the effect of thermal stresses (KELLER, 2018). By controlling laser power and focus in LSP, RS field can be modified: higher laser power creates non-equibiaxial RS, while lower laser power generates equi-biaxial RS. Besides, small laser focus implies in higher compressive RS at the surface (KELLER, 2018).

In PBF processing routes, as powder layers are deposited, a stress redistribution is observed. Consequently, the highest tensile stresses are detected in the last deposited layers (KROMM, 2018). In this sense, finer control of layer deposition can effectively reduce RS. In Wire Directed Energy Deposition (W-DED) processing routes, rolling can be implemented to reduce residual stresses. *Martina et al.* (MARTINA, 2016) demonstrated that Ti-6Al-4V samples produced by Wire Arc Additive Manufacturing (WAAM), combined with high pressure rolling of each layer, had lower tensile RS than unrolled specimens. Peaks of tensile stress were found at 200 MPa and 500 MPa, respectively. Also, compressive RS zones were generated in rolled specimens, which were 150-250 MPa higher than in the unrolled samples (MARTINA, 2016).

Lastly, infrared (IR) or near infrared cameras can be installed inside the AM machine to monitor temperature during part manufacturing. By this method, lack or excess of fusion and homogenization of thermal gradients can be determined with high speed and good spatial resolution. Furthermore, when combined with high-speed image analysis, defects can be accurately detected (MOYLAN, 2014; BOONE, 2018).

3.4.5.5 RS post process control

A common solution to reduce RS is the heat treatment after part fabrication, which helps to homogenize and refine microstructure. In AM parts, this post-process step can reduce up to 70% of RS when the treatment is performed in the 600 – 700 °C range (ABA-PEREA, 2016). Annealing also promotes a redistribution of stresses and homogenization of microstructure through solubilization. Besides, with the proper heat treatment several other properties can be tailored, such as tensile strength, ductility, and hardness (ALI, 2017).

Alternative strategies using mechanical treatments are available to diminish RS. Machining (e.g., grinding and hard turning) promotes a redistribution of stresses through the creation of compressive RS on the machined subsurface and surface, resulting in a significant reduction of RS (MATSUMOTO, 1999; GUO, 2009). Parameters such as cutting speed and feed rate have a significant influence on the final residual stress: *Tang et al.* (TANG, 2008) discovered that higher cutting speeds result in shallower RS layers. On the other hand, changes in the feed rate presented less influence in Residual Stresses.

By combining heat treatment and machining, *Oyelola et al.* (OYELOLA, 2018) discovered that a 22% increase in compressive surface RS could be obtained in the case of Ti-6Al-4V produced by DED.

An innovative solution pointed out by *Yamaguchi et al.* (YAMAGUCHI, 2017) uses a magnetic field to finish SLM parts and reduce RS: by controlling the motion of the magnetic tool, RS can be eliminated, mitigating stresses created by the laser during the SLM process.

Another mechanical post-process to control and minimize the effect of residual stresses is the Surface Mechanical Attrition Treatment (SMAT), a technique similar to Laser Shock Peening. However, in SMAT deeper compressive residual stress zones are produced and the impacting balls travel in multiple directions, not only normal to the surface, as observed in LSP (GALLITELLI, 2014; PORTELLA, 2018).

Portella et al. (PORTELLA, 2018) measured RS in 316L stainless steel samples after SMAT and noted that regions of compressive RS were created. These stresses were in the range of -170 to -280 MPa, values that were lower than the tensile residual stresses observed in 316L parts prior to SMAT, which ranged from 90 to 140 MPa (PORTELLA, 2018).

Ultrasonic waves can also be employed to modify the stress profile in samples. In a study by *Gao et al.* (GAO, 2014), structural steel samples were treated by Ultrasonic Impact Treatment (UIT): as a direct consequence, residual stresses were redistributed and softened. This effect was more pronounced in deformed regions (stress concentration zones) and authors stated that ultrasonic waves modified RS in depths up to 16 mm (GAO, 2014).

Hybrid methods that combine production and stress relief process can also be employed, as mentioned by *Kalentic et al.* (KALENTICS, 2017; KALENTICS, 2017). First, LSP was used in the surface of the SLM part, during the fabrication process, which significantly reduced RS by switching tensile to compressive RS in a depth of 1 mm of the part surface (KALENTICS, 2017). Moreover, low energy pulsed lasers with high frequency and small spot size are well suited to optimize compressive RS, both in depth and in magnitude (KALENTICS, 2017).

3.5 PARAMETER INFLUENCE ON PART PROPERTIES

In the previous sections, the main parameters of SLM process were introduced. Each of these parameters plays a specific role and has an influence over the produced part properties. Moreover, when using SLM method with a 200 W Ytterbium fiber laser and a Ti-6Al-4V spherical shape powder (25-45 μm particle size), it is possible to obtain parts almost 100% dense, with mechanical properties such as: tensile strength greater than 1 GPa and 12% elongation at break (HANZL., 2015).

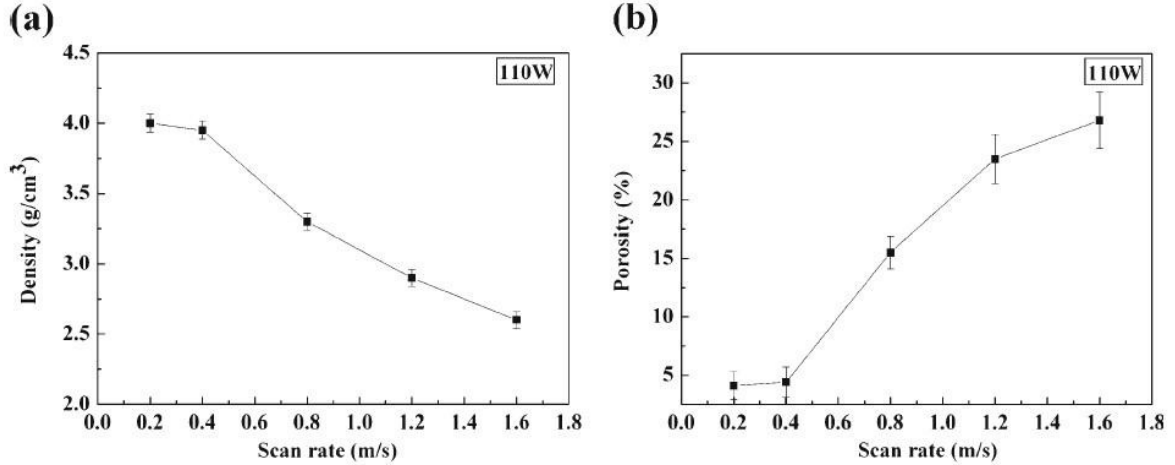
3.5.1 Scanning rate and scanning strategies

In a research by *Song et al* (SONG, 2012), a constant laser power output of 110 W was used to obtain Ti-6Al-4V dense parts using SLM. It was observed that higher scanning speeds (v) produced less molten volume, creating a higher cooling rate, and, in the other hand, revealing a finer microstructure. Also, as scanning speed rises, an abrupt decrease in density is observed (Figure 44(a)), and, consequently, porosity becomes more important (Figure 44(b)).

At lower scanning speeds, densification is higher, more specifically in the 0.2 – 0.8 m/s range (Figure 44(b)). As scan rate increases from 0.4 m/s to 1.2 m/s, density reduces

abruptly, because there is more time available for sintering to occur and organize the structure creating a coarser microstructure at lower scan speeds, typically at 0.2 – 0.4 m/s (SONG,2012).

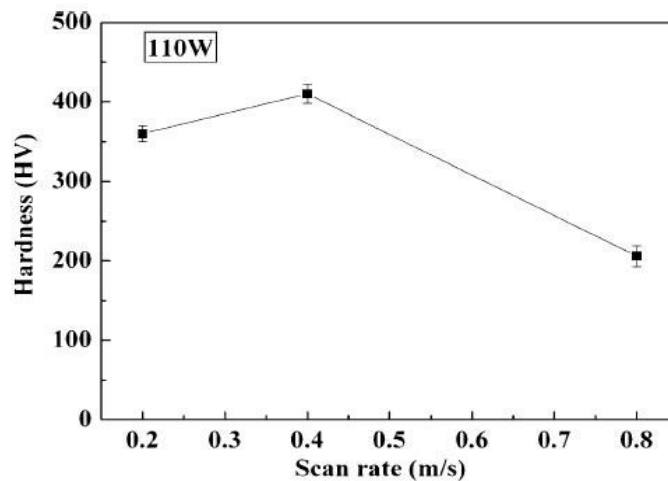
Figure 44 – Density (a) and porosity (b) curves at different scan rate values.



Reference: Adapted from (SONG, 2012).

In another study by *Song et al* (SONG, 2012), authors reported that the scanning rate has a significant influence on hardness values of Ti-6Al-4V samples made by SLM. At lower scanning rates – 0.4 m/s, there are less pores and the measured hardness is around 410 HV (Figure 45). As scan rate overpasses 0.4 m/s, hardness decreases significantly: at a scan rate of 1.2 m/s the measured hardness is around 230 HV (Figure 45).

Figure 45 – Hardness & scan rate behavior of SLM made Ti-6Al-4V parts.

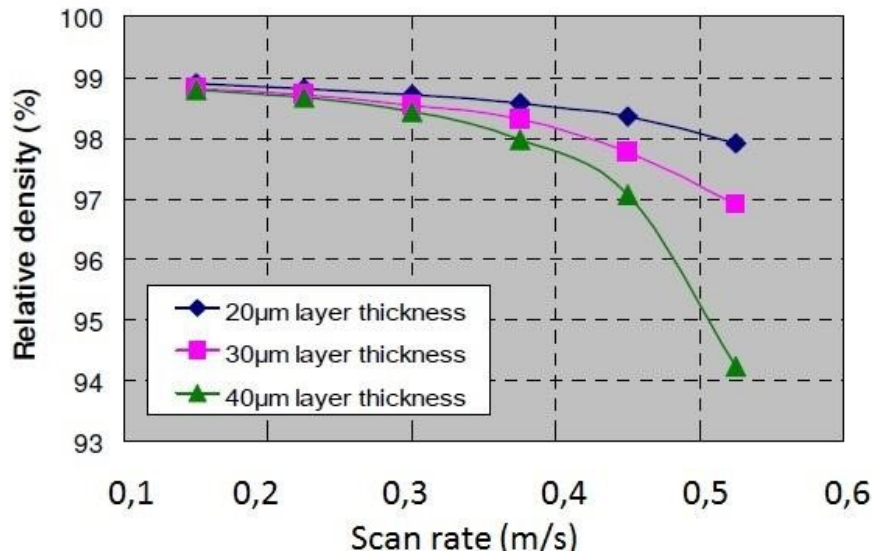


Reference: Adapted from (SONG, 2012).

At lower scan rate the temperature is relatively lower and there is more α phase (hexagonal close packed – hcp) of Titanium, which is stable until 882 °C (Figure 8). Since there is a higher densification in phase α than in phase β (base centered cube - BCC), the resulting micro hardness will be greater at lower scan speed (typically at 0.4 m/s) (MOTT; ROLAND, 2009).

Complementarily, there is a correlation between scan rate and densification for a specific powder thickness: using AISI 316L stainless steel, *Kruth et al* (KRUTH, 2010) produced a series of dense parts to test the influence of scan rate on densification for different values of powder thickness (20, 30 and 40 μm) and constant laser power (105 W). The behavior of densification in function of scan rate is observed in Figure 46: at lower scan rates (0.15 – 0.3 m/s), relative density has little variations (less than 1%) for 20, 30 and 40 μm layer thicknesses. Thus, at lower scan rates, density can be regarded as independent of layer thickness, making possible to achieve significant densification levels for thicker layer of powder. Finally, with the increase of scan rate, density values become more disperse and the greatest layer thickness will present the lowest densification (GU, 2012), which corroborate the findings by *Song et al.* (SONG, 2012).

Figure 46 – Influence of scan rate on densification for different layer thicknesses.

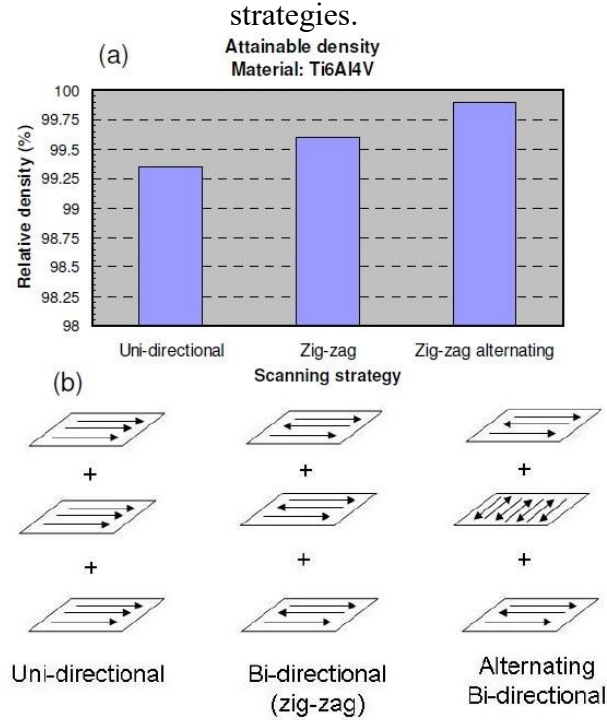


Reference: Adapted from (KRUTH, 2010).

Kruth et al (KRUTH, 2010) examined the influence of scan strategies on the density of Ti-6Al-4V parts. Authors discovered that for three different scan strategies (unidirectional,

zigzag and zig-zag bidirectional), densification suffered very little variation (around 0.5%), which is shown in Figure 47. The main advantage to use zig-zag alternating is a minor risk of producing cracks and more efficient dissipation of thermal gradients (KRUTH, 2010).

Figure 47 – (a) Attainable density according to different scanning strategies; (b) scanning strategies.

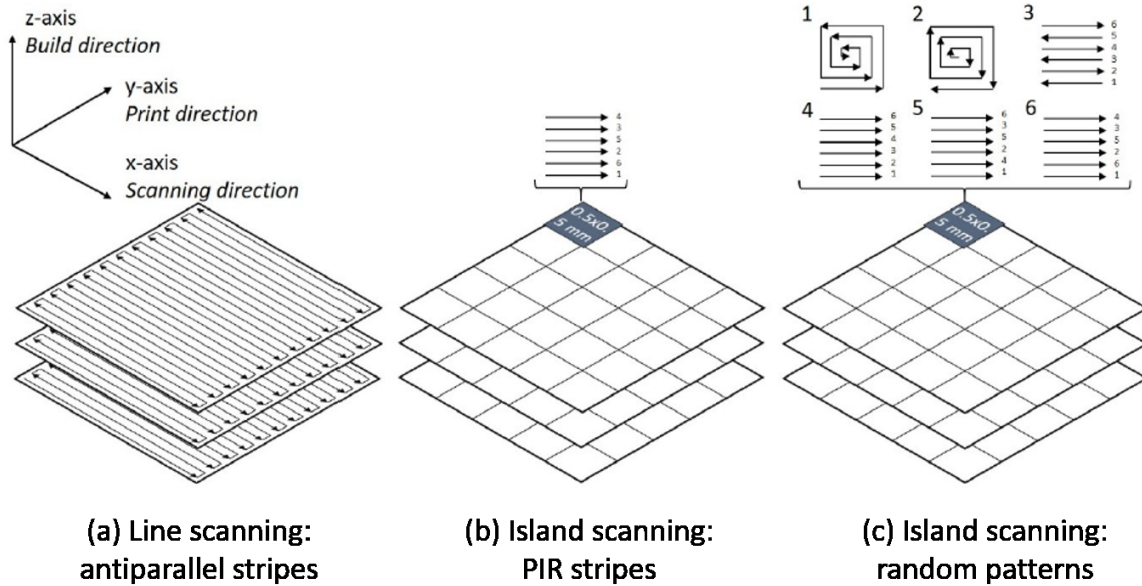


Reference: Adapted from (KRUTH, 2010).

Valente *et al.* (VALENTE, 2019) investigated on the influence of three different scan strategies in as-built Ti-6Al-4V grade 5 SLM samples in hardness, porosity and surface roughness. SLM process parameters were held constant, with laser power of 119 W, layer thickness of 50 μm and scan speed of 800 mm/s.

Scanning strategies were set as follows: Line scan with antiparallel stripes (Figure 48(a)); island scan parallel-interlaced-reversed (PIR) stripes (Figure 48(b)); and, island scan random patterns of six different types: (1) out-in spiral, (2) in-out spiral, (3) antiparallel stripes, (4) parallel stripes, (5) parallel-interlaced stripes, (6) PIR stripes (Figure 48(c)) (VALENTE, 2019).

Figure 48 - scan strategies: (a) lines scanning using antiparallel stripes [LS]; (b) Island scanning using PIR stripes [IS-PIR]; (c) Island scanning using random patterns [IS-RP].



Reference: Adapted from (VALENTE, 2019).

Scan strategies had a notable influence in the microhardness of as-built SLM samples: island scan strategies PIR stripes and random patterns presented the highest hardness values, 492 and 496 HV_{0.01}, respectively, against 474 HV_{0.01} for line scan samples. This difference is explained by the decomposition of α' martensite into lamellar α/β phase observed only in line scan samples (VALENTE, 2019). Nevertheless, all measured hardness data were superior to the values reported in the literature for as-printed DMLS and SLM test pieces, respectively, 440 HV (XU, 2017), 427 HV (THIJS, 2010), 410 HV (SONG, 2012).

Concerning density (ρ), the highest values were observed for Line scanning strategy (ρ [LS]= 99.63%), followed by the island scanning strategy using random patterns (ρ [IS-RP] = 99.23%), and, the lowest density was obtained in island scanning strategy using parallel-interlaced-reversed stripes (ρ [IS-PIR] = 98.63%). Complementarily, pore distribution and form were also investigated: Line scanning samples presented the lowest porosity (0.37%) with predominant spherical pores; samples built with island scanning using random patterns have the second lowest porosity (0.77%) and the majority of pores were found to be spherical; samples produced by island scanning using PIR presented the highest porosity (1.37%) and pore form preponderancy was irregular, which is assumed to be a consequence of Lack of Fusion – LOF (VALENTE, 2019).

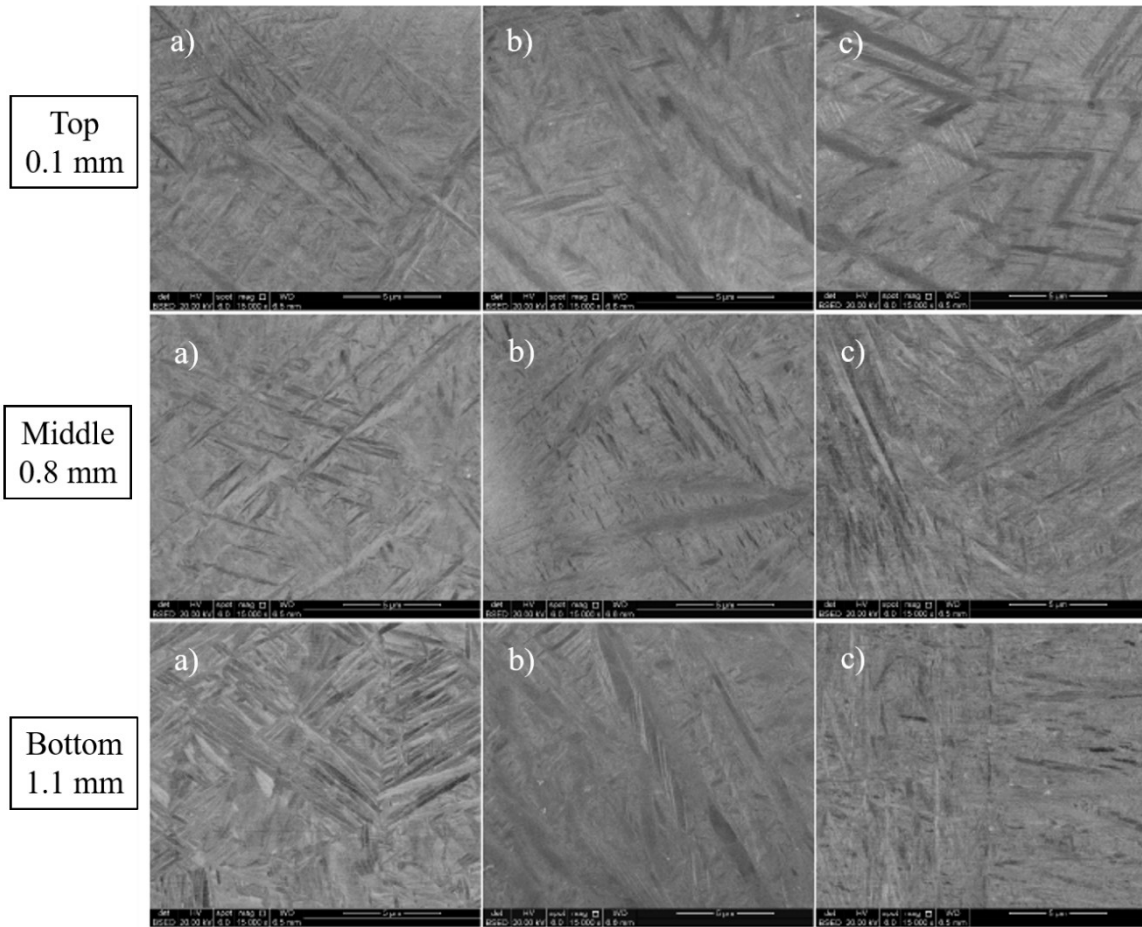
Regarding surface roughness and topography, samples built using line scanning strategy (Figure 47(a)) presented the lowest values of surface roughness (S_a [LS] = 48.4 μm < S_a [IS-PIR] = 66.4 μm < S_a [IS-RP] = 82.8 μm) despite presenting an irregular surface topography. Moreover, island scan strategies distributed deformations more homogeneously through the surface than the line scan strategy (VALENTE, 2019).

3.5.2 Microstructure

Microstructure plays a fundamental role in the properties of a part made by any fabrication method, especially SLM. In a study by *Facchini et al.* (FACCHINI, 2010), the modification in mechanical properties with microstructures of Ti-6Al-4V produced by SLM was observed. The formation of unique hcp α' martensitic microstructure (Figure 11 (a) and (c)) increases the tensile strength (GU, 2012) and hardness of SLM manufactured parts (VALENTE, 2019), making it higher than that of hot worked parts, whereas lower ductility is observed. A postprocessing heat treatment induces the transformation of the metastable martensite into a biphasic α - β matrix, as can be observed in Figure 11 (b) and (d), resulting in a greater ductility and a tensile strength decrease. The stabilization of microstructures contributes to the improvement of the ductility. By using SLM method under different conditions, it was possible to fabricate dense parts through the control of martensite transform in Ti-6Al-4V (FACCHINI, 2010).

SLM scan strategies can also influence microstructure. In this sense, *Valente et al.* (VALENTE, 2019) studied how SLM scan strategies modified microstructure of as-built Ti-6Al-4V samples. Microstructure analysis of samples built using line scan strategy revealed the decomposition of acicular α' martensitic into ultrafine lamellar α/β – bottom Figure 49(a), and, α' in top and middle positions of Figure 49(a). Top, middle and bottom – positions that refer to the distance from the last melted layer – of Figure 49(b) and (c) are predominant acicular α' martensite, demonstrating that for island scan strategies no martensitic decomposition is observed.

Figure 49 - microstructure of as-built samples: (a) scan line; (b) island scan PIR stripes; (c) island scan random patterns.



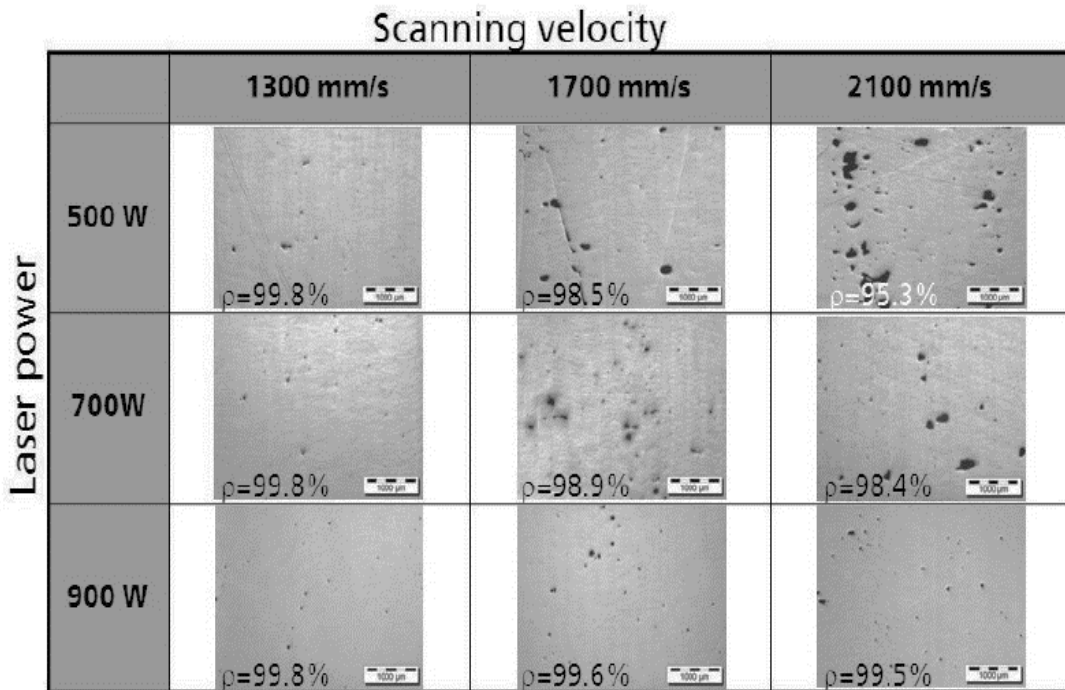
Reference: Adapted from (VALENTE, 2019).

3.5.3 Scanning speed and laser power

In an article by *Buchbinder et al* (BUCHBINDER, 2011), high power SLM was performed to produce aluminum alloy - $\text{AlSi}_{10}\text{Mg}$ - parts. A laser power of 500 W, 700 W and 900 W (Gaussian beam form) was used to sinter dense parts made of $\text{AlSi}_{10}\text{Mg}$. This was possible since this aluminum alloy presents a high thermal conductivity similar to copper, silver and gold. As laser power and scan speed increased, the highest densification of the sintered part was observed: 99,8% (laser power of 900 W and 1300 mm/s of scanning speed) with refined microstructure and few defects. Optimal density results were also observed for scan speed of 1300 mm/s and 500 W; scan speed of 1300 mm/s and 700 W. For 900 W of laser power and scan velocity higher than 1300 mm/s, densification is significant but more defects are reported (Figure 50).

At 2100 mm/s (2.1 m/s) and laser power ≤ 700 W, density is low and defects concentration is high (Figure 50), which can be explained by a low energy density that causes LOF. As laser power increases, less imperfections were verified for different scan speeds (1300, 1700 and 2100 mm/s), because there is enough energy to sinter and locally melt powder material. Densities high as 99.8% were observed for different samples (BUCHBINDER, 2011).

Figure 50 – Density dependency on scanning velocity and laser power for AlSi₁₀Mg samples.



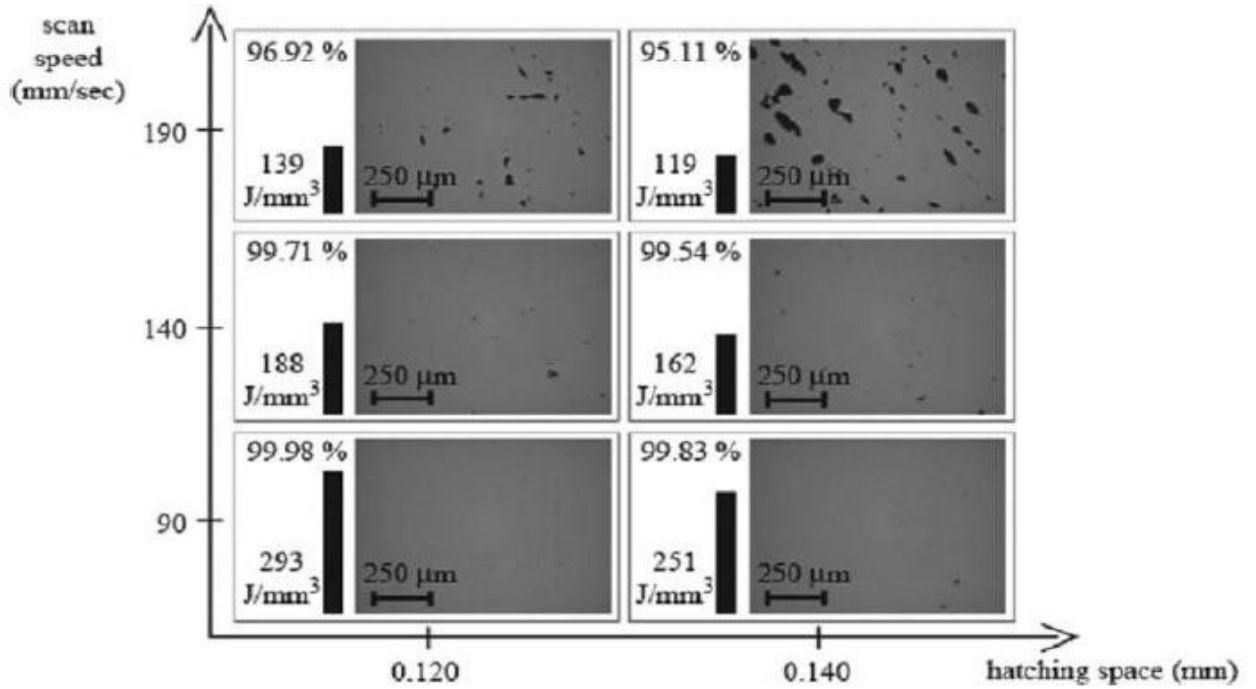
Reference: Adapted from (BUCHBINDER, 2011).

In a study by *Vandenbroucke et al.* (VANDENBROUCKE, 2007), densification behavior of Ti-6Al-4V parts were observed in function of V and laser power. The optimum set of parameters makes possible to obtain the highest densification. Figure 51 illustrates the evolution of microstructure with scanning speed and laser power.

As scanning speed increases, it is observed for different laser power values that density decreases for hatching spaces of 0.12 mm and 0.14 mm. On the other hand, when laser power increases and scanning speed decreases, the highest densities are obtained: 99.98% for a laser power of 293 J/mm³ and a hatching space of 0.12 mm; 99.83% for a laser power of 251 J/mm³ and a hatching space of 0.14 mm. The hatching space or hatch spacing

is the distance between two neighboring vectors, hatch lines (Figure 29(b)). Hatch spacing is usually less than the beam diameter (DAHOTRE; HARIMKAR, 2008).

Figure 51 – Density behavior of Ti-6Al-4V parts processed by SLM with laser power and scanning speed.



Reference: Adapted from (VANDENBROUCKE, 2007).

In order to link parameters laser power (P), scan speed (V), hatch spacing (h), layer thickness (d), an equation has been proposed by *Gu et al.* (GU, 2012). The term “VED”, which stands for “Volumetric Laser Energy Density”, has been introduced with the aim to understand and increase the controllability of AM processes, especially those that use laser as energy source for sintering/melting (GU, 2012).

$$VED = \frac{P}{vhd} \quad (6)$$

Equation (6) is also very useful to verify how the parameters P,v,h and d influence the densification of powder.

In a study by *Gu et al.* (GU, 2006), processing Laser Sintering parameters were optimized to increase production of high – density (HD) parts composed of Cu-CuSn-CuP powder: for a VED ranged between 0.16 – 0.23 kJ/mm³, there is a higher yield of HD parts.

3.6 SLM PERSPECTIVES AND ENHANCEMENTS

In a simplified manner, SLM process can be enhanced by changing few parameters. Among these, scan strategies, laser specifications and powder preheating figure as the most remarkable (HAGEDORN et al., 2011):

- Adoption of scan strategies and laser parameters that imply in a less aggressive heating regime, and, therefore reduce the overheating responsible for spatter and balling generation, as well as excessive grain growth and coarsening.
- Scan strategies applying powder pre-sintering through low energy density laser and layer re-melting to reduce spatter formation.
- Modulation of the laser pulse form (Gaussian, non-Gaussian, multiple pulses). Distributing laser power energy density over a longer period of time softens thermal gradients and creates less RS.
- Pre-heating of the powder: aims to reduce thermal gradients which are intensified during sintering process. In the other hand, the control of cooldown is also desirable to prevent crack propagation and thermal shock.

In order to increase SLM productivity (a typical building speed is around 5 mm³/s (BUCHBINDER, 2011), higher laser power (> 1 kW) and higher scan speed (> 3000 mm/s) are limitations to surpass. In this regard, the simultaneous use of multiple lasers can significantly optimize SLM efficiency, for instance, a three-laser system in which one laser is used to preheat the powder (reducing thermal gradients and RS), and two others employed in the sintering process. Nevertheless, this adds up complexity to the system, which is challenging to machine software and control development.

In situ process monitoring of SLM (defect formation, crack propagation, undesired porosity and balling/spatter) using techniques such as XRD, Ultrasound (UT) and Infrared (IR) is expected to be integrated in a new generation of machines. This new feature will increase overall productivity, as well as greater quality control and optimization of fabrication costs. As defects are detected, in the majority of cases, process parameters have to be swiftly corrected and this implies in a significant computation effort. In this sense, several Multi Criteria Decision Making (MCDM) routines can be applied such as Promethee method: first proposed by *Brans et al* (BRANS, 1986) – has greater application due to its

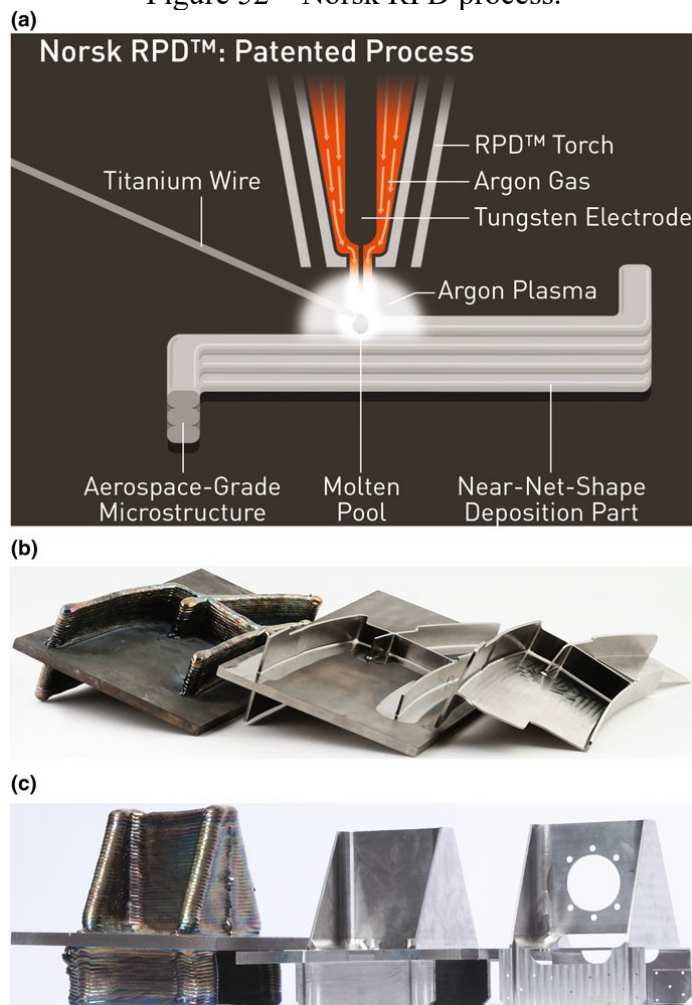
simplicity of calculation when compared to other MCDM methods (ZHU, 2010; GERVASIO, 2012; MAITY, 2015).

Promethee routine is based on extensions of the notion of criterion. Several parameters can be analyzed at the same time and by a ranking routine, this method provides a set of possible actions (BRANS, 1986). Nevertheless, this method can be tendentious in some cases, in a manner such as the answer was previously known, implying in less confidence on the results using this MCDM routine.

Other MCDM methods are Vise Kriterijumska Optimizacija Kompromisno Resenje (VIKOR); Analytic Hierarchy Process (AHP); ELimination and Choice Translating REality (ELECTRE); Technique for Order Preference by Similarity to Ideal Solution (TOPSIS); Grey Relation Analysis (GRA); Preference Ranking Organization Method for Enrichment Evaluations (PROMETHEE); Preference Selection Index (PSI) (AHERWAR, 2019).

Another approach to sinter and melt powder besides laser and electron beam is the use of plasma. Recently, Norwegian company Norsk Titanium patented a new process, Rapid Plasma Deposition (RPD), in which an Argon plasma is locally created by RPD torch and this is used to melt a Ti alloy wire in a molten pool (Figure 52(a)), creating 3D printed objects (Figure 52(b) and (c)), layer by layer as in SLM/EBM/DMLS. According to this company, this new process will allow to save 25 – 75% titanium powder during part production and large parts up to 45 kg can be produced (NORSK, 2020). Moreover, this company has produced the first certified (FAA) AM structural part for Boeing 787 Dreamliner, which is a benchmark for new manufacturing technologies (MILEWSKI, 2017).

Figure 52 – Norsk RPD process.



Reference: (MILEWSKI, 2017).

The use of Titanium alloys in form of wire avoids a series of inconvenient features present in powder, such as high reactivity of pure Ti and its alloys; limitations in recycling; high purity; narrow size distribution and specific morphology (spherical, in most cases); higher cost of fabrication; and, low productivity (MILEWSKI, 2017).

Moreover, compared to SLM, RPD technology allows faster production of parts: one of the claims of Norsk Titanium is that a Merke IV single system could deposit up to 20 tons of parts within a year, with rapid changing of parameters and lot sizes, according to field requirements (NORSK, 2020). Thus, this innovative technique has a great potential and could be employed to fabricate a new generation of auxetic samples (MILEWSKI, 2017).

Furthermore, new materials for SLM are in development considering necessary advances in the relative volatility of the alloying elements, which is a common problem in metal AM fabrication. In this sense, Ti-13Nb-13Zr (Ti alloyed with 13% Nb and 13% Zr,

also named Ti1313) presents several remarkable properties. This predominantly β -phase Ti alloy is more ductile (depending on heat treatment) and presents higher fatigue resistance than its counterpart Ti-6Al-4V (FLORENCIO, 2010). Table 17 presents both properties of Ti-13Nb-13Zr and Ti-6Al-4V (NIEMEYER, 2009). Nevertheless, as Ti1313 is not yet available for SLM processing, specific fabrication parameters and powder features have to be thoroughly developed to ensure parts with repeatable and adequate properties.

Table 17 – Properties of Ti-13Nb-13Zr and Ti-6Al-4V.

Properties	Ti-13Zr-13Nb	Ti-6Al-4V (annealed)
Density (g/cm ³)	4.66	4.43
Ultimate tensile strength (MPa)	1030	895-930
Yield tensile strength (MPa)	900	825-869
Modulus of elasticity (GPa)	64	110-114
Elongation at break (%)	20	6-10
Poisson's ratio	0.30	0.34
Hardness (Hv)	245	349

Reference: (NIEMEYER, 2009).

3.7 SIMULATION USING FINITE ELEMENT METHOD

In order to understand some aspects of the behavior of auxetic materials, a directed study through Finite Element Method (FEM) is a fundamental and effective step.

Elasticity theory which is part of continuum media mechanics, has as primary objective the development of mathematical models that are capable of making a realistic representation of the physical scenery observed in industrial components subjected to mechanical efforts. In the field of structural analysis, the objective can be the determination of internal deformations, in the field of displacement or tensions present in the component due to load application, among others.

Nevertheless, the application of such theories in real cases present difficulties sometimes impassable. For example, in structural analysis, the perfect mathematical representation of loading, geometry, boundary conditions, material behavior, etc. In most of the situations there is complexity, which brings the need to introduce simplifying assumptions to the real problem, in order to allow a mathematical modelling that lead to straightforward solutions.

In the other hand, engineers have shown growing interest for more precise studies for the analysis of structures. This interest comes united to the increasing need to study the

behavior of complex structural elements, which leads to more refined analytic treatment, based in general theories, composed of extremely difficult solutions (CAMARGO, 2012).

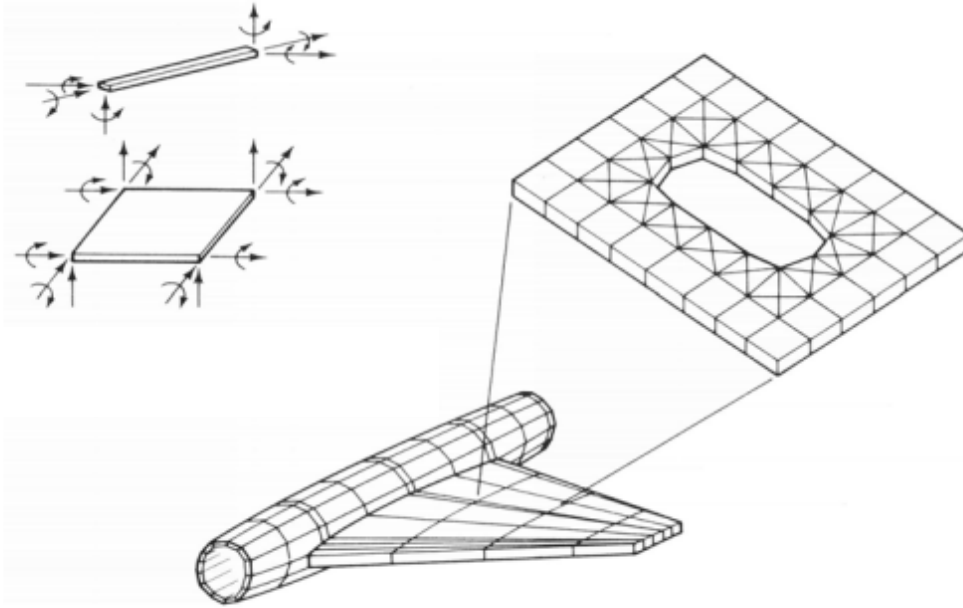
Because of these difficulties, engineers have been searching for solutions to the development and modes of use of approximated methods that allow the execution of the principle of theories such as elasticity theory in an easy and exact manner. The most used methods are those based in the segmentation of continuous medium in simplified parts which presents equations closer to the linearity.

Finite Element Method (FEM) is certainly the most used process for discretization of continuous media. Its large use is also due to the fact that it can be applied, besides the classical problems of the linear elastic structural mechanics, for which the method was developed, but also for problems such as (CAMARGO, 2012):

- nonlinear problems, either static or dynamic;
- solid mechanics;
- fluid mechanics;
- electromagnetism;
- heat transfer;
- filtration using porous media;
- electric field;
- acoustics;

Besides, it is possible to use FEM as a direct comparison between the real physical system and the simulated model (finite elements mesh). As example of practical application of finite elements, Figures 53 and 54 show the wing structure of a commercial plane modeled using bars, peels, triangles and square elements: on each geometrical portion, different types of load, shear and torque are applied. Such models are useful for evaluation and static analysis, free vibration, impact and optimization aimed to lower weight and maximize resistance.

Figure 53 – Schematics of calculation mesh using bar elements.

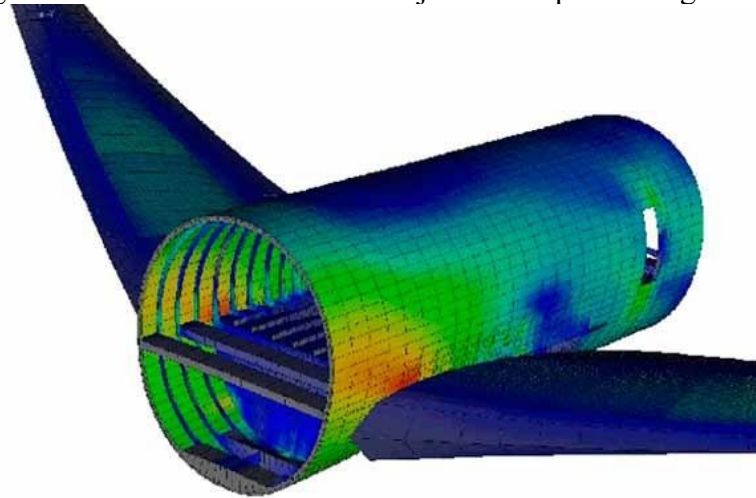


Reference: (CAMARGO, 2012).

Every FEM engages many mathematic theories. In the scope of the work, analytic geometry and linear algebra contain important demonstrations, as well as in the vector theory in many points of the structure. Since the analysis describes the behavior in simplified systems, and then create the whole system, the mathematical model uses matrices for the systems union and linear algebra for complete resolution of problems with many unknown variables (CAMARGO, 2012).

A wing can be submitted to elasticity and stress. Each situation creates a different algorithm in all the length of the plane's wing. It is of great value that in practical applications of this wing, the maximal resistance and applied forces characteristics be known, especially in the borders or in the nodes (welding points or fixation) for a simulation closer to reality. The development of the problem normally occurs in simplified practical situations in order to illustrate modelling, showing the behavior of a conventional wing plane design under different proposed variables, as it is shown in Figure 54 (CAMARGO, 2012).

Figure 54 – Stress concentration in joints of a plane wing.



Reference: (CAMARGO, 2012).

4 MATERIALS AND METHODS

Materials and methods to achieve this research are described in the following steps:

A. Bibliographic investigation in the present State of the art in Selective Laser Melting (SLM), Ti-6Al-4V, Stainless steel and auxetic structures and materials: context and actual research in the field: through intense reading and analysis, important aspects such as SLM process parameters, mechanical properties of Ti and steel alloys, and auxetic materials features will be discussed. Complementarily, Finite Element Methods are also reviewed.

B. Simulation and modeling of auxetic structures: based on the literature survey realized in step A, several auxetic geometries are tested regarding their performance, using mechanical simulation software COMSOL and ANSYS 19. These FEM software perform Finite Element Analysis, allowing to simulate computer models of structures, prototypes and machine components for properties estimation or real service applications. Several modules can be used, from mechanical to thermal, passing through fluid dynamics, optical, electromagnetic, and, more recently, 3D printing simulation.

As this is the last level prior to production of samples (step C), a large number of auxetic structures have to be thoroughly tested and tuned to absorb a maximum

of energy as part of an innovative ballistic armor system. As FEM simulation is the field of expertise of UFSC research partner Thermomechanics Institute of the Czech Academy of Sciences (IT-CAS), a significant joint effort between institutions has been made to ensure the success of this research: in this sense, many important investigations occurred in the IT-CAS laboratories located in Prague.

C. Production of Ti-6Al-4V and 316L stainless-steel parts using SLM: following the research and optimization of auxetic structures in step B, prototypes are fabricated using CL20ES (ConceptLaser) and Ti64 (Tekna) metallic powders described in tables 18 and 19, respectively.

Table 18 – CL20ES SS powder features.

Element	%	Element	%	
Fe	62.89 – 71.5	Mn	0 – 2.0	
Cr	16.5 – 18.5	Si	0 – 1.0	
Ni	10.0 – 13.0	P	0 – 0.045	
Mo	2.0 – 2.5	C	0 – 0.030	
		S	0 – 0.030	
Powder mechanical properties	E (GPa)	Yield strength 0.2 % offset (MPa)	Ultimate Tensile Strength (MPa)	Density (g/cm³)
CL20ES (austenitic SS)	200	470	570	8.10

Reference:(LASER, 2018).

Table 19 – Ti-6Al-4V powder datasheet (Ti64).

Element	Amount (%)	Density	g/cm³
Titanium	Balance	Tap	> 2.7
Aluminum	6.0 – 6.5	Apparent	> 2.3
Vanadium	3,5 – 4.5		
Iron	< 0.250	Average Particle size (µm)	30
Oxygen	< 0.100		
Nitrogen	< 0.030		
Hydrogen	< 0.012		
Carbon	< 0.080		
Yttrium	< 0.005		

Reference: (TEKNA, 2018).

According to machine availability and project budget, several samples were built in two different SLM equipment from SENAI ISI LASER: M2 Cusing (Figure 55(a)) from ConceptLaser – this machine has a larger fabrication chamber (250x250x280 mm) and was used to obtain SS316L samples - and SLM 125HL (Figure 55(b)) from SLM Solutions, which is fully dedicated for the fabrication of Ti and it possess a more compact fabrication chamber (125x125x125 mm), which implies in a lower consumption of inert gas (Argon or Helium), optimizing fabrication costs.

Figure 55 – SLM apparatus: (a) M2 Cusing and (b) SLM 125HL.

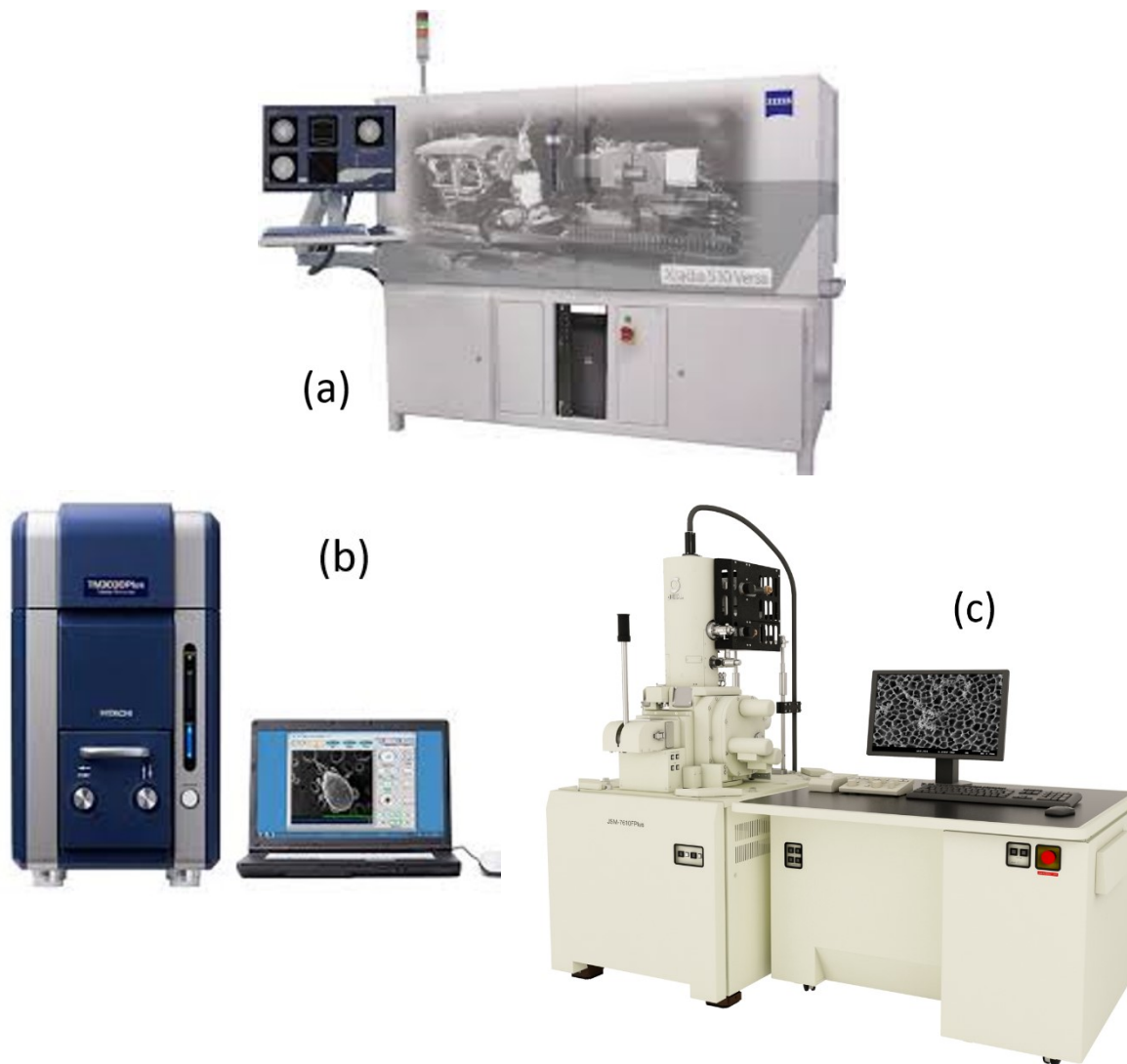


Reference: own authorship and (GE, 2020)

These new parts require different process parameters to optimize fabrication and their mechanical properties, which were developed in partnership with SENAI ISI LASER. To reduce, redistribute or even eliminate the effects of Residual Stresses in the samples, a heat treatment process under inert Argon vacuum (pressure around $1.31\text{E-}7$ atm or 10^{-5} Torr) is a practical and effective solution, as reported in the literature (ABA-PEREA, 2016; ALI, 2017). Further details are presented in section 5. This work was performed by Bodycote company (Liberec, Czech Republic), which is a major player in thermal processing in Europe.

D. Characterization of samples (X-Ray Diffraction; mechanical tests; micro computerized tomography (XCT) and electronic microscopy (Scanning Electron Microscopy – SEM): several analyses were realized to explore microstructure, phases, porosity and mechanical properties of fabricated parts in item C. XCT analysis of samples were held at UFSC, in the Laboratory of Porous Media and Thermophysical Properties (LMPT) using XRADIA 510 VERSA (ZEISS) microtomography unit (Figure 56(a)). SEM analysis occurred at Ceramic & Composite Materials Research Laboratories (CERMAT – UFSC), operating bench microscope HITACHI TM3030 (Figure 56(b)), and, UDESC (Center for Technologic Sciences – CCT, located in Joinville) using JEOL JSM-6701F SEM equipment (Figure 56(c)).

Figure 56 – XCT & SEM microscopes: (a) ZEISS XRADIA 510 VERSA; (b) HITACHI TM3030, and, (c) JEOL JSM-6701F.

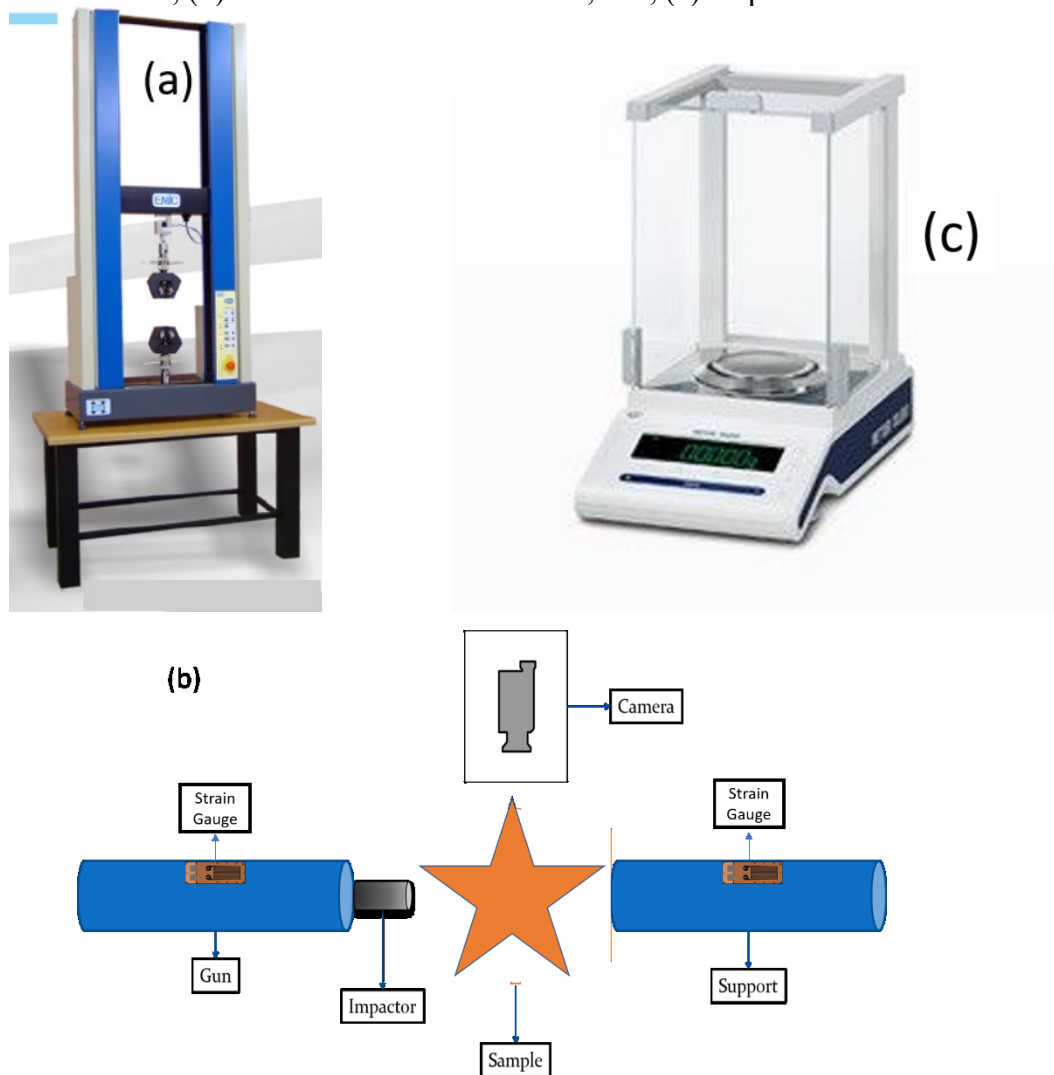


Reference: adapted from (HITACHI BR, 2020; JEOL USA, 2020)

On the other hand, mechanical characterization such as static compression using a bench Universal Testing Machine (UTM) EMIC model DL 3000 (Figure 57(a)) and dynamic tests (Split Hopkinson bar – Figure 57(b)) took place at the facilities of IT-CAS. Compression tests consist in loading a force - using a UTM and a control unit to regulate loading speed (mm/min) and force range (N or kN) - into the sample, which is placed in between two plates. Besides, Split Hopkinson bar test consists in the dynamic impact of a sample by a striker. This experiment allows the determination of dynamic properties and behavior of the sample.

Complementarily, porosity and density of auxetic samples are performed by the Archimedes method: at first, sample weight is measured in air by a Mettler-Toledo New Classic MS balance (Figure 57(c)), and then, weight in liquid (water) is obtained. After that, sample density is calculated from the values measured previously. All characterization processes are described in the Results section.

Figure 57 – Mechanical characterization and density measurement: (a) EMIC DL 3000 UTM; (b) Mettler Toledo MS balance; and, (c) Hopkinson bar test.



Reference: adapted from (EMIC, 2012; Mettler Toledo, 2018; Own authorship, 2018).

E. Model optimization: based on items B, C and D, the geometric models and SLM parameters will be optimized using ANSYS 19, in order to obtain parameters that provide the mechanical properties specified in our application of auxetic armor (high energy impact absorption).

F. Further applications: besides the ballistic field, innovations are planned to take place also in the biomedical area. As the auxetic structures are highly cellular, it is likely to use this feature and create, for instance, bone regeneration guides with increased flexibility composed of Ti-13Zr-13Nb, a Ti alloy with increased ductility.

G. Perform analysis of the data collected, identifying the effectiveness of the proposed methodology applied. Several aspects of the samples were considered: density, mechanical strength, Poisson ratio and yield strength. These results were compared to present literature findings.

To deal with unexpected difficulties¹ during the period of experiments, a different research strategy was employed. It is important to highlight that for each task (mechanical tests a computational experiment was used. This research strategy produced the necessary information to test the hypothesis and achieve the results described below.

A well-known protocol in Science that uses computer simulations, to obtain preliminary results, proved to be an important strategy for the acquisition of information that allowed to test the hypothesis and, then, achieve the general objective of this research.

¹Problems occurred with the IT-CAS Plzen laboratory collaborators, where mechanical experiments using a Universal Testing machine were planned. The main objective of these tests was to measure Poisson ratio in quasi-static regime.

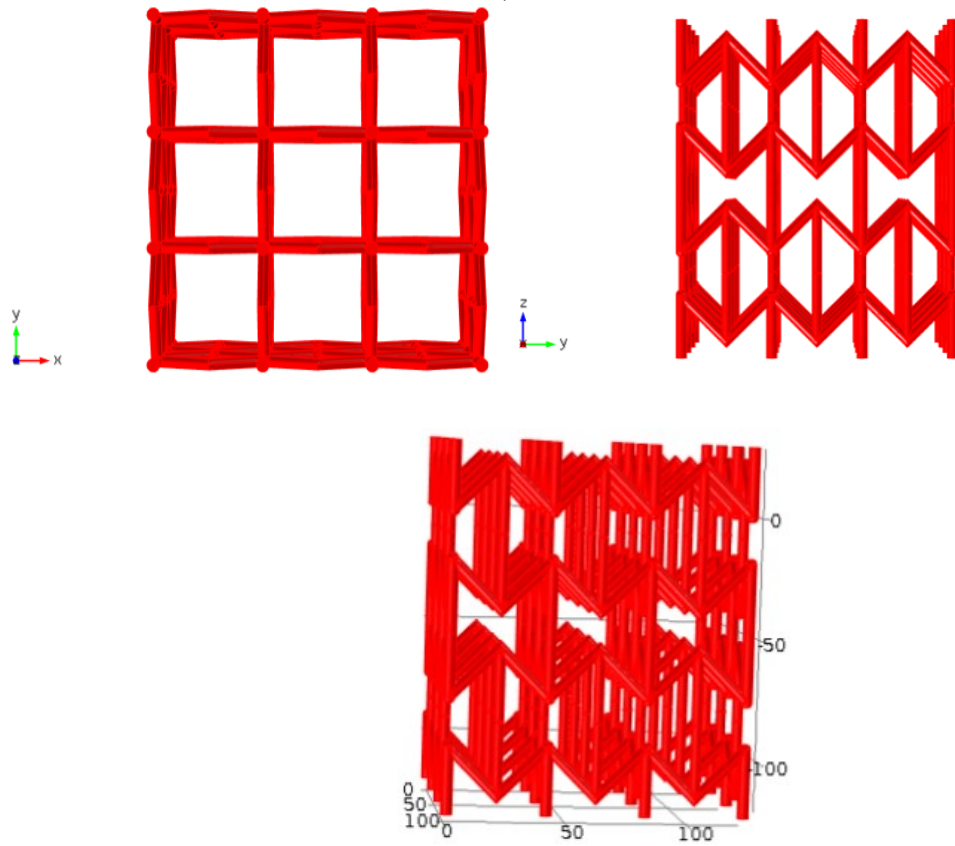
5 RESULTS AND DISCUSSION

In this section, research results obtained through numerical simulation and experiments are presented and the discussion is established.

5.1 SIMULATION OF AUXETIC STRUCTURES

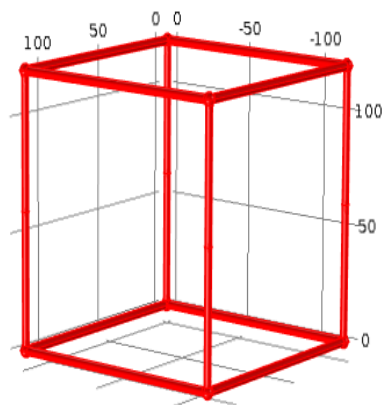
COMSOL and ANSYS 19 FEM software were used to perform calculations and mechanical simulation. Through physical modules of solid mechanics inserted in COMSOL software, it is possible to simulate the behavior of cellular samples composed of Ti-6Al-4V – one of our materials of study. In a preliminary field analysis, three geometries were compared: re-entrant geometry A - expected to be auxetic, as reported in research articles (CARNEIRO, 2013; BOAKYE, 2019), presented in Figure 58; conventional geometries B and C (cubes with or without inner structures). These geometries are shown in figures 59 and 60.

Figure 58 – Cellular structure, geometry A – STR1, 120 mm of edge, (a) view of yx plan, (b) view of zy plan, and, (c) transverse view.



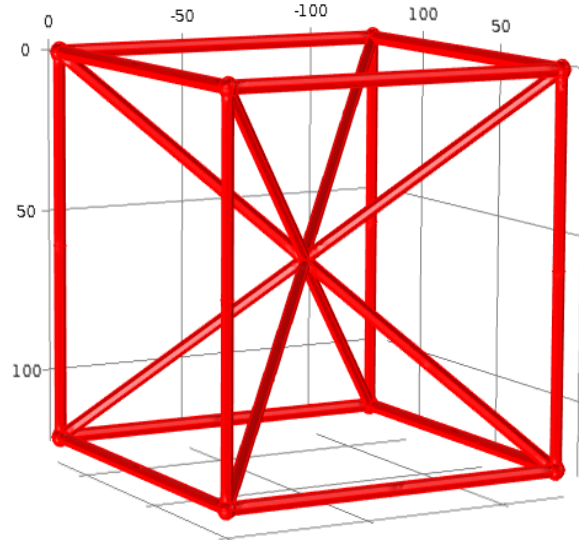
Reference: Own authorship (2018).

Figure 59 – Simplified cube without internal diagonals, geometry B, 120 mm of edge.



Reference: Own authorship (2018).

Figure 60 – Cube with internal diagonals, geometry C, 120 mm of edge.



Reference: Own authorship (2018).

The simulation using COMSOL was based in a uniaxial compression test, applying a pre-set deformation of 4 mm approximately for all three geometries. The body deformation was simulated and analyzed with small variations in deformation, 10% of final deformation per step, as shown in Tables 20, 21 and 22.

Each geometry required different loads to achieve the same percentage of transverse deformation: 24.5 kN; 3.9 kN and 6.5 kN for the geometries A, B and C respectively. Still, those values are in the elastic regime of Ti-6Al-4V.

Table 20 – Deformation of geometry A in Z & Y axis.

Deformation in Z (mm)	Deformation in Y (mm)
-0.50	-0.52
-1.00	-1,06
-1.50	-1.63
-2.00	-2.24
-2.50	-2.87
-3.00	-3.53
-3.50	-4.21
-4.00	-4.88

Reference: Own authorship (2018).

Table 21 – Deformation of geometry B in X & Y axis.

Deformation in X	Deformation in Y
(mm)	(mm)
-0.40	0.13
-0.80	0.33
-1.20	0.65
-1.60	1.23
-2.00	2.15
-2.40	3.18
-2.80	4.12
-3.20	4.94
-3.60	5.67
-4.00	6.34

Reference: Own authorship (2018).

Table 22 – Deformation of geometry C in X & Y axis.

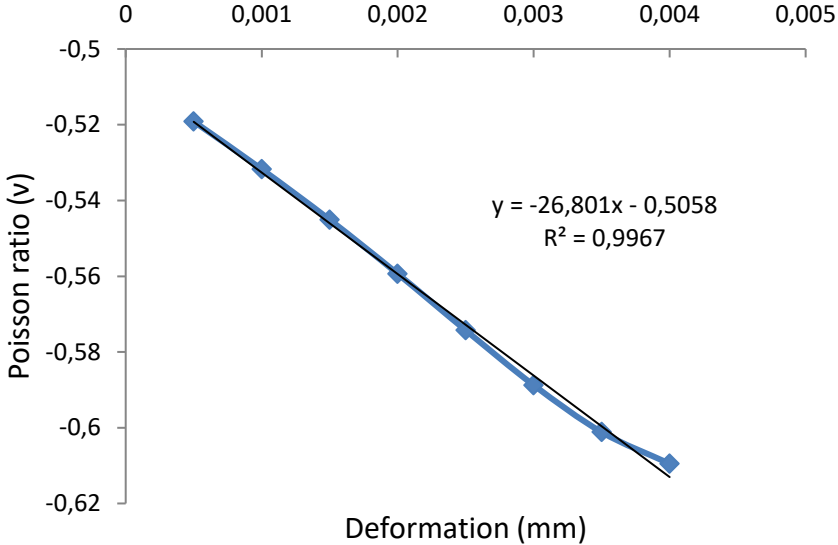
Deformation in X	Deformation in Y
(mm)	(mm)
-0.40	0.19
-0.80	0.43
-1.20	0.77
-1.60	1.29
-2.00	2.05
-2.40	2.99
-2.80	3.94
-3.20	4.83
-3.60	5.65
-4.00	6.39

Reference: Own authorship (2018).

In this case, Poisson's ratio is not only linked to material's properties, but also with the geometry, presenting thus distinct values for each geometry. Poisson's coefficient, ν , measures transverse deformation (according to the longitudinal direction of load application) of a homogeneous and isotropic material. Poisson's ratio is calculated by a relation between orthogonal deformations, as it has been shown in section 3.2 (page 33).

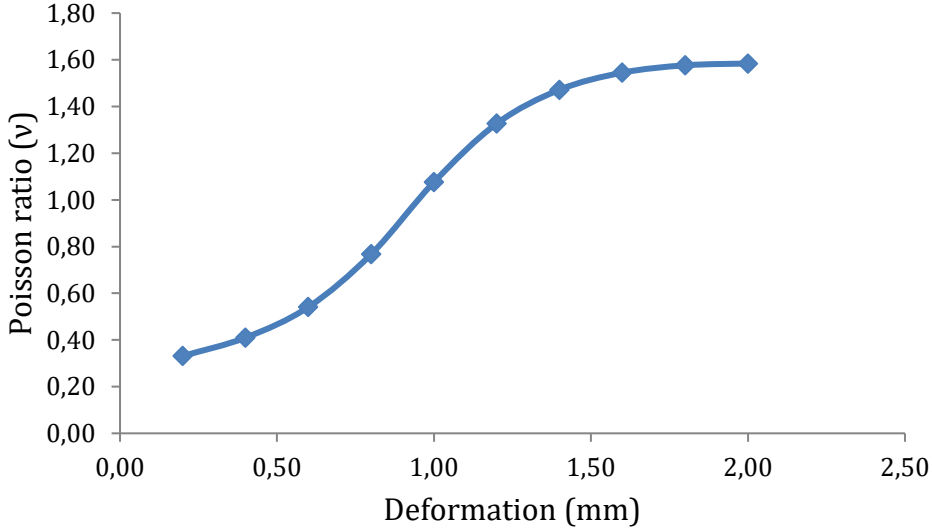
Using data contained in Tables 20 - 22, it was possible to obtain values of Poisson's ratio for each studied deformation, in function of the deformation. In Figures 61 to 63 the behavior of Poisson's coefficient is observed for all geometries.

Figure 61 – Poisson’s coefficient in function of compressive deformation in geometry A.



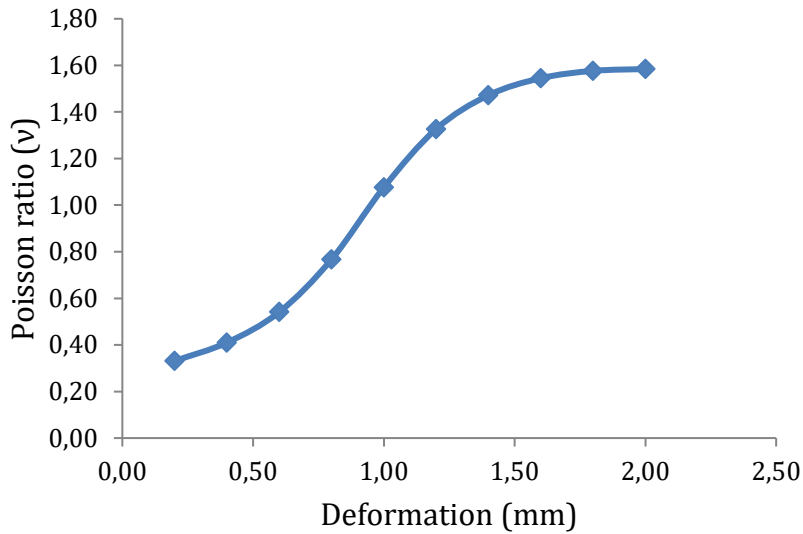
Reference: Own authorship (2018).

Figure 62 – Poisson’s coefficient in function of compressive deformation in geometry B.



Reference: Own authorship (2018).

Figure 63 – Poisson’s coefficient in function of compressive deformation in geometry C.



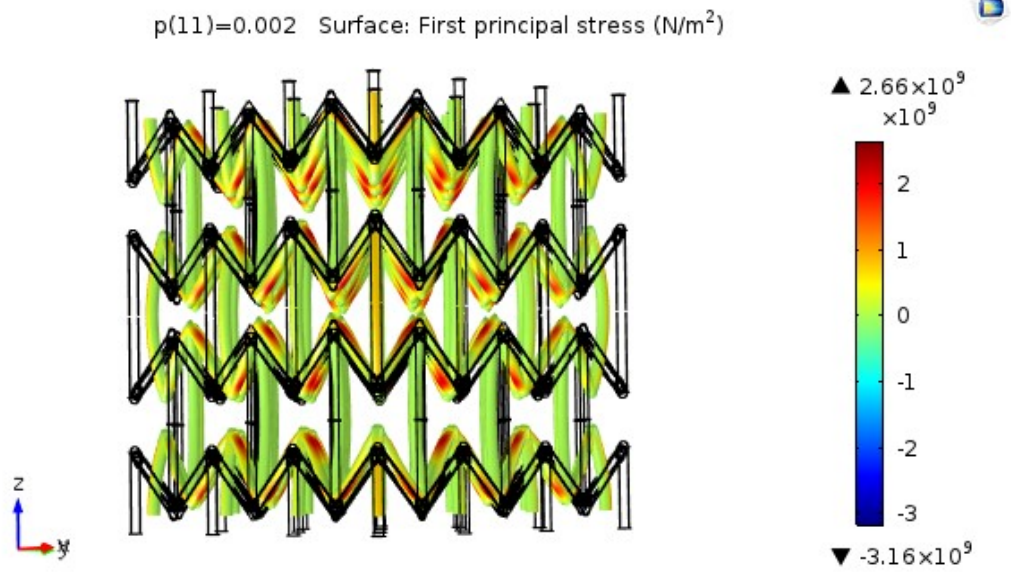
Reference: Own authorship (2018).

Observing Figure 61, geometry A has a negative Poisson ratio (< -0.51) in a deformation range from 0 to 5 mm. Besides, the behavior of the curve is approximately linear, thus, geometry A can be considered auxetic since it has a Negative Poisson Ratio – NPR.

On the other hand, as it can be observed in Figures 62 and 63, geometries B and C presented similar behavior, both presented positive ν in a deformation range comprised between 0 and 2.5 mm. Finally, as last remark, the non-linearity of Poisson’s coefficient values has to be taken into consideration.

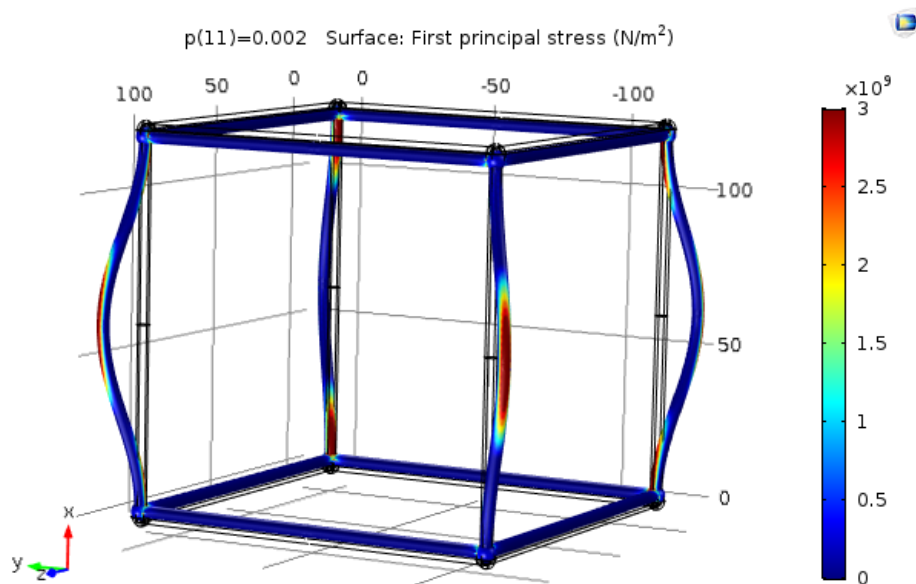
The first major stresses generated by the 3.3% deformation of transverse length brought the correspondent stress distributions for geometry A (Figure 64), geometry B (Figure 65), and, geometry C (Figure 66).

Figure 64 – Stress distribution in geometry A, referring to the first major stress.



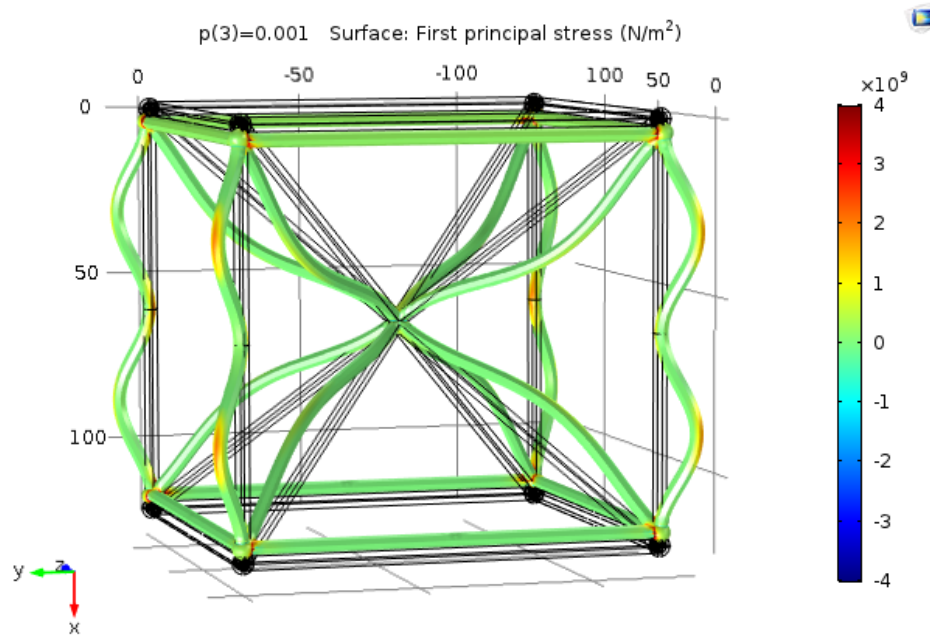
Reference: Own authorship (2018).

Figure 65 – Stress distribution in geometry B, referring to the first major stress.



Reference: Own authorship (2018).

Figure 66 – Stress distribution in geometry C, referring to the first major stress.



Reference: Own authorship (2018).

After complete modeling, it can be inferred from the graphs of stress distribution for each geometry that, geometry A presented a maximum stress concentration of 9.52 GPa while geometries B and C presented 24.6 GPa and 58.6 GPa, respectively. Thus, there is a significant decrease in the intensity of internal stresses of the structures in function of the deformation of the material, which is due to the choice of geometry. This property has a direct influence in the final density of the part. In this sense, the relative density of the geometries is the following: A = 6.7%; B= 2.0% and C= 3.1%.

Still, there are some imprecisions due to the mechanical model adopted in COMSOL: the software considers that the deformation is linear in all dimensions (isotropic deformation). Moreover, there can be observed a buckling phenomenon in several sections of the structure, which can be a consequence of thin walls.

When an anisotropic case is considered, the inclusion of an elastic matrix composed of several coefficients is a major enhancement to increase calculation accuracy. Thus, instead of a single elastic modulus average value, different other coefficients are considered.

In the following, tests were made to determine the influence of struts diameter in the compression resistance for all simulated geometries.

The struts were simulated both with constant length and variable diameter, with an increment step of 10% in the diameter after each simulation, the length was fixed as 30 mm. The height/diameter ratio was obtained, as shown in Table 23.

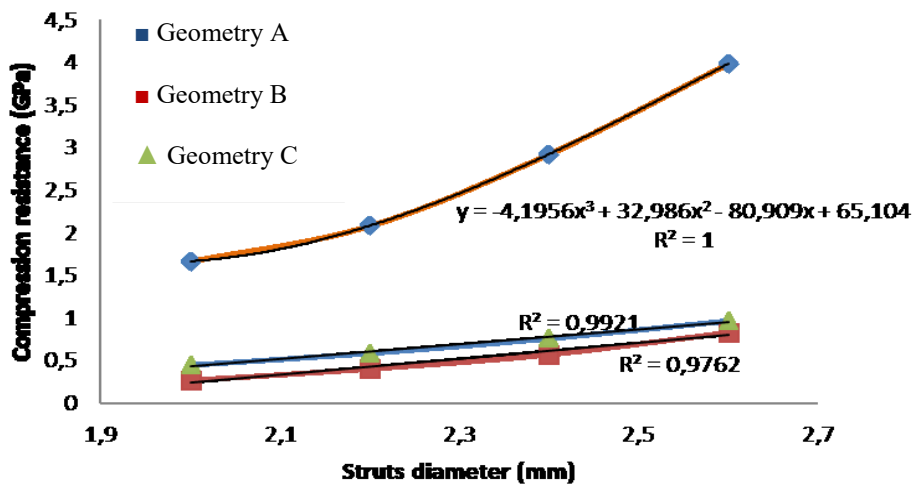
Table 23 – Height/diameter ratio for structures and struts diameter.

Height/diameter ratio	Struts Diameter (mm)
15.00	2.00
13.64	2.20
12.50	2.40
11.54	2.60
10.71	2.80

Reference: Own authorship (2018).

Correlatively, simulation determined the compression resistance curve in function of struts diameter for each geometry. Compression resistance curves are shown in Figure 67.

Figure 67 – Compression resistance in function of strut diameter for geometries A, B and C.

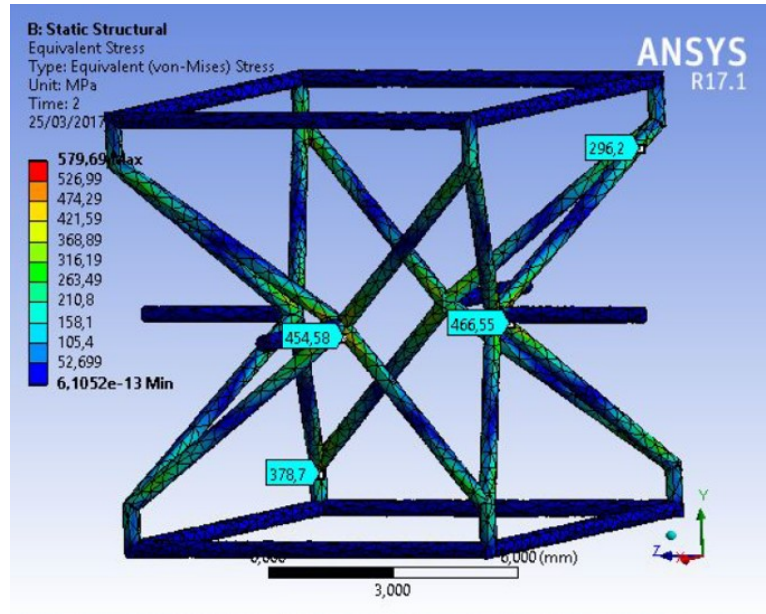


Reference: Own authorship (2018).

The increase in strut diameter implies in greater density of structure A, which allows it to withstand higher loads, explaining a part of the growing tendency of compression resistance, as shown in Figure 67. Furthermore, between all three geometries, the highest increase in compression resistance was verified for geometry A. This particular geometry presented a non-linear behavior and the highest capacity of bearing loads under compression.

Further on, new tests with auxetic models proposed in the literature such as the structure proposed by *Imbalzano et al* (IMBALZANO, 2017), Figure 68, were performed on Ansys 17 software. During simulation on STR2, many singularities and high stress regions were detected, especially in the joining sections of the struts (Figure 68).

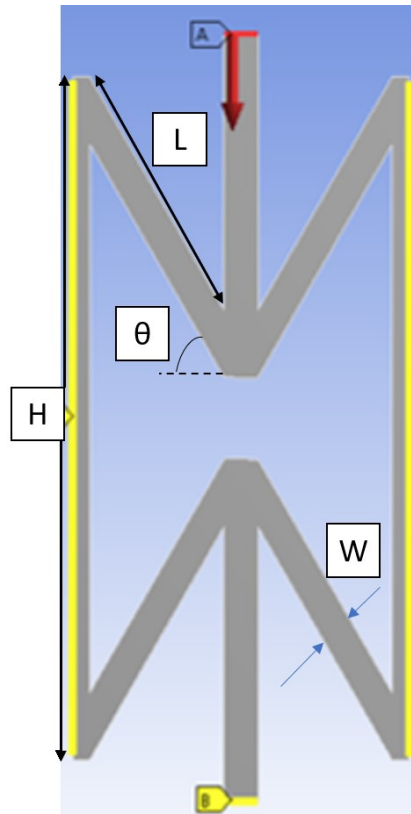
Figure 68 – Compression test in auxetic structure STR2.



Reference: own authorship (2018).

Following the results from Ansys 17 compression tests with STR2 (Figure 68), new geometries were investigated aiming improved mechanical performance and less points of singularities. After this literature survey, a new auxetic re-entrant structure was considered with attention - STR3. It was first presented in an article by *Evans et al* (EVANS, 1994): it presents a great ease on parametrization, tunable mechanical properties, high compatibility of production by most of the AM processes, especially SLM and EBM. Then, as preliminary simulations results demonstrated a great potential in the elastic regime, the object of study was finally determined (Figure 69).

Figure 69 – Auxetic structure STR3 and their geometric parameters in a 2D view.



Reference: Own authorship (2018).

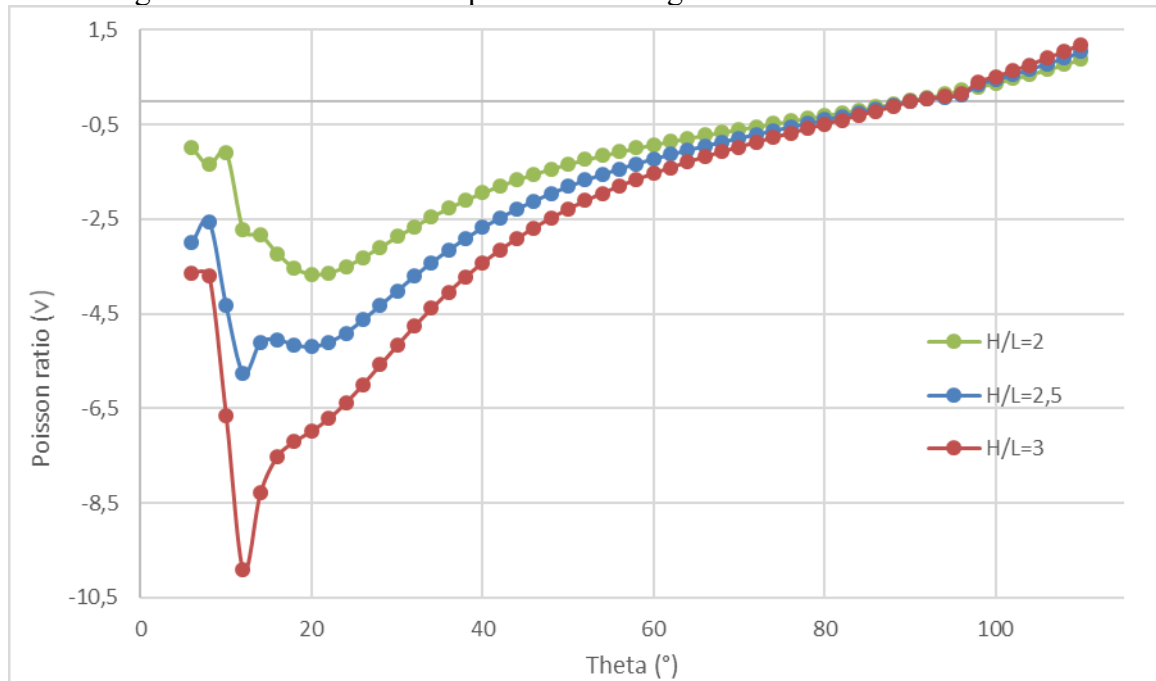
A 2D parametric model was created with Ansys 19 software, including four main features: H (height of main vertical strut); L (length of main diagonal strut); W (width of struts); and, θ (angle between H and L). Symmetry functions were used to obtain the model and perform mechanical simulations. In this case study, the focus was on the determination of Poisson ratio dependence on STR3 parameters (H, L, W and θ).

After concluding geometric parametrization, simulations in elastic regime were implemented: a force of 1 N is applied in the upper part of the structure - red arrow at point A (Figure 69). For the sake of convergence, supports are distributed on the structure borders (sides and bottom), shown in yellow marks at point B (Figure 69). Finally, after the load is applied, the respective transverse and axial deformation are measured.

The influence of each of the four geometric STR3 parameters (H, L, W and θ) was determined by a series of static simulations both in plane strain and plane stress cases (Figure 70). At first, a H/L ratio ($H/L > 2$) was fixed and $W = 1$ mm, angle theta was swept in the [6, 110] interval – $\theta < 6^\circ$ implies in non-physical results, and, were not considered in this

analysis. Moreover, as θ increases, the structure becomes less auxetic, i.e., Poisson ratio (ν) becomes positive after 90° . Besides, for each H/L ratio, a maximum of auxetic behavior is verified in a specific theta value: when H/L= 2, $\nu = -3.66$ @ $\theta = 22^\circ$; in the other hand, as H/L=2.5, $\nu = -5.75$ @ $\theta = 12^\circ$; and, finally, H/L=3, $\nu = -9.90$ @ $\theta = 12^\circ$.

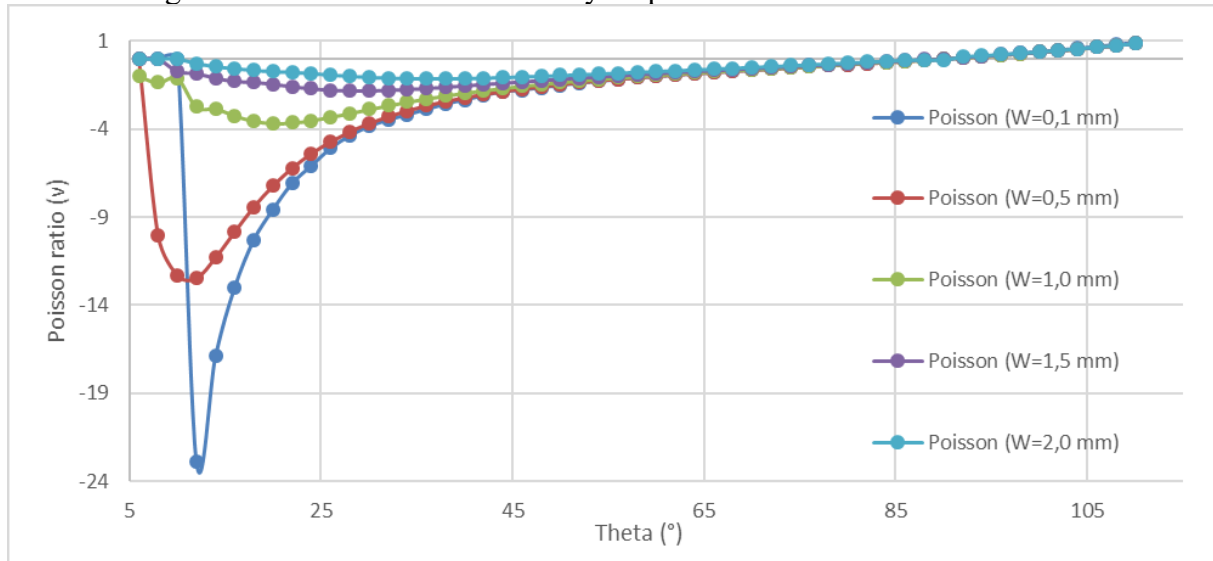
Figure 70 – Poisson ratio dependence on angle theta and H/L ratio.



Reference: Own authorship (2018).

A similar study was performed on the parameter W , fixing a H/L ratio and sweeping angle theta in the $[6, 110]$ interval. As verified in the previous analysis, an increase in theta produces a shift towards positive values of ν . Furthermore, as W increases, stiffness is dramatically augmented, revealing a less pronounced auxetic behavior, as shown in Figure 71. Still, for $W=2$ mm Poisson ratio is negative in a wide θ range: from 6° to 88° .

Figure 71 – Poisson ratio sensitivity on parameter W for H/L=2.



Reference: Own authorship (2018).

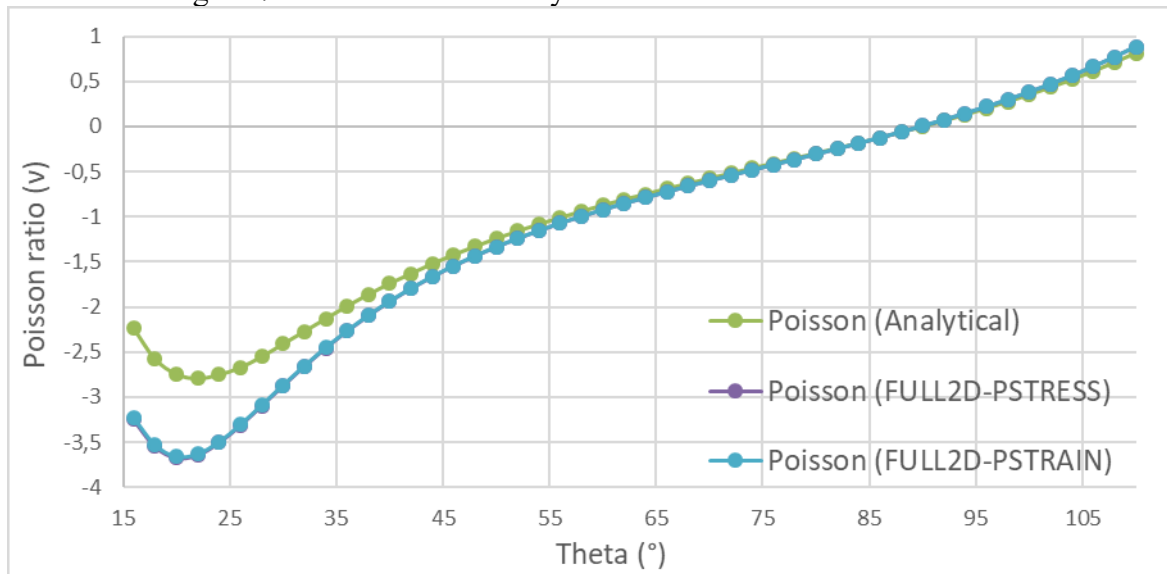
In all geometric parameter cases (Figures 70 and 71), it was verified the equivalence of plane stress and plane strain simulations, which brings a good accuracy to the ANSYS 19 results. Simulation data were found to be in good agreement with an analytical formulation, equations (7) and (8), proposed by Wang *et al.* (WANG, 2017), by which Poisson ratio is calculated through the values of geometric parameters (H, L, W and θ), E (Young modulus) and G (shear modulus).

$$v_{zx} = -\frac{\varepsilon_x}{\varepsilon_z} = \frac{5EGb^3 + 6b(Ew)^2 \left[(\cos(\theta))^2 - \left(\frac{h}{l}\right) \cos(\theta) \right]}{5EGb^3 [\sin(\theta)]^2 + 6b[Ew \sin(\theta)]^2 + 20EGc \cdot w^2} \quad (7)$$

$$b = l - \frac{0.6w}{\sin\theta} - \frac{0.4w}{\tan\left(\frac{\theta}{2}\right)} \quad \Bigg| \quad c = h - \frac{w}{\tan\left(\frac{\theta}{2}\right)} \quad (8)$$

A comparative study was realized between the numerical solution obtained by Ansys software and the analytical solution in equations (7) and (8). Major differences are observed in the θ range of [15, 45]; as θ exceeds 45°, analytical and numerical solutions present equivalent results (Figure 72).

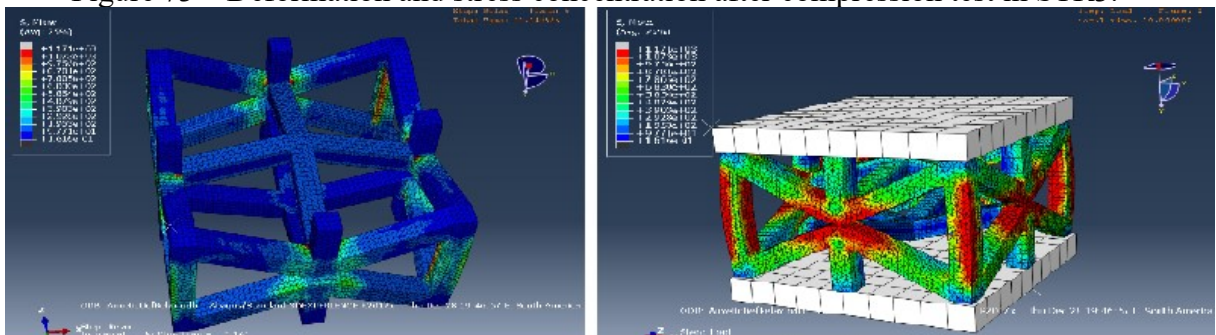
Figure 72 – Poisson ratio analytical and simulation results.



Reference: Own authorship (2018).

Considering only static regime, the ideal parameters to create a highly auxetic structure would be $H/L= 4$ and $W= 0,1$ mm. Nevertheless, as the struts become thinner, fragility and bending are more prone to happen, bringing the need to a further understanding on the deformation behavior (Figure 73). A thicker wall, in the [0.3, 0.5] mm range and $H/L=2$ produces a structure with pronounced auxetic performance (Figure 71, dark blue and red curves) and has significant gain in compression resistance.

Figure 73 – Deformation and stress concentration after compression test in STR3.



Reference: Own authorship (2018).

As static tests proved satisfactory results, a short series of dynamic simulations were implemented using the following geometric parameters: $H/L= 2$; $w= 1$ mm and $\theta= 24^\circ$. Through LSDYNA, a dynamic mechanics package from ANSYS 19 software, it is possible to create time-lapse essays that are similar to ballistic testing. In this series of simulations,

STR3 - coupled with a thin stainless-steel plate - was used as shooting blank for a standard 7.62x39 mm caliber cartridge, a standard in AK-47, and, AK-15 assault rifles (ROSOBORONEXPORT, 2021), with mass of 9.0 g. Results from ballistic simulation are shown in Table 24.

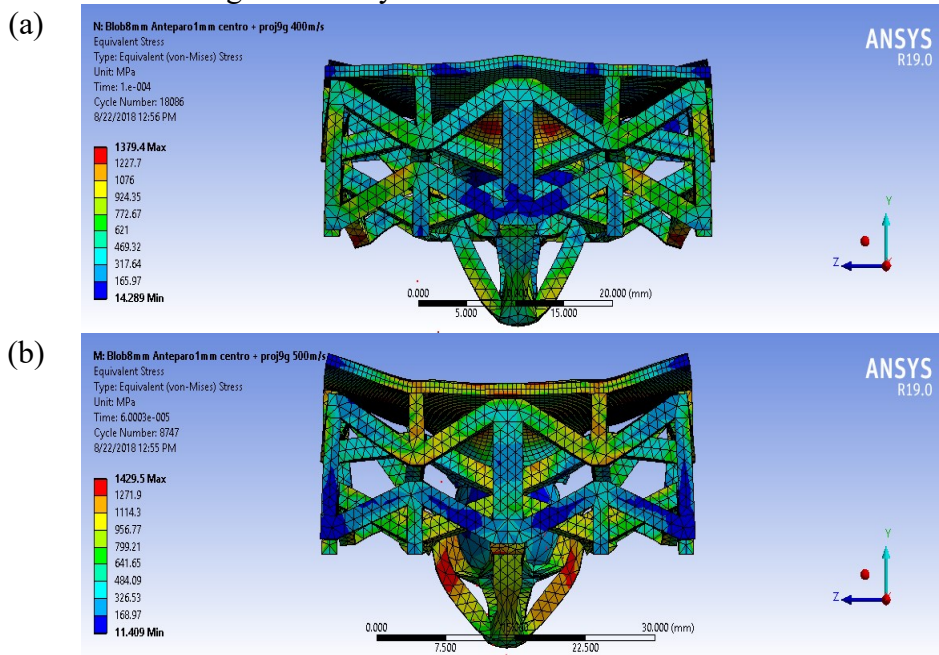
Table 24 – Absorbed energy on STR3 after ballistic impact.

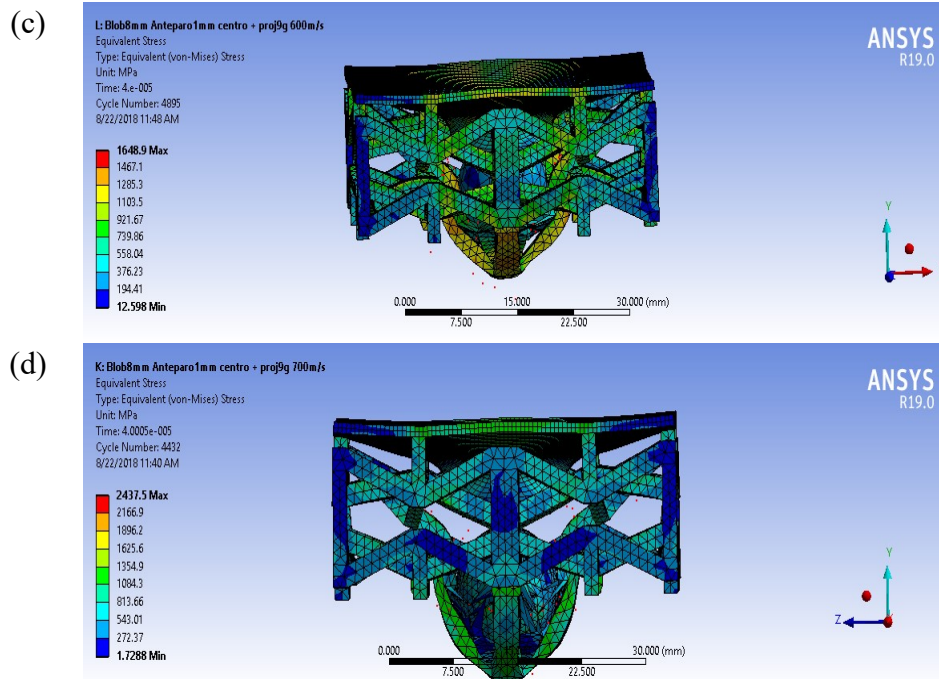
Initial speed (m/s)	7.62 mm projectile			Sample STR3
	Initial Energy (J)	Residual speed (m/s)	Residual Energy (J)	Absorbed Energy (J)
100	35.5	0	0	35.5
200	142.0	0	0	142.0
300	319.6	0	0	319.6
400	568.2	0	0	568.2
500	887.8	168.0	100.2	787.5
600	1278.4	354.9	447.2	831.2
700	1740.1	465.3	768.9	971.1

Reference: Own authorship (2018).

For initial speeds below or equal to 400 m/s (Figure 74(a)), STR3 is able to absorb all of the impact energy and successfully stop the 7.62x39 mm bullet. Furthermore, as the bullet speed increases, strain attains critical levels, leading to progressive damage of struts (Figure 74(b) and (c)), and, finally, mechanical failure of STR3 (Figure 74(d)).

Figure 74 – Dynamic test on STR3.





Reference: Own authorship (2018).

5.2 FABRICATION OF AUXETIC METALLIC SAMPLES

In this section, powder material was characterized for the production of samples by SLM. First, a microstructural analysis of stainless steel 316L powder was performed, and, then parts were produced by SLM. Similarly, Ti-6Al-4V powder was studied and auxetic samples were fabricated using the aforementioned AM method.

5.2.1 Characterization of Stainless Steel powder

In a first moment, CL20ES SS powder composition was analyzed. Major components of this powder and their respective percentage, as well as important mechanical properties (density, ultimate tensile strength, Yield strength, and, Young modulus) are described in Table 18 CL20ES SS (AISI SS316L).

Figure 75 shows an optical microscopy microsection analysis of a CL20ES component: a dense and homogeneous structure is formed as CL20ES powder is processed by SLM.

Figure 75 – Optical microscopy of CL20ES test piece.



Reference:(LASER, 2018)

This powder is an austenitic Stainless Steel with high contents of Chromium and Nickel. Minor alloying elements are Molybdenum, Manganese, Silicon, Phosphorus, Carbon and Sulfur. Its properties are very similar to the SS types shown in section 3.1.3 (page 30).

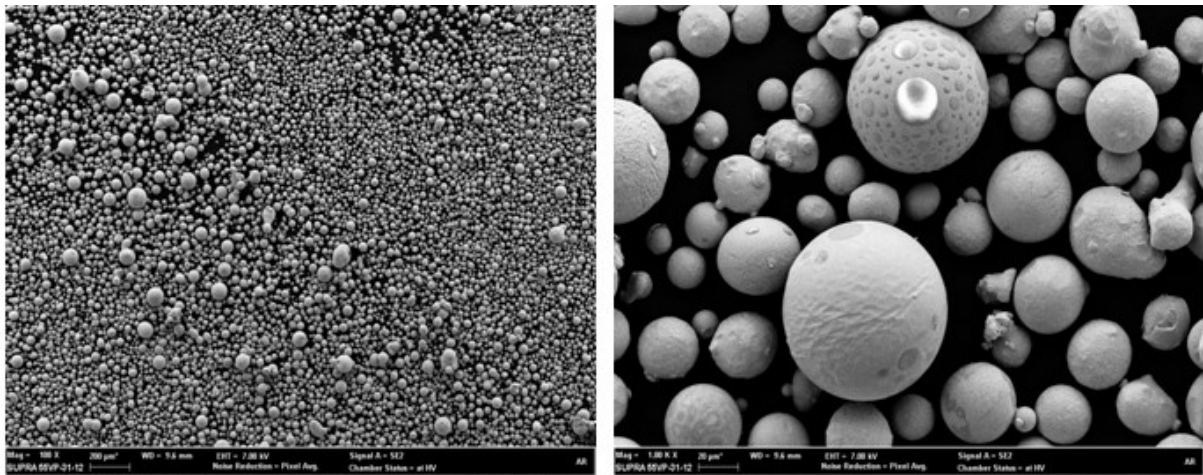
The process used to transform the fused SS material in powder is gas atomization, with the use of Argon. Since the supplier did not furnished a complete powder datasheet, further steps of characterization had to be performed in order to ensure the quality of this powder material.

In order to complement data obtained from ConceptLaser datasheet, CL20ES powder was characterized by the following techniques: Scanning Electron Microscope (SEM) with Field Emission Gun (FEG); Dynamic Analysis of Particles; Energy Dispersive X-Ray Spectroscopy (EDS or EDX).

Granulometry analysis was performed by Scanning Electron Microscope (SEM) using FEG (*Zeiss EVO*) and for the Dynamic Analysis of Particles, model Particle Insight 2.55 from *Particulate Systems* was used, aiming to characterize size distribution and form of grains since they could influence fluidity and performance while processing. The information related to the form of the raw material (circularity, suavity and aspect ratio) increase process control to higher levels rather than details about the size of the particulate. Those measurements are essential when powder is recycled, to understand the influence of reuse in the powder and SLM - part features.

The results of the CL20ES SS powder analysis reveal grains with spheroidal form, ideal for performance and fluidity increase during fabrication process. This influences the uniformity of each layer, as well as the packing factor of the particulate material with consequent reduction of empty spaces, which avoids undesirable porosity and allows the reproducibility of the process. Thus, the Gaussian curve is maintained by the standardization of grain distribution, allowing the control of porosity, those features are due to the use of gas atomized powders. Figure 76 explicit the average spheroidal form of powder particles, despite the presence of different dimensions and non-spheroidal particles (Power source: 7 KV, Detector: Secondary Electrons SE2).

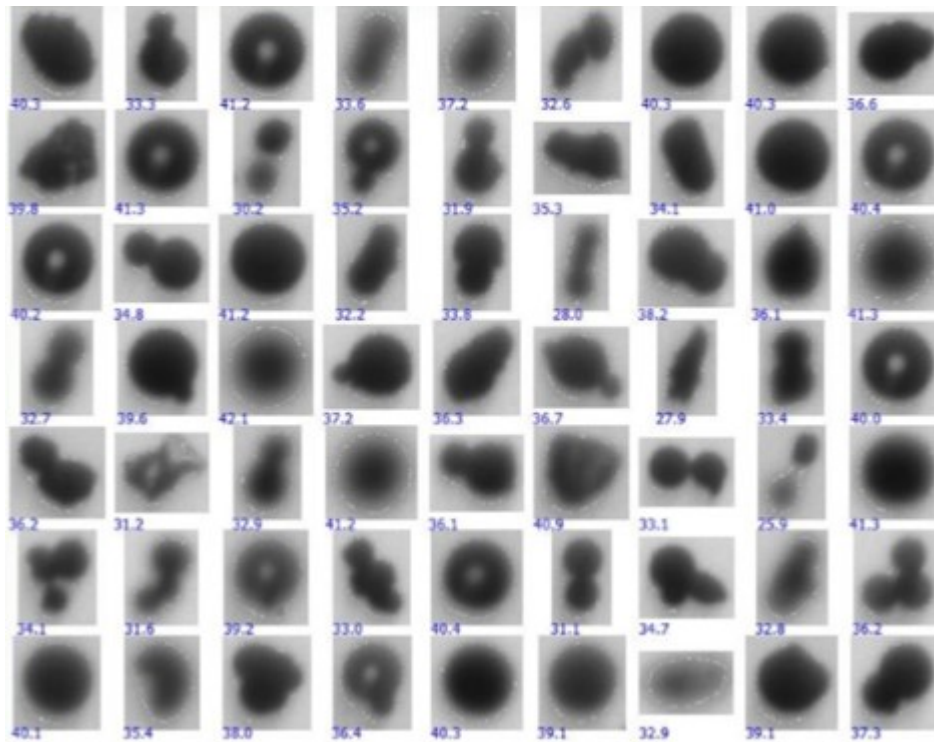
Figure 76 – CL20ES powder SEM analysis: amplification of 100 and 1000 x.



Reference: Own authorship (2018).

Further image analysis was performed using Particle Insight 2.55 from Particulate Systems, allowing to study the particulate size and their morphology. In this sense, both diameter and their roundness, size, aspect ratio and suavity were critical factors. Figure 77 presents different types of particles with sizes in micrometers (μm) for both powders.

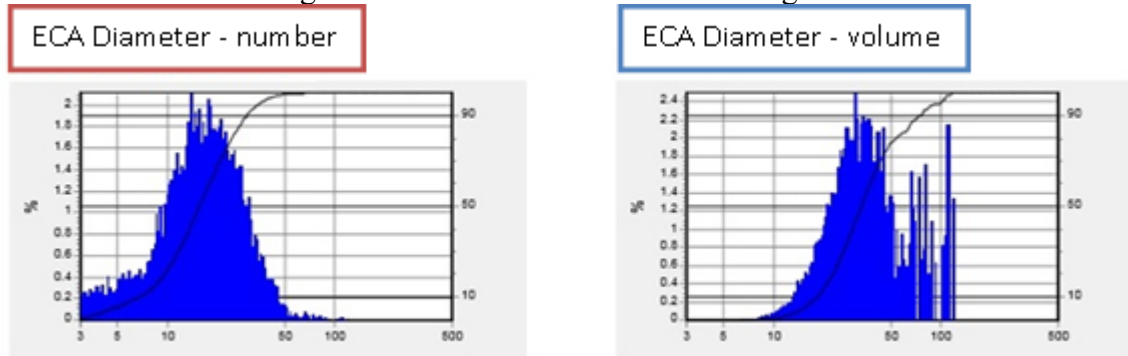
Figure 77 – Morphology and size measurements of CL20ES powder particles.



Reference: Own authorship (2018).

Grain size distributions are represented on Table 25. The narrower the distribution, the bigger the recurrence of grains with similar sizes. In this case, it is possible to verify the biggest incidence of grain size in a distribution close to the interval between 10 to 40 μm .

Table 25 – Histogram related to circular diameter and grain volume.



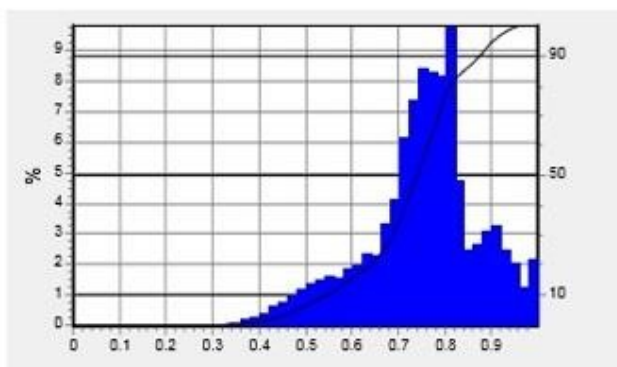
Summary of sample analysis (size in μm)

Count	9351	Percentage (%)		Percentage (%)		Volume %		Dp,q	
Minimum	3.0	10.00	6.8	10	14.2	10	18.5	D1,0	17.8
Maximum	117.8	25	10.8	25	19.5	25	24.9	D2,0	20.5
Average	17.8	50	15.9	50	26.9	50	34.0	D2,1	23.6
Standard Deviation	10.2	75	22.8	75	36.7	75	48.5	D3,0	23.5
								D4,3	41.0

Reference: Own authorship (2018).

Roundness parameter (aspect ratio) of particles influences in flow and fluidity during SLM fabrication process. It is noted that in Table 26, the metallic powder (average parameter value of 0.749) has a narrow distribution and it is close to 1 (perfect roundness). Average values above 0.7 reveal high roundness. Therefore, it can be concluded that Concept Laser particulate is predominantly circular, which corroborates previous findings observed in SEM-FEG images.

Table 26 – Histogram related to roundness (aspect ratio).



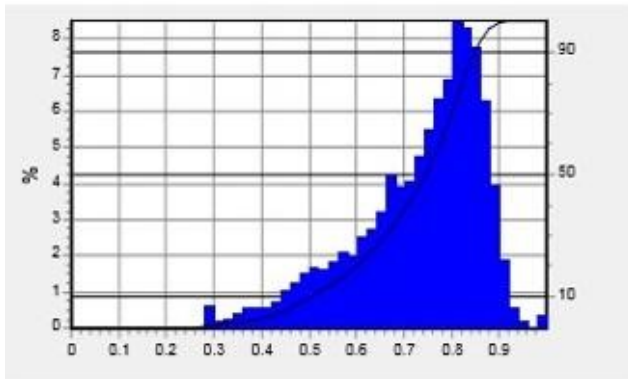
Sample analysis summary

Count	9453	Percentage (%)	
Minimum	0.128	10.00	0.568
Maximum	1.000	25.00	0.690
Average	0.749	50.00	0.762
Standard Deviation	0.126	75.00	0.819

Reference: Own authorship (2018).

The suavity parameter is detailed in Table 27: the distribution of suavity gives the information about the rugosity of the powder particulate. The relatively narrow distribution with average value close to 1 (0.729), suggests a low rugosity.

Table 27 – Histogram related to suavity.

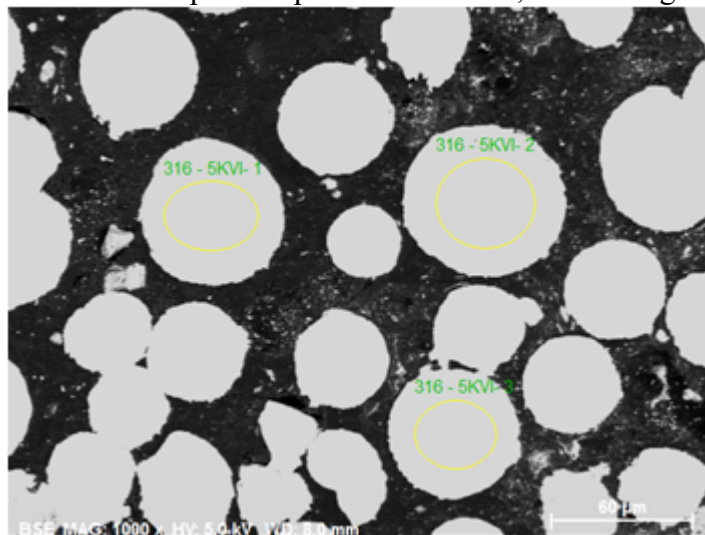


Sample analysis summary			
Count	9454	Percentage (%)	
Minimum	0.292	10.00	0.524
Maximum	0.997	25.00	0.654
Average	0.729	50.00	0.765
Standard Deviation	0.136	75.00	0.831

Reference: Own authorship (2018).

From the results analyzed so far, the CL20ES powder from Concept Laser presented a majority of spheroidal particulates, with few defects (Figure 78), as observed in powders prepared by gas atomization process.

Figure 78 – CL20ES powder particles on SEM, 1000x magnification.



Reference: Own authorship (2018).

5.2.1.1 Chemical composition analysis of SS powder

The results of chemical composition analysis performed using EDS/EDX (Energy dispersive X-ray spectroscopy) were measured and explained on Table 28 and Figure 72: based on experiments, it can be noted that the nominal powder composition presents 61.15 to 63.01 %w of Iron; 17.24 to 17.70 %w of Chromium; 9.93 to 11.02 %w of Nickel; 2.29 to 2.58 %w of Molybdenum; 0.51 to 0.89 %w of Silicon, and, 1.27 to 1.83 %w of Manganese (in weight percentage - %w). Several other elements were found in lower quantities: Carbon, Oxygen and Sulphur (the sum of these three elements oscillate between 2.97 and 7.61 %w). Thus, the CL20ES powder is in fact an AISI SS316L, containing Chromium and Nickel with 18% and 10%, respectively.

Comparing the data obtained by EDS of CL20ES powder (Table 28) with Table 18, a significant difference between the values of iron content can be verified: while CL20ES powder EDS analysis reveal 61.15 to 63.01 %w of Iron, CL20ES powder datasheet reveal 62.9 to 71.5 %w, which can provide uncertainty. On the other hand, for other metals such as Mo, Si, Mn, Cr and Ni, no significant difference in w% can be observed.

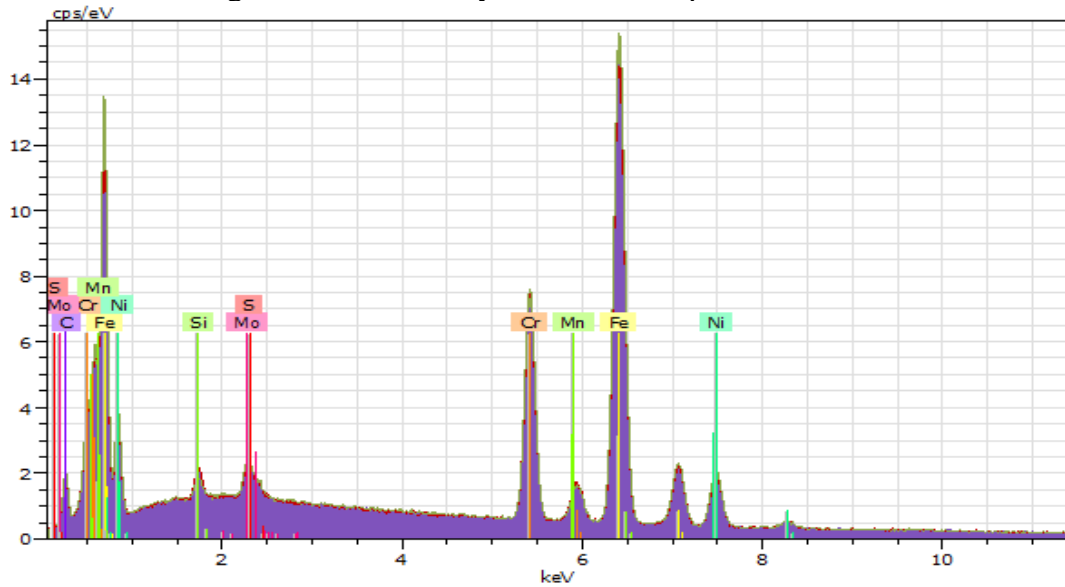
Table 28 – Results from EDS analysis of CL20ES chemical composition.

Measurements (Spectra)			
Chemical composition	%w	Chemical composition	%
Silicon	0.7 ± 0.1	Molybdenum	2.4 ± 0.1
Chromium	17.4 ± 0.1	Manganese	1.5 ± 0.2
Nickel	10.5 ± 0.3	Iron	62.1 ± 0.5

Reference: Own authorship (2018).

Figure 79 presents the chemical composition of CL20ES, when characterized by EDS method, which was performed using EDS ZEISS EVO (SEM) module. The particles were embedded in conductive resin and prepared with abrasion in sandpaper of 320, 600 and 1200 MESH followed by polishing via diamond solution of 3 µm and 1 µm. The analysis was performed with magnifications of 1000 times operating a power source of 5 kV.

Figure 79 – EDS analysis of CL20ES powder.



Reference: Own authorship (2018).

5.2.2 Fabrication of SS samples

Auxetic and conventional structures based on SS powder were obtained by Selective Laser Melting (SLM). The SLM machine used for sample fabrication was model M2 Cusing from CONCEPT Laser, a member of German group *HOFMANN Innovation Group GmbH* (recently acquired by General Electric - GE), is shown in Figure 80.

Figure 80 – SLM machine M2 Cusing from ConceptLaser.



Reference: Own authorship (2018).

With M2 Cusing system, complex geometries parts with fine precision can be obtained. The possibility of changing several parameters and fabrication strategies, as well

as the use of different metallic materials such as steel for hot forging, SS, titanium alloys, aluminum alloys, nickel alloys, makes this platform very well suited for research and development. The main characteristics of this machine are presented in Table 29.

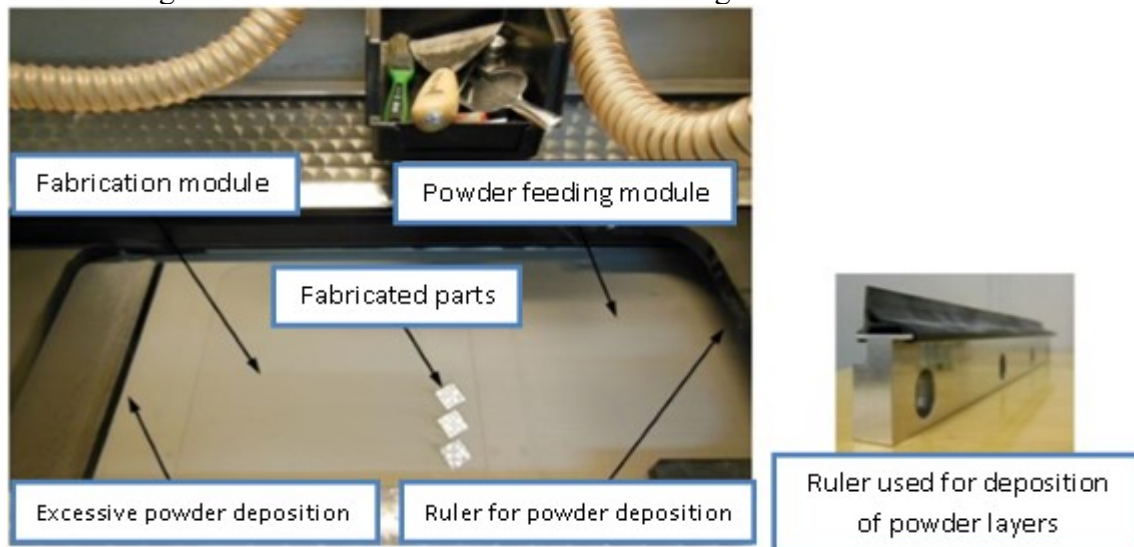
Table 29 – Features from M2 Cusing SLM machine.

Building area specifications	Model: M2 Cusing
Maximal dimensions of fabrication (x,y,z) (mm)	250 x 250 x 280
Layer thickness (μm)	20 – 80
Building speed (cm ³ /h)	2 – 20
Laser specifications	Type: Fiber; Power: 400 W
Maximal scanning speed (m/s)	7
Beam diameter (μm)	50 – 200
Machine dimensions (width x length x height) (mm)	2440 x 1630 x 2354
Weight (kg)	2000

Reference: Adapted from (GE, 2018).

Building area provides a closed environment with an inert gas (Argon or Helium) for reactive materials such as stainless steel, titanium and aluminum alloys. In specific cases such as Maraging 300 (Martensitic Steel strengthened with 18 % of Nickel and 7.5 – 12 % of Cobalt), nitrogen is used as shielding gas during fabrication. Figure 74 reveals the building chamber of M2 Cusing. Prior to fabrication, the powder is transferred from the feeding module to the fabrication module. In the following, a powder layer is spread by a ruler (metallic or heat-resistant thermoplastic), which is chosen according to the powder and part geometry. In this research, a heat-resistant thermoplastic ruler was used.

Figure 81 – Fabrication area inside M2 Cusing SLM machine.



Reference: Own authorship (2018).

Table 30 describes SLM processing parameters used for the fabrication of samples, which were set combining standard ConceptLaser fabrication setup, literature review, and, experimental testing. Both samples were fabricated following norms from ISO ASTM E9 – standard test methods of compression testing of metallic materials at room temperature (ASTM E9-19, 2019).

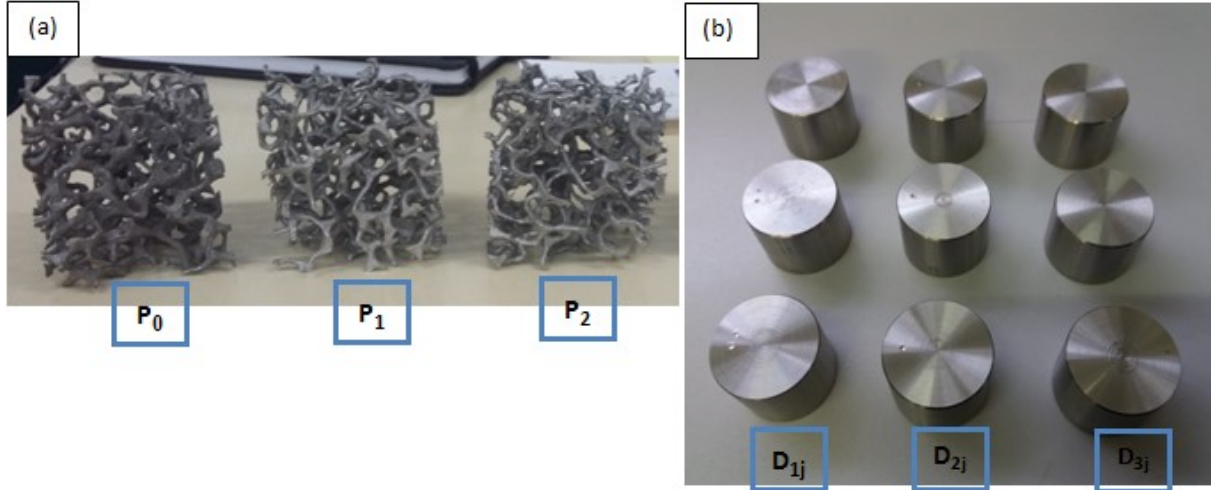
Table 30 – SLM processing parameters employed in SS sample fabrication.

Power (W)	Scanning speed (mm/s)	Layer thickness (μm)	Density of energy (J/mm^3)	Interaction time (ms)	Beam diameter (μm)
200	800	30	104.17	100	150

Reference: Own authorship (2018).

A total of twelve samples were fabricated by SLM: 3 were porous (Figure 82(a)) and 9 were cylindrical dense parts (Figure 82(b)). The porous samples are designed as P_i ($i=0,1,2$); dense samples are designed as D_{jk} ($j=k=1,2,3$).

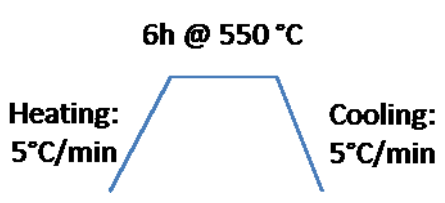
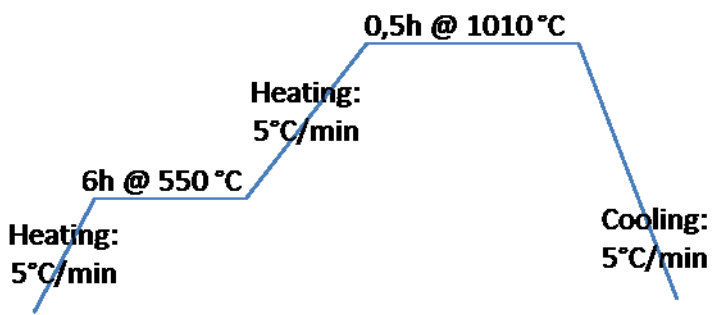
Figure 82 – SLM samples before heat treatment - (a) auxetic geometry part P_i ($i=0,1,2$); (b) cylindrical dense parts D_{jk} ($j=k=1,2,3$).



Reference: Own authorship (2018).

After fabrication, part of the P_i and D_{jk} samples was submitted to different thermal treatments. Since SLM specimens show a significant amount of RS in their structure, which is primarily due to the intense heat transfer (successive cycles of heating and cooling in a short time interval) involved in the laser melting process. In this sense, a stress relaxation is a necessary step, as detailed in Table 31.

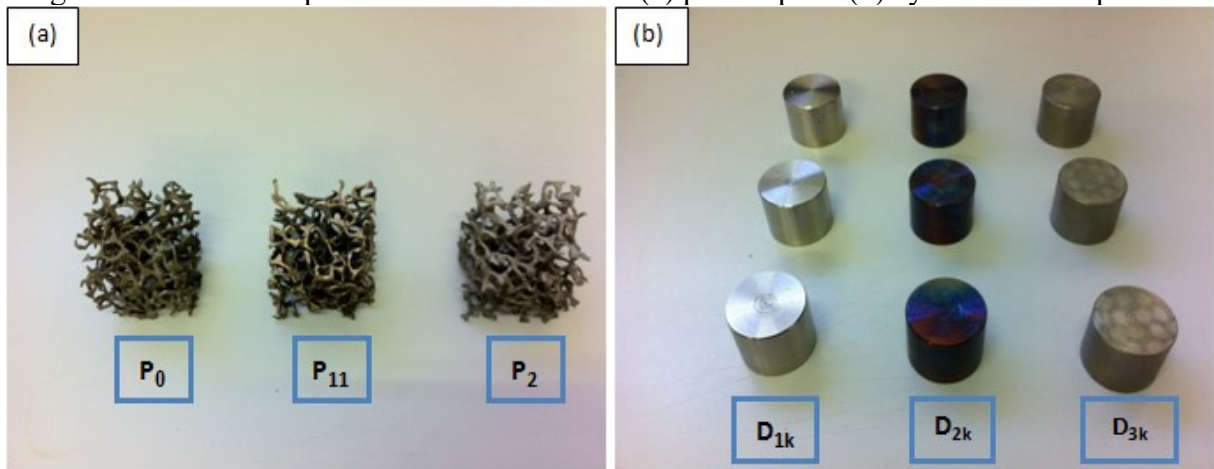
Table 31 – Heat treatment of SLM made samples.

Sample designation	Heat treatment type
P ₀	None Stress relief:
P ₁	 <p>6h @ 550 °C Heating: 5°C/min Cooling: 5°C/min</p>
P ₂	<p>Stress relief + normalization:</p>  <p>0,5h @ 1010 °C Heating: 5°C/min 6h @ 550 °C Heating: 5°C/min Cooling: 5°C/min</p>
D ₁₁ ; D ₁₂ ; D ₁₃	None
D ₂₁ ; D ₂₂ ; D ₂₃	Same as P ₁
D ₃₁ ; D ₃₂ ; D ₃₃	Same as P ₂

Reference: Own authorship (2018).

The aim of these thermal treatments was to minimize surface and internal tensions of the parts. Most of the parts presented few defects and were able to perform compression tests. SS samples after specific heat treatment are shown in Figure 83 (a) and (b).

Figure 83 – SLM samples after heat treatment - (a) porous parts (b) cylindric dense parts.



Reference: Own authorship (2018).

5.2.2.1 XCT characterization of SS-316L samples

Porous samples (P_i) were analyzed by means of computed tomography using X-ray (XCT). This technique consists in the use of X-ray to produce a virtual image of the object under analysis without modification of its structure (non-destructive evaluation). This characterization method has a resolution in the nanometer scale, typically 50 nm to 100 μm (WANG, 2018), for some computed tomographic equipment.

When XCT is coupled with a synchrotron radiation source (SXCT), resolution is dramatically enhanced – typically between 30 nm and 20 μm (NARESH, 2020). Nevertheless, such high precision comes with a drawback: sample size is limited between 20 μm and 50 mm (NARESH, 2020). Moreover, in an article by *Cunningham et al* (CUNNINGHAM, 2016), an EBM sample of Ti-6Al-4V was analyzed by SXCT and a feature with 1.5 μm of diameter was successfully observed.

The equipment used for XCT analysis and acquisition parameters are described in Table 32. XCT analysis of auxetic samples was held at LMPT – UFSC.

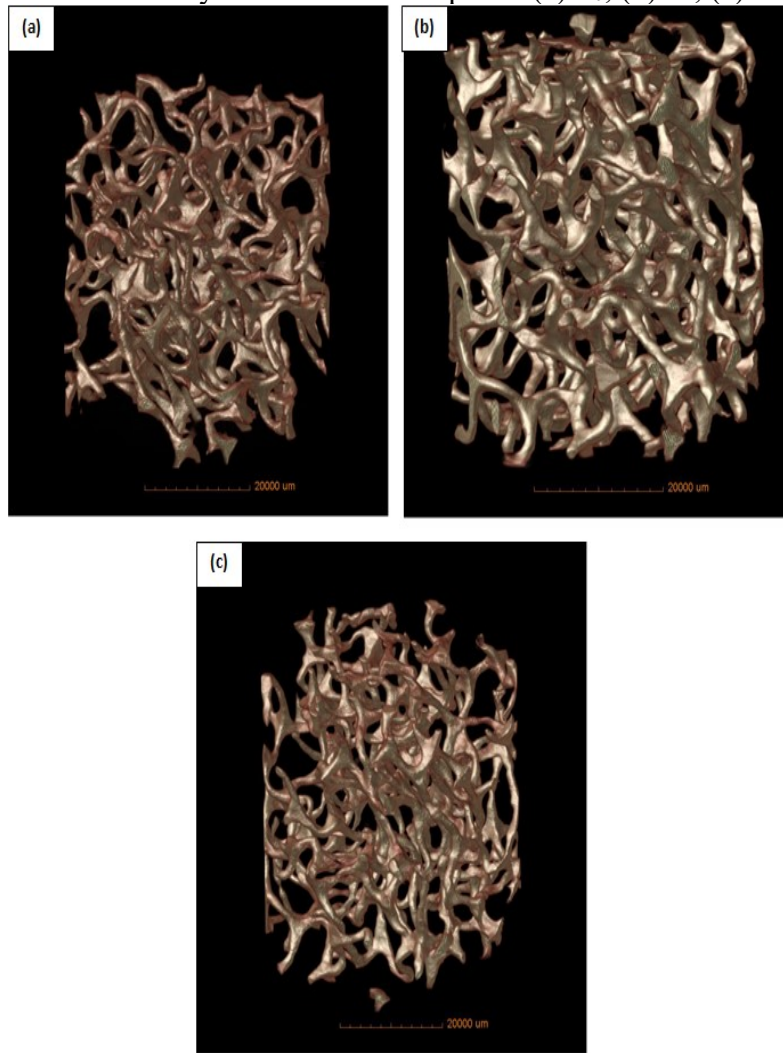
Table 32 – Parameters of acquisition for ZEISS XRADIA 510 XCT equipment.

Equipment: VERSA XRM-500		Resolution (pixel size of image; μm)	50,7
Better resolution (μm)	~ 0.7	Size of 2D image (pixels)	1004*1024
Number of projections	1601	Source power	150 kV/10 W
Angular step ($^\circ$)	0.225	Optical lens (X - augmentation)	0.4
Acquisition times (s)			
P₀	3.0		
P₁	2.5		
P₂	3.0		

Reference: Own authorship (2018).

Images from XCT analysis are shown in Figures 84(a), (b) and (c) and the high amount of porosity contained in all samples is detailed through high definition images. The porosity is also well interconnected. Because of the rotation of the equipment and the hemispheric lens, XCT 3D images are slightly distorted: instead of generating a perfect cube, a cylinder is obtained.

Figure 84 – XCT analysis of SLM P_i samples – (a) P_0 , (b) P_1 , (c) P_2 .



Reference: Own authorship (2018).

Table 33 reveals average pore size (average pore size of P_i samples is 54 mm), percental porosity (average porosity of P_i samples is 91.13%; average density of samples is 6.51 g/cm^3).

Table 33 – Analysis of pores and porosity of P_0 , P_1 , P_2 porous samples.

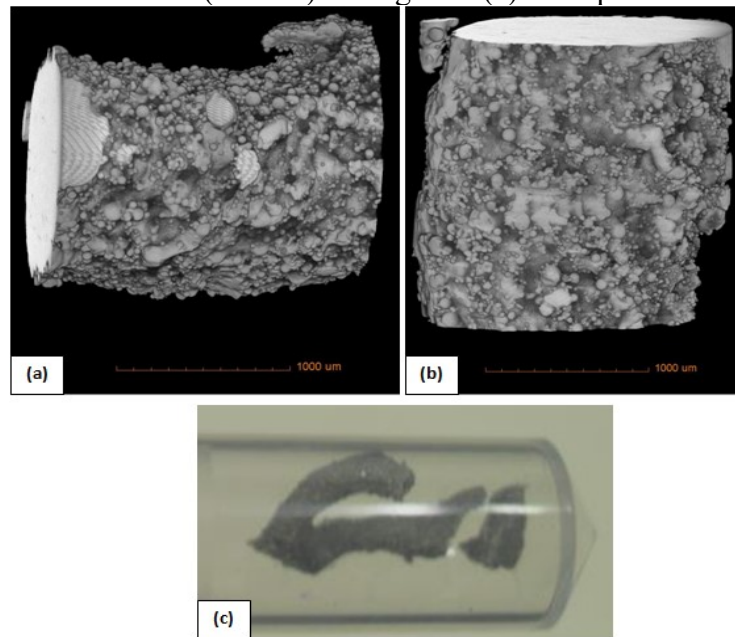
Sample	Average pore size (mm)	Porosity (%)
P_0	50	90.42
P_1	55	90.89
P_2	58	92.07

Reference: Own authorship (2018).

Moreover, a smaller portion of the sample was analyzed using XCT: a strut was extracted from the auxetic SS structure. This smaller portion allowed to observe the high roughness of the sample surface and also the low porosity of the SS part. Figure 85 represent

two amplified lateral cuts (a and b) of the sample and the sample itself (c). Since sample size changed drastically, acquisition parameters were modified: resolution (pixel size of image; μm) was set to $2\ \mu\text{m}$; while acquisition time was increased to 7.5 s; and, a higher optical lens magnification - four times (4X) - was used.

Figure 85 – Lateral cuts (a and b) of fragment (c) from porous SLM sample.



Reference: Own authorship (2018).

Complementarily, Figure 85 (a) and (b) reveal the presence of balling effect in the production of SLM samples. In order to reduce rugosity, an electrochemical treatment could be performed. Still, it was decided not to reduce rugosity since no significant influence in mechanical properties is observed, except for fatigue.

5.2.2.2 Compression tests of SS-316L samples

Samples prepared in section 5.2.2, Figure 82 (a), were characterized in mechanical tests. Compression tests were performed using an EMIC model 23-200. Test setup is described in Table 34.

Table 34 – Setup of compression tests for P_i samples.

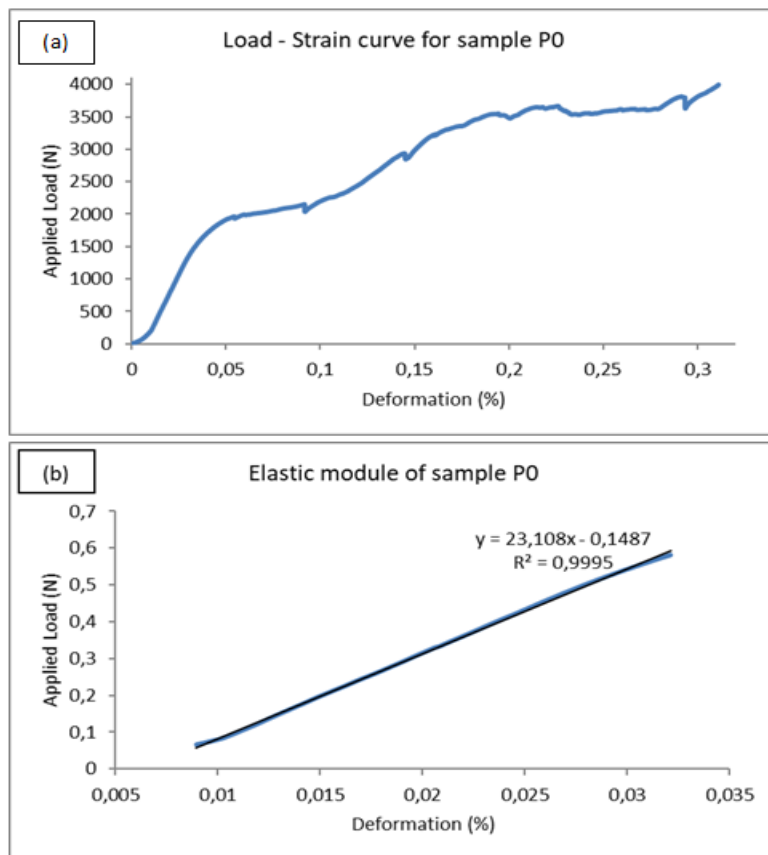
Parameter	Value
Deformation speed (mm/min)	0.20
Maximum Applied load (kN)	3.00

Reference: Own authorship (2018).

Figure 86 (a) and (b) reveals the mechanical behavior of porous sample P_0 under compression, using test parameters from Table 35. Figure 86 (a) reveals that after an applied load, there is a swift drop in stress, which represents the breaking of one portion of P_0 structure. Nevertheless, since structures P_0 , P_1 and P_2 have random layer distribution, stress – strain curve does not present a cyclic behavior, as observed in compression tests of re-entrant auxetic structures (YANG, 2011).

P_0 presented an elastic modulus of 23.11 GPa (Figure 86 (b)) which is very near from cortical bone (RHO et al., 1993). In this sense, this structure could lead to applications in the biomaterials field, such as bone regenerator guides.

Figure 86 – Mechanical behavior of sample P_0 under compression – (a) Load – strain curve; (b) elastic portion of compressive test.



Reference: Own authorship (2018).

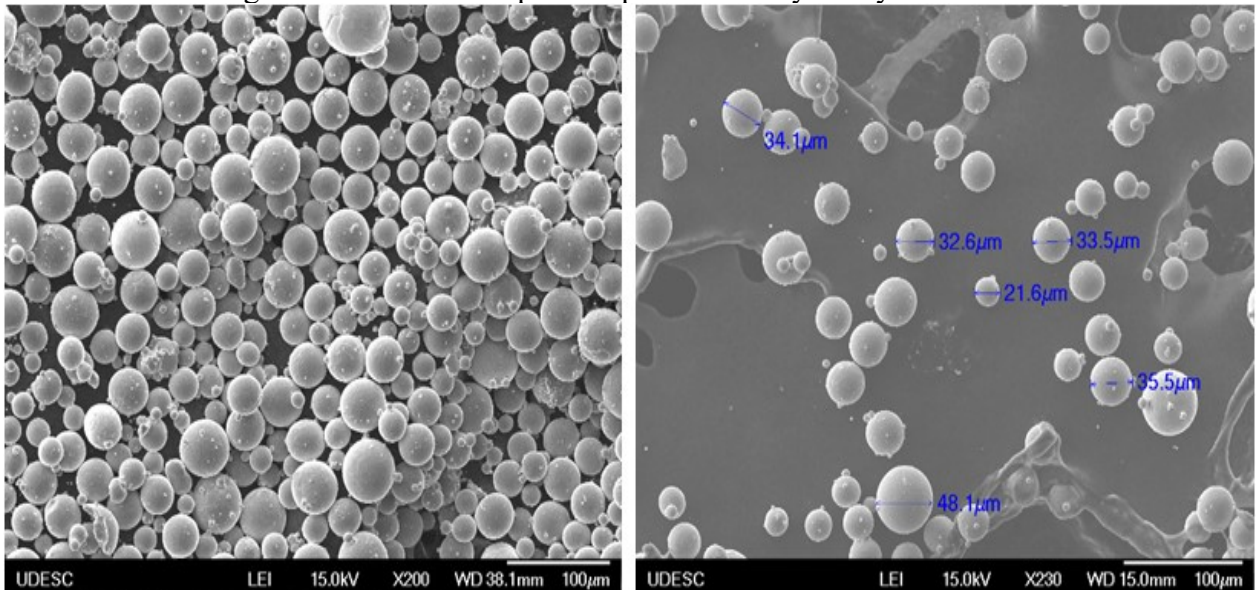
Poisson's coefficient measurements were planned but several technical problems limited the precision of deformation data on these auxetic porous structures. Thus, new tests are planned using more regular geometries, especially STR3.

5.2.3 Characterization of Ti-6Al-4V powder

Ti-6Al-4V powder grade 23 (TEKMAT Ti64-23/20) was supplied by Tekna. It is an Extra Low Interstitial (ELI) and high purity Ti alloy powder, obtained by plasma atomization and its chemical composition is presented in Table 19 (TEKNA, 2018).

The majority of particles have spheroidal form (Figure 87 a and b). These particles presented an average size of 34.23 μm , which was obtained from six measurements performed using ImageJ software. Low agglomeration is observed, as a direct result of plasma atomized metal powders. SEM-FEG analysis was performed using Scanning microscope JEOL JSM-6701F (Figure 56(c)).

Figure 87 – Ti-6Al-4V powder particles analyzed by SEM-FEG.



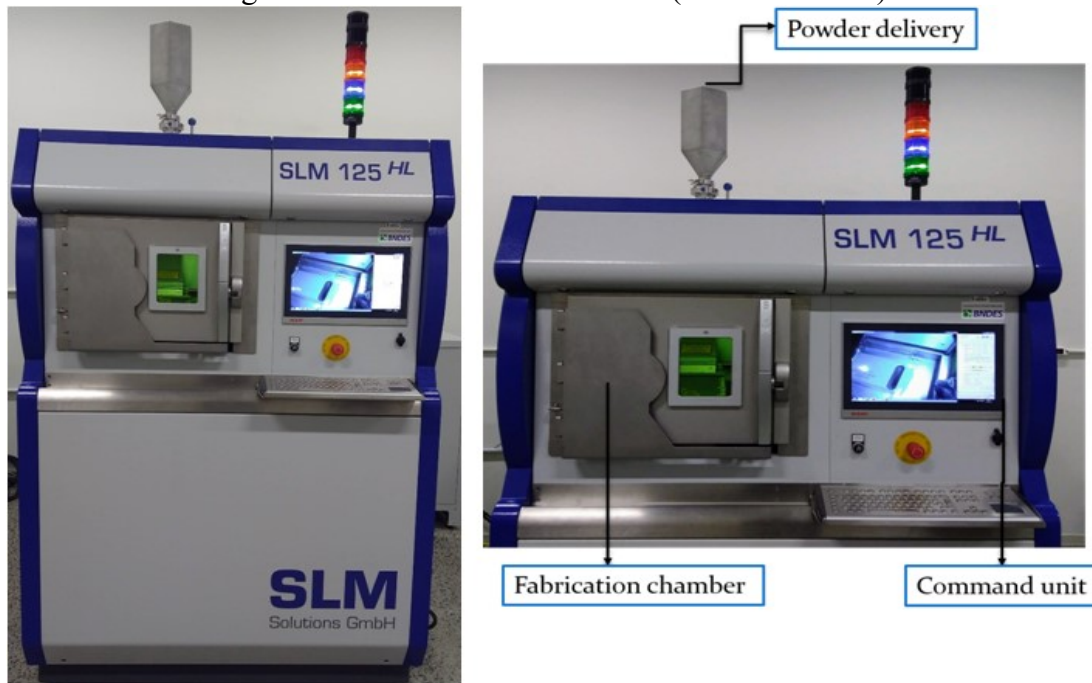
Reference: Own authorship (2018).

5.2.4 Fabrication of Ti-6Al-4V samples

Auxetic Ti-6Al-4V samples were made using Selective Laser Melting Machine 125 HL (Figure 88), by SLM Solutions, which has a very similar operation principle as M2

Cusing (ConceptLaser). Aiming to enhance powder material purity, SLM 125 HL is exclusively dedicated to the fabrication of Ti grade II and Ti-6Al-4V parts.

Figure 88 – SLM Machine 125 HL (SLM Solutions).



Reference: Own authorship (2018).

This machine has a more compact building chamber: 125x125x125 mm³, which implies in a significant reduction in Argon consumption, lowering fabrication costs. It features a single fiber laser with maximal output power of 400 W (continuous wave - CW). It can operate on stainless steel, tool steel, Co-Cr alloys, Ni alloys, Al alloys and Ti alloys. At SENAI ISI, this equipment is exclusively dedicated to Ti-6Al-4V powder processing, due to optimized operation resources, and, also, to avoid powder contamination. Table 36 exposes technical specifications from SLM Solutions 125 HL (SLM SOLUTIONS, 2018).

Table 35 – Main features SLM Solutions 125HL.

Building area specifications	Model: SLM 125
Max. Dimensions of fabrication (x,y,z) (mm)	125 x 125 x 125
Layer thickness (μm)	20 – 75
Building speed (cm ³ /h)	≤ 25
Laser specifications	Type: Fiber; Power: 400 W
Max. scanning speed (m/s)	10
Beam focus diameter (μm)	70 – 100
Average inert gas consumption (Argon) (L/min)	2 (process) 70 (purging)
Weight (kg)	750

Reference: (SLM SOLUTIONS, 2018).

Fabrication parameters are shown on Table 36. For each part of the design (outside, inside, support structure), there is a set of specific parameters which are employed, e.g., support structures are built with lower laser power and higher scanning speeds to ensure powder mechanical support and thermal dissipation.

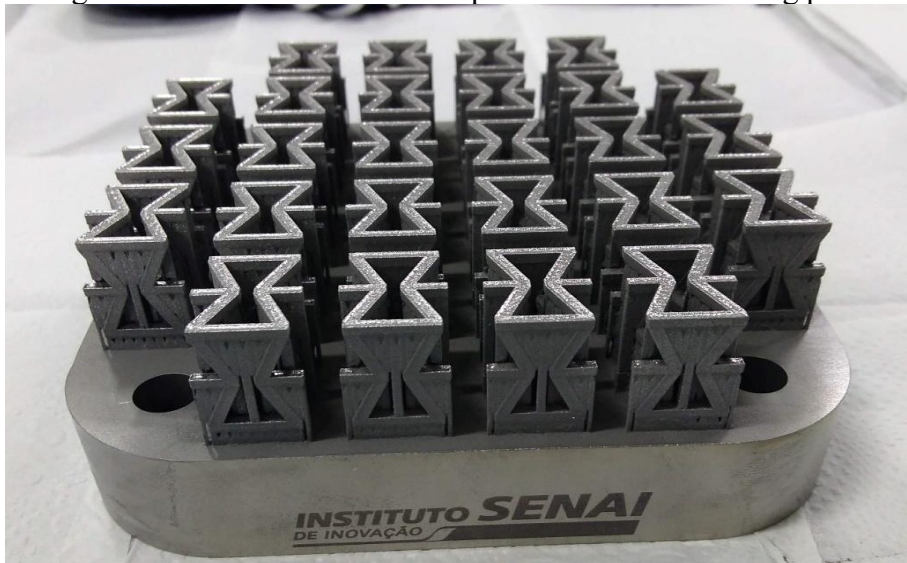
Table 36 – Fabrication parameters for Ti-6Al-4V samples by SLM.

Area	Power (W)	Scanning speed (mm/s)	Layer thickness (μm)	Hatching distance (mm)
Inside	200	900	30	0.12
Support	150	1100	30	0.12

Reference: Own authorship (2018).

Applying Table 36 parameters, auxetic SLM Ti-6Al-4V samples were built (Figure 89). In this stage, with the end of fabrication and the removal of excessive powder, Ti-6Al-4V samples are still attached to the building plate and have their support structures.

Figure 89 – SLM Ti-6Al-4V samples fixed on the building plate.



Reference: Own authorship (2018).

In the following step, the structures were retrieved from the building plate by means of an AgieCharmilles CUT 20P Wire Electrical Discharge Machining (WEDM) equipment (Figure 90). This equipment uses an electrified wire immersed in a dielectric to cut a variety of metals (steels, copper, aluminum and their alloys), carbides and graphite, including high thickness bars – up to 250 mm in this model - with high precision and good final surface finishing. Optimal fine surface roughness (R_a) values of $0.25 \mu\text{m}$ can be achieved and, in most common situations, $R_a = 0.60 \mu\text{m}$ (AGIECHARMILLES, 2009).

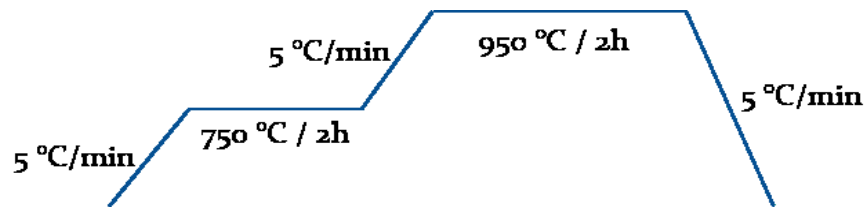
Figure 90 –AgieCharmilles CUT 20 P WEDM equipment.



Reference: (AGIECHARMILLES, 2008).

After WEDM cutting, auxetic parts were separated from the building plate and were heat treated in Argon inert atmosphere (Pressure around 10^{-5} Torr), following parameters presented in Figure 91. This heat treatment is intended to relieve thermal stresses produced during SLM processing, successive heat and cooling cycles occurs as parts of the powder pool are melted. Also, this procedure is critical to eliminate support structures, as they become more fragile and brittle, facilitating its removal. This post-process step was performed at Bodycote, Czech Republic.

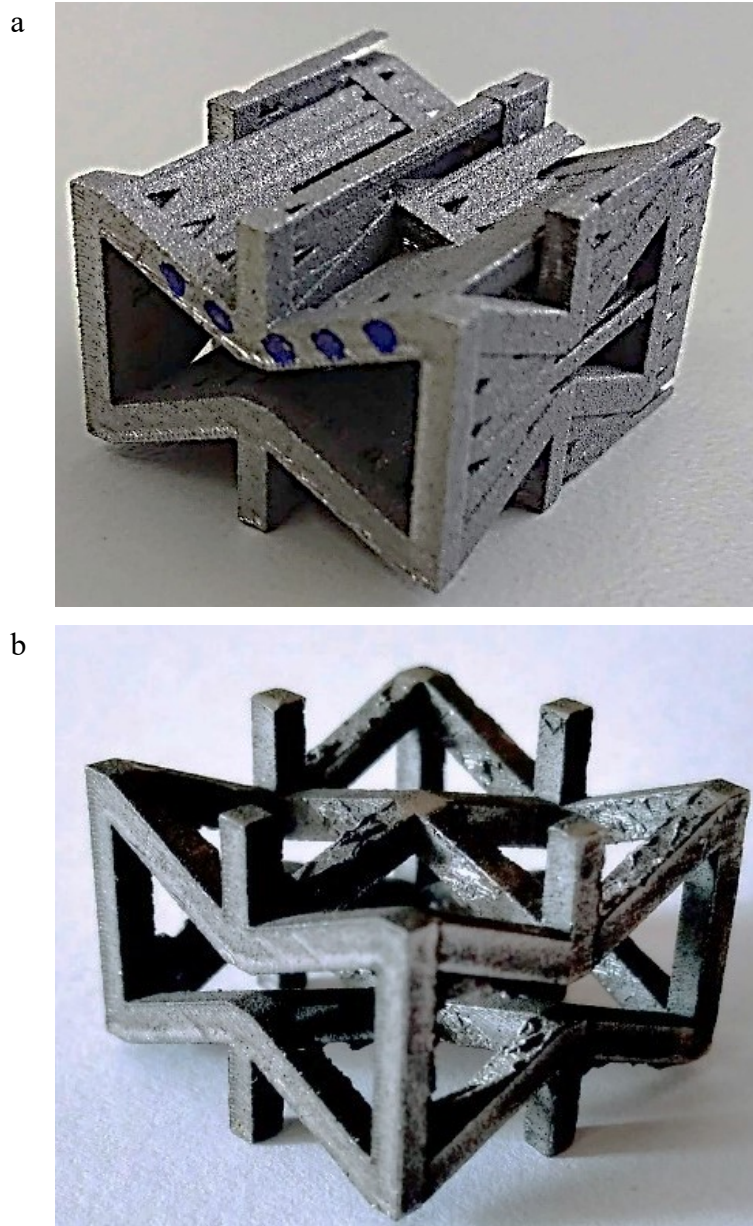
Figure 91 – Details of heat treatment under argon atmosphere of Ti-6Al-4V auxetic samples.



Reference: Own authorship (2018).

Figure 92(a) presents a STR3 sample before heat treatment, containing support structures. After being submitted to the heat treatment described in Figure 91, STR3 support structures were removed and polishing was applied to eliminate traces of this sustentation system (Figure 92(b)).

Figure 92 - Ti-6Al-4V STR3 auxetic samples: (a) STR3 sample with support structure, before heat treatment; (b) STR3 sample without support structure, after heat treatment described in Figure 91.



Reference: Own authorship (2018).

5.2.4.1 Porosity of Ti-6Al-4V samples

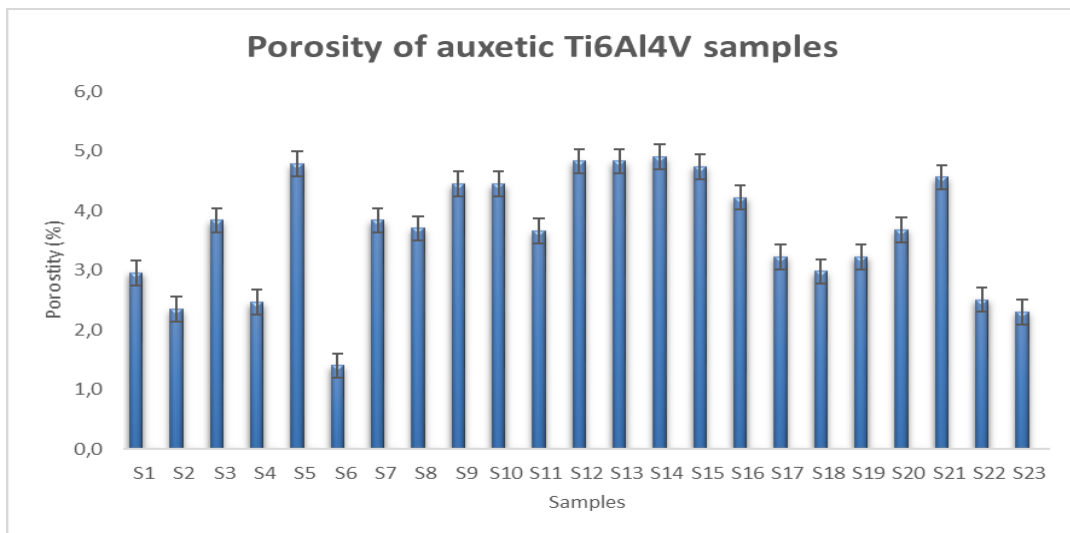
In the following, porosity of auxetic Ti-6Al-4V samples was measured using the Archimedes method (adapted balance model Mettler Toledo New Classic MS with Draftshield). Figure 57(c) represents the schematics of this balance.

Coupled to Mettler Toledo balance there are a thermometer and two smaller balances: one in air; another inside a beaker filled with deionized water. The first measures weight in air, as the latter measures the corresponding weight in liquid.

First, machine calibration was performed, then, sample's weight in air was measured. Then, sample's weight in water was obtained and density was calculated. Average porosity and the respective standard deviation were obtained: $3.647 \pm 0.976\%$. As previously verified in the state of the art (Section 2), SLM method is able to create parts with very high densification, in the case of STR3 samples, a minimum value for densification was a maximum of 98.6% was attained, which is similar to values obtained using island scan strategies (VALENTE, 2019). Complementary data concerning porosity of all samples are summarized in the annex section – Table 40.

Figure 93 presents the statistical distribution of measured porosity in auxetic Ti-6Al-4V samples obtained by Archimedes method: porosity values were found between and 1.40 and 4.989 %, with strong oscillations. Despite the simple setup and fast measurement, this method presents a series of limitations as it demands a constant calibration and constant room temperatures, which can have influence on the experimental results.

Figure 93: Distribution of measured porosity of Ti-6Al-4V samples.



Reference: Own authorship (2018).

5.2.4.2 Mechanical tests of Ti-6Al-4V samples

Static tests

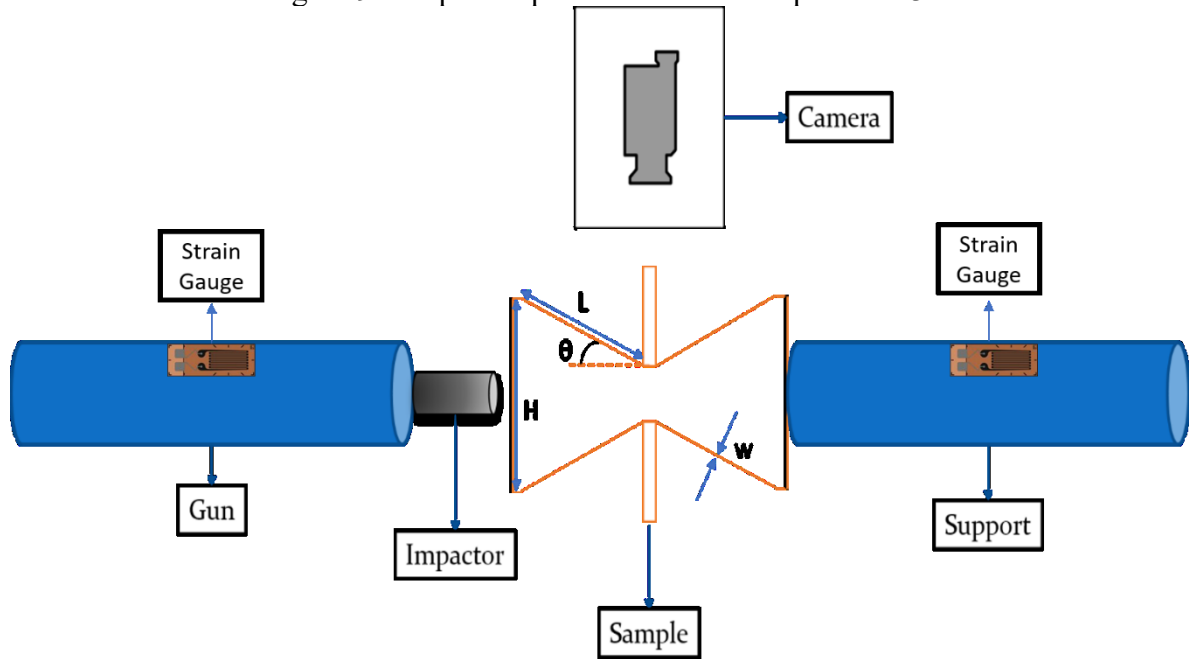
The purpose of testing auxetic STR3 samples in static regime is to establish its main mechanical properties such as Poisson ratio, Young modulus, tensile strength, and, stress-deformation curve.

In this step, the measurement of Poisson coefficient is the stronger priority. As such, a specific experiment setup was employed: two laser vibrometers were coupled to a Universal testing machine. After long calibration, laser vibrometers were set to follow the deformation of the structure in quasi-static regime.

Split-Hopkinson bar test: dynamic behavior of auxetic samples

This compressive test consists in the impact of a sample by a striker moving at constant speed (Figure 94). Typically, the striker can be made of several materials: aluminum alloys, steels, nylon, polyester, wood. As the sample is hit, a high-speed camera (typically 10^4 fps) captures the motion of the sample and, by Digital Image Correlation (DIC) method, the corresponding deformations can be measured. Moreover, this test allows the determination of amplitudes of the elastic wave pulse (incident, transmitted and reflected); as well as the dynamic stress-strain response of materials and other dynamic properties.

Figure 94 – Split-Hopkinson bar test setup of STR3.



Reference: Own authorship (2018).

This test requires a long planning and rigorous calibration to provide reproducible results. Besides, as the experiment is held in a dark room, one face of the STR3 samples is marked to obtain more contrast and, then, measure the motion of the auxetic structure. In this experiment a set of two steel bars (dimensions: 15 x 1100 mm) and a steel striker (dimensions: 14 x 33 mm) were used.

Figure 95 presents three different steps of Hopkinson bar test – before impact (a), impact (b), and, relaxation (c). After impact, a slight deformation is observed (in fact, as the test result is composed by a succession of frames, deformation is more visible in the motion picture). Moreover, because of the high surface rugosity, contrast points in the sample were not sufficient. In this sense, deformation measurements obtained by DIC were not representative, which implies in the need of a major revision and new experiments.

Figure 95 – Split-Hopkinson bar test of STR3.



Reference: Own authorship (2018).

5.3 BUILDING HIGH ENERGY IMPACT RESISTANT ARMOR MODELS

The state of art in ballistic armor indicates that for intermediary ballistic protection, a common model, for higher caliber protection, is the one composed by a thin Kevlar® (registered trademark of DuPont) layer, followed by a ceramic plate (SiC, TiC, B₄C), a polymer gel and as final layer a ceramic plate (equal to the first plate). This model is illustrated in Figure 96 (BAE SYSTEMS, 2018).

Figure 96 – Armor plates from ballistic vests.



Reference: (BAE SYSTEMS, 2018).

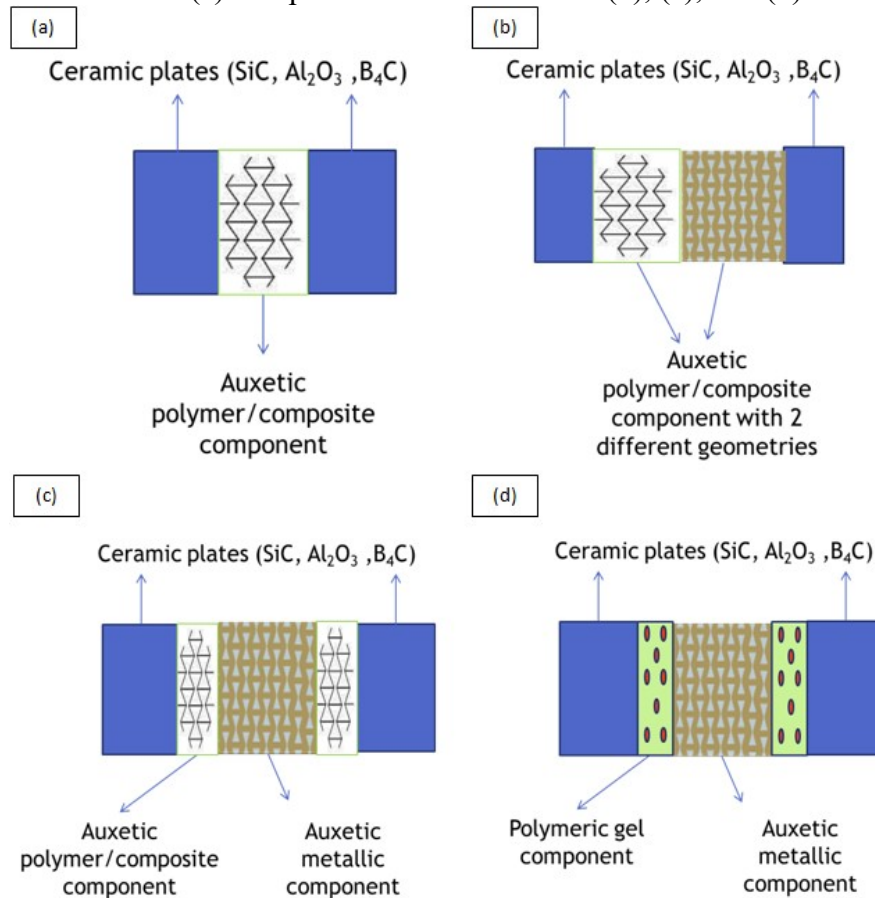
Besides, this armor protection system is able to endure in severe environment conditions (high altitudes, temperatures and humidity), and, also in extreme conditions such

as direct flame exposure, intense vibration and exposition to chemicals. Comfort and versatility are also considered with the application of multi-curved geometries and different plate sizes (SYSTEMS, 2018).

Based on this ballistic model and results of this study, several armor models are proposed and optimized (initially through simulation). Figure 97 a - d illustrates all features of those structures:

- a. Hard Ceramic layer + thin Polyvinylbutiral (PVB) interlayer + auxetic polymer/composite component + thin PVB layer + hard ceramic layer.
- b. Hard Ceramic layer + thin PVB interlayer + 2 different auxetic polymer/composite components with same dimensions + thin PVB layer + hard ceramic layer.
- c. Hard ceramic layer + thin PVB interlayer + auxetic polymer/composite/metal components with variable dimensions + thin PVB layer + hard ceramic layer.
- d. Hard ceramic layer + thin PVB interlayer + auxetic metallic component + polymeric gel + thin PVB interlayer + hard ceramic layer

Figure 97 – Armor systems using ceramic plates and polymer auxetic structures (a)/composite auxetic structures (b), (c), and (d).



Reference: Own authorship (2018).

Each layer accomplishes a specific function: the first ceramic plate (high hardness and increased compression resistance) significantly reduces the speed of the projectile or can also destroy/deflect the projectile; the polymeric PVB interlayers ensures support to the ceramic plate, strong binding to the auxetic component and also decreases the projectile's kinetic energy in case of the ceramic plate is penetrated.

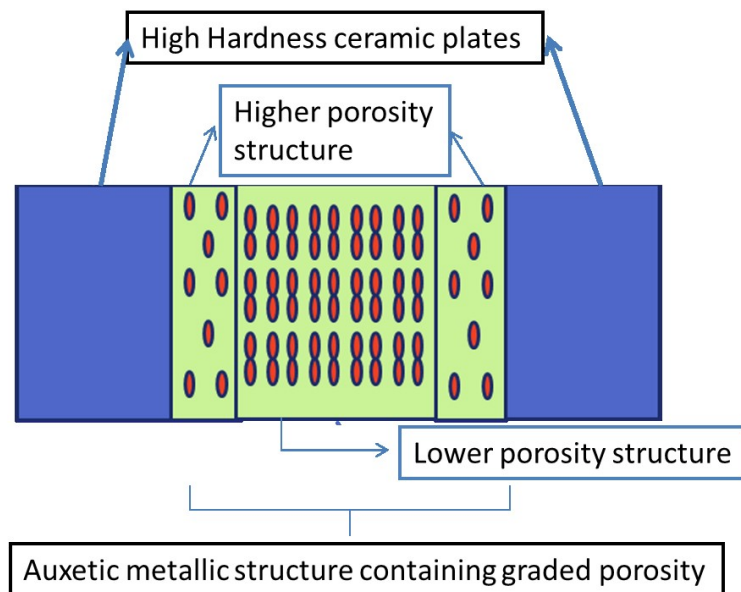
Even tough, in extreme cases, projectile kinetic can significantly damage armor systems. In this sense, armor model (d) (Figure 97(d)) presents an innovative feature: if the hard-ceramic plate and the auxetic metallic component fail, a viscous polymeric gel can still provide flexibility and functionality of the armor part by offering a more resistive media for the projectile propagation.

As an alternative to polymer gel formulations, shear thickening/magnetorheological fluids (STF) have a Non-Newtonian behavior: as the pressure is low, their characteristics are similar to common liquids; in the other hand, with higher pressure or increased magnetic field, STF have a solid-like response (PATEL, 2020). Compared to Kevlar bulletproof vests, STF-filled armor presents lower mass and a minor rebound after impact, which enhances system reliability and user safety (TOP WAR, 2015).

Models listed in Figure 97 have as main objective the enhancement of armor effectiveness: by including an auxetic structure, the armor structure will have greater compression resistance. Further understanding of the dynamic deformation behavior is required, especially in the ballistic test of the composite structure. For this purpose, simulation will be performed using ANSYS software.

Moreover, since SLM brings a great flexibility to create parts with complex geometries, an auxetic component with graded porosity is quite relevant: a single auxetic metallic layer would reduce the problem of coupling between different layers – especially between auxetic components of different compositions (polymer/composite with metallic materials). This model is illustrated in Figure 98.

Figure 98 – Auxetic armor model containing an auxetic metallic component with graded porosity (red circles).



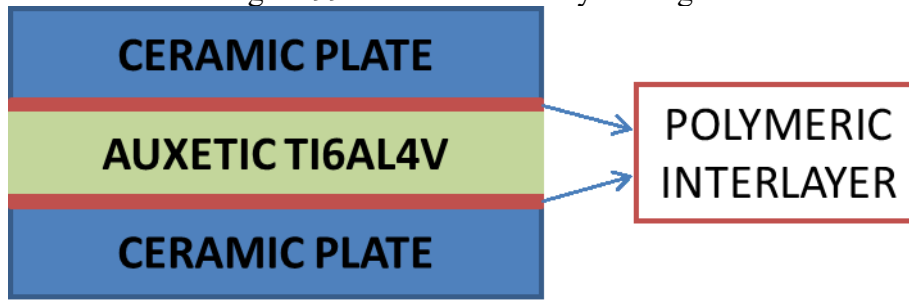
Reference: Own authorship (2018).

Greater porosity structures are placed near to the hard ceramic plate: in this area, more flexibility is required from the auxetic component (a greater deformation and energy absorption capacity is necessary), and, consequently, the hard ceramic have more significant resistance to the projectile impact. Besides, in a central region of the auxetic component, porosity will be reduced to increase compression resistance and armor integrity. Nevertheless, this area must display some capability of deformation. A compromise between compression resistance and flexibility has to be determined in the whole auxetic component.

By using standard dimensions for the ceramic plates and the auxetic component (which will be optimized by simulation), the models proposed in Figure 97 and 98 will be tested in a FEM ballistic test, similar as NATO standards for this level of armor protection.

Prototypes will be produced based in the most efficient design, combination of materials and ballistic performance. Furthermore, the armor will be assembled in a multilayer sandwich design as shown on Figure 99.

Figure 99 – Auxetic multilayer design.



Reference: Own authorship (2018).

In order to perform the union between the ceramic plates and the auxetic metallic structure, several adhesive materials are available: prepreg resin mixed with fibers, such as Kevlar (e.g., a mix composed of PVB phenolic resin and Kevlar fibers); PVB layers combined with resin to ensure a minimal rigidity (CHEESEMAN, 2003).

A polymer layer is an affordable alternative to link ceramic and metallic parts. As a complementary approach, a metallization of the ceramic plate surface can create a strong bond to the auxetic metallic part. Still, this procedure can increase fabrication time and final cost of the composite.

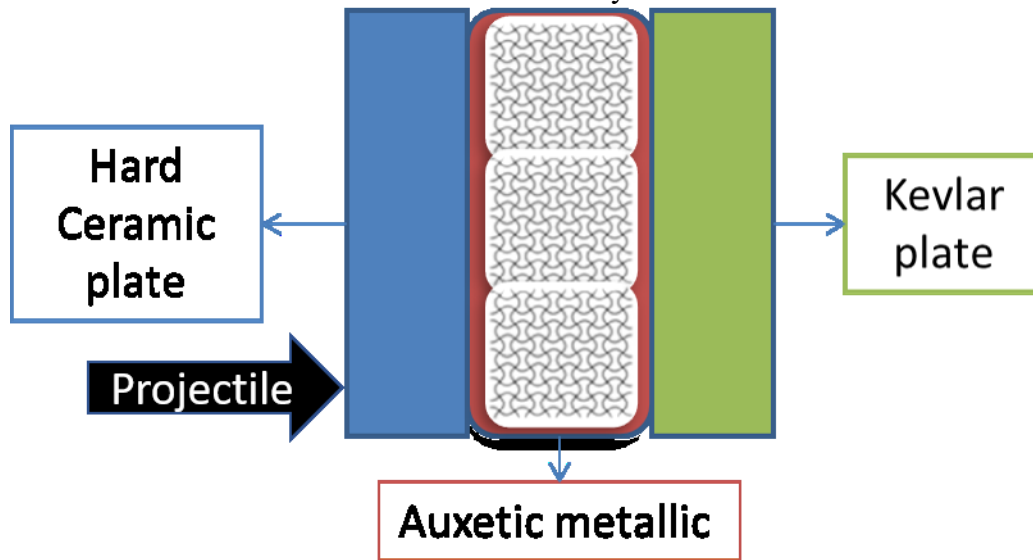
Regarding the formation of the sandwich structure, a protocol is proposed:

- (0) Test stability of the adhesive material (chemical and thermal).
- (1) Apply 1 mm layer of prepreg resin/PVB in the ceramic plate.
- (2) Heat the ceramic plate for 10 minutes at 120 °C to leave humidity and allow the resin/PVB to cure. In this sense, UV light has to be applied, to ensure resin cure.
- (3) Bond the auxetic metallic structure to the ceramic plates containing resin.
- (4) Pressing of the composite (auxetic structure + polymeric interlayers + ceramic plates) to strengthen the bond between layers. Ideal time and temperature of process has to be determined.

Figure 100 presents another alternative to counter weight limitations: instead of using two hard ceramic plates, a thin Kevlar layer enters the composition, ensuring more flexibility to mold surfaces such as the human body. In this case, the auxetic structure works as a damper to attenuate shock waves resulting from the projectile impact. To assure cohesion of this armor system, a thin elastomer layer is spread on the surface of the auxetic metallic structure, creating a strong bond between, the front hard ceramic plate and the Kevlar plate.

Further research and simulation will determine the ideal width of each layer and the most appropriate elastomer, according to the application.

Figure 100 – Composite armor including hard ceramic plate, auxetic metallic interlayer and a thin Kevlar layer.



Reference: Own authorship (2018).

6 CONCLUSIONS

SLM, which figures as one of the most remarkable AM techniques, has the potential to create complex forms from raw metallic powder. This so-called 4th Industrial revolution, in which machines are integrated through intelligent networks, bring a new perspective for fabrication. From now on, areas such as prototype development can be significantly enhanced both regarding time and mechanical properties by using AM.

In the other hand, auxetic structures, which have been more intensively studied from 1980 on, have remarkable features such as improved resistance to indentation. Until recent times, polymeric foams such as Polyurethane (PU) were the main object of study in auxetic structures. However, with growing advances in AM, especially regarding metal fabrication, metallic auxetic structures (Ti and Ti-6Al-4V, AlSi₁₀Mg, Inconel, steels) are quickly produced with high precision and tunable properties. In this sense, auxetic structures gain more leverage and novel applications are conceivable, such as armor protection.

SS-316L and Ti-6Al-4V complex auxetic structures were obtained using SLM, with remarkable densification around 96% (average value). Nevertheless, for both materials, significant surface rugosity was observed, which created problems in deformation measurements by DIC and laser vibrometers.

Static compression tests performed in SS-316L samples P_i proved that these structures can absorb significant quantity of energy, even after suffering plastic deformation in several regions. In one particular case, the compression test of P₁, maximal machine loading limit was applied, resulting in a significant shrinking, whilst this structure still presented mechanical integrity.

ANSYS 19 simulations of auxetic Ti-6Al-4V STR3 presented promising results: a minimum value of $\nu = -5.75$ can be easily obtained by setting $H/L = 2.5$ and $W = 1$ mm, for $\theta = 12^\circ$. Moreover, from our ballistic impact simulations, STR3 was able to fully absorb the energy of a 7.62 mm projectile travelling at a maximal speed of 400 m/s. After this limit, STR3 suffers severe plastic deformation and mechanical integrity is compromised.

Therefore, the hypothesis formulated in the Introduction (section 1) has been confirmed: auxetic structures can be optimized and geometric parameters have a strong influence on NPR.

As previously mentioned, the mechanical testing process took place mostly through numerical simulations, producing results that contributed to the demonstration that the STR3 structure has auxetic properties and great potential for ballistic applications.

In general, experiment work is highly demanding in time and resources – especially in SLM fabrication – which becomes a major challenge to the research task. Limitations of time and budget had little influence in the results of this research, still, part of the mechanical characterization suffered delays. During the development of this investigation, a decision was made to perform an extensive work at IT-CAS, a center of excellence in research with strong international presence. This institution gathered several resources such as Split Hopkinson bar test; static tests with vibrometers; FEM expertise; fundamentals on ballistic impact and plasticity, which implied in a crucial time optimization for this research.

This research represents a contribution for a very promising topic, both regarding technology and innovation. Several applications can be developed, especially to solve practical problems in ballistic applications.

7 FUTURE WORK

The continuation of this research will follow in different fronts: new auxetic geometries; advanced simulations to verify the properties of these new structures; further optimization of auxetic structures; more static and dynamic tests, especially regarding high cycle fatigue and Taylor gun tests. Furthermore, new Ti-6Al-4V auxetic structures optimized via simulation and experiments will be produced using SLM. Process parameters will be reviewed aiming to improve mechanical performance for ballistic applications.

Extensive simulation of armor models described in Figure 90 is also considered. According to results and capabilities of each design, prototypes will be produced, and, further on, tested in a standardized ballistic experiment.

From the network created in the PhD period, international cooperation will be strengthened to bring fruitful results for the scientific community.

8 ANNEX

Table 37 – Porosity of auxetic Ti-6Al-4V samples measured by Archimedes method.

Sample	Measured density ρ (g/cc)	Sample porosity P (%)	Main parameters
S1	4,299	2,957	Machine error (g)
S2	4,326	2,348	$\pm 0,001$
S3	4,260	3,837	Temp. (°C)
S4	4,321	2,460	23,6
S5	4,218	4,786	Average density $\langle\rho\rangle$ (g/cc)
S6	4,368	1,400	4,268
S7	4,26	3,837	$\rho_{\text{Ti-6Al-4V}}$ (g/cc)
S8	4,266	3,702	4,430
S9	4,233	4,447	Standard Deviation (%)
S10	4,233	4,447	0,976
S11	4,268	3,657	Average sample Porosity $\langle P \rangle$ (%)
S12	4,216	4,831	3,647
S13	4,216	4,831	
S14	4,213	4,898	
S15	4,220	4,740	
S16	4,243	4,221	
S17	4,287	3,228	
S18	4,298	2,980	
S19	4,287	3,228	
S20	4,267	3,679	
S21	4,228	4,560	
S22	4,319	2,506	
S23	4,328	2,302	

Reference: Own authorship (2018).

9 REFERENCES

ABA-PEREA, P. E.; PIRLING, T.; PREUSS, M. In-situ residual stress analysis during annealing treatments using neutron diffraction in combination with a novel furnace design. **Materials & Design**, v. 110, n., p. 925-931, 2016.

ACEVEDO, R. SEDLAK, P. KOLMAN, R. FREDEL, M. Residual stress analysis of Additive Manufacturing of Metallic Parts using Ultrasonic Waves: State of the art review, **Journal of Materials Research and Technology**, v. 9, n.4, 2020.

AGIECHARMILLES. **Technical Data CUT 20/30**: secondary title, 2008.

AGIECHARMILLES. **Brochure Wire Cut EDM CUT 20P/30P**: secondary title, 2009.

AGRIPA, H. BOTEF, I. Modern production methods for titanium alloys: a review. **Titanium alloys – novel aspects of their manufacturing and processing**, IntechOpen 2019

AHERWAR, A. SINGH, T. SINGH, A. PATNAIK, A. FEKETE, G. Optimum selection of novel developed implant material using hybrid entropy-PROMETHEE approach. **Materialwissenschaft und Werkstofftechnik**, v. 50, n. 10, p. 1232-1241, 2019.

ALDERSON, A. A triumph of lateral thought. **Chemistry & Industry**, v., n. 10, p. 384-391, 1999.

ALI, H. MA, L. GHADBEIGI, H. MUMTAZ, K. In-situ residual stress reduction, martensitic decomposition and mechanical properties enhancement through high temperature powder bed pre-heating of Selective Laser Melted Ti-6Al-4V. **Materials Science and Engineering a-Structural Materials Properties Microstructure and Processing**, v. 695, n., p. 211-220, 2017.

ARCE, A. N. Thermal modeling and simulation of electron beam melting for rapid prototyping on Ti-6Al-4V alloys. **North Carolina State University**, Raleigh, 2012.

ASTM E9-19. Standard Test Methods of Compression Testing of Metallic Materials at Room Temperature, **ASTM International**, 2019.

BAKER, C. **Auxetic spinal implants: consideration of negative Poisson's ratio in the design of an artificial intervertebral disc**. University of Toledo, 2011.

BALDI, A. Residual Stress Measurement Using Hole Drilling and Integrated Digital Image Correlation Techniques. **Experimental Mechanics**, v. 54, n. 3, p. 379-391, 2014.

BANERJEE, S. MUKHOPADHYAY, P. **Phase Transformations: Examples from Titanium and Zirconium Alloys**: Elsevier Science, v.12, 2007.

BAUGHMAN, R. H. SHACKLETTE, J. M. ZAKHIDOV, A. A. STAFSTROM, S. Negative Poisson's ratios as a common feature of cubic metals. **Nature**, v. 392, n. 6674, p. 362-365, 1998.

BOAKYE, A. CHANG, Y. RAJI, R.K. MA, P. A review on auxetic textile structures, their mechanism and properties. **Journal of Textile Science & Fashion Technology**, v. 2, n. 1, 2019.

BOONE, N. ZHU, C. SMITH, C.; TODD, I. WILLMOTT, J. R. Thermal near infrared monitoring system for electron beam melting with emissivity tracking. **Additive Manufacturing**, v. 22, n., p. 601-605, 2018.

BRANS, J. P. VINCKE, P. MARESCHAL, B. How to select and how to rank projects - the promethee method. **European Journal of Operational Research**, v. 24, n. 2, p. 228-238, 1986.

BREMEN, S. MEINERS, W. DIATLOV, A. Selective Laser Melting. **Laser Technik Journal**, v. 9, n. 2, p. 33-38, 2012.

BUCHBINDER, D.; SCHLEIFENBAUM, H. HEIDRICH, S. MEINERS, W. BULTMANN, J. High Power Selective Laser Melting (HP SLM) of Aluminum Parts. In: Schmidt, M., Zaeh, M., *et al* (Ed.). **Lasers in Manufacturing 2011: Proceedings of the Sixth International WIT Conference on Lasers in Manufacturing** (Physics Procedia), v.12, Pt A, p.271-278, 2011.

BUCHBINDER, D. MEINERS, W. PIRCH, N. WISSENBACH, K. SCHRAGE, J. Investigation on reducing distortion by preheating during manufacture of aluminum components using selective laser melting. **Journal of Laser Applications**, v. 26, n. 1, p., 2014.

CAMARGO, E. **Conheça os principais softwares de simulação e suas aplicações**: secondary title, 2012.

CARLSSON, S. LARSSON, P. L. On the determination of residual stress and strain fields by sharp indentation testing. Part I: Theoretical and numerical analysis. **Acta Materialia**, v. 49, n. 12, p. 2179-2191, 2001.

CARLSSON, S. LARSSON, P. L. On the determination of residual stress and strain fields by sharp indentation testing. Part II: Experimental investigation. **Acta Materialia**, v. 49, n. 12, p. 2193-2203, 2001.

CARNEIRO, V. H. MEIRELES, J. PUGA, H. Auxetic materials — A review. **Materials Science-Poland**, v. 31, n. 4, p. 561 – 571, 2013

CARNEIRO, V.H. CAPELA, P. TEIXEIRA, J.C. TEIXEIRA, S. CERQUEIRA, F. MACEDO, F. RIBAS, L. SOARES, D. Influence of copper layer content in the elastic and damping behavior of glass-fiber/Epoxy-Resin Composites. **Applied Composite Materials**, n. 23, p. 1219 – 1228, 2016.

CERNIGLIA, D. SCAFIDI, M. PANTANO, A. LOPATKA, R. **Laser ultrasonic technique for laser powder deposition inspection**: secondary title. Le Mans, France, 2013.

CERNIGLIA, D. SCAFIDI, M. PANTANO, A. RUDLIN, J. Inspection of additive-manufactured layered components. **Ultrasonics**, v. 62, n., p., 2015.

CHEESEMAN, B. A.; BOGETTI, T. A. Ballistic impact into fabric and compliant composite laminates. **Composite Structures**, v. 61, n. 1, p. 161-173, 2003.

COLMENERO, F. TIMON, V. Extreme negative mechanical phenomena in the zinc and cadmium anhydrous metal oxalates and lead oxalate dihydrate. **Journal of Materials Science**, n. 55, pp. 218-236, 2020.

CONTROLLASER. Buyer's Guide: Understanding Laser Machines, 2020. URL: <https://www.controllaser.com/blog/2018/11/22/how-can-i-select-the-right-laser-source-for-my-application/>

CROSS, T.M. HOFFER, K.W. JONES, D.P. KIRSCHNER, P. B. LANGVIN, E. MESCHTER, J.C. Auxetic structures and footwear with soles having auxetic structures. Patent US9402439B2, 2016.

CSIRO. The ankle bone's connected to the... 3D printed titanium implant. CSIROSCOPE, 2014. URL: <https://blog.csiro.au/the-ankle-bones-connected-to-the-3d-printed-titanium-implant/>

CUNNINGHAM, R. NARRA, S. P. OZTURK, T. BEUTH, J. ROLLETT, A. D. Evaluating the Effect of Processing Parameters on Porosity in Electron Beam Melted Ti-6Al-4V via Synchrotron X-ray Microtomography. **The Journal of The Minerals, Metals & Materials Society**, v. 68, n. 3, p. 765-771, 2016.

DAHOTRE, N. B. HARIMKAR, S. **Laser Fabrication and Machining of Materials.**: Springer-Verlag, p. 558, 2008.

DAVIS, J. R. Introduction to Stainless Steels. In: Davis, J. R. (Ed.). **Alloy Digest Sourcebook: Stainless Steels**. United States of America: ASM International, p.584, 2001.

DUCATO, A. FRATINI, L. LA CASCIA, M. MAZZOLA, G. **An Automated Visual Inspection System for the Classification of the Phases of Ti-6Al-4V Titanium Alloy**, p. 362-369, 2013.

EARNSHAW, A. GREENWOOD, N.N. Chemistry of the elements. Butterworth-Heinemann 1997.

EVANS, K. E. NKANSAH, M. A. HUTCHINSON, I. J. Auxetic foams: Modelling negative Poisson's ratios. **Acta Metallurgica et Materialia**, v. 42, n. 4, p. 1289-1294, 1994.

EVANS, K. E. ALDERSON, A. Auxetic materials: Functional materials and structures from lateral thinking! **Advanced Materials**, v. 12, n. 9, p. 617-628, 2000.

FACCHINI, L. MAGALINI, E. ROBOTTI, P. MOLINARI, A.; HOGES, S. WISSENBACH, K. Ductility of a Ti-6Al-4V alloy produced by selective laser melting of prealloyed powders. **Rapid Prototyping Journal**, v. 16, n. 6, p. 450-459, 2010.

FISCHER, P. ROMANO, V. WEBER, H. P. KARAPATIS, N. P. BOILLAT, E. GLARDON, R. Sintering of commercially pure titanium powder with a Nd:YAG laser source. **Acta Materialia**, v. 51, n. 6, p. 1651-1662, 2003.

FLORENCIO, O. CHAVES, J. M. SILVA, P. S. SCHNEIDER, S. G. Estudo do comportamento elástico da liga Ti-13Nb-13Zr submetida a diferentes tratamentos térmicos. **19º Congresso Brasileiro de Engenharia e Ciencia dos Materiais**, 2010.

FRITSCH. Brownian motion, 2020. URL: <https://www.fritsch.pt/medicao-de-particulas/conhecimento-fritsch/brownian-motion/>

GALLITELLI, D. RETRAINT, D. ROUHAUD, E. Comparison between conventional shot peening (SP) and surface mechanical attrition treatment (SMAT) on a Titanium alloy. In: Francois, M., Montay, G., *et al* (Ed.). **Residual Stresses IX** (Advanced Materials Research), v.996, p.964-968, 2014.

GAO, H. DUTTA, R. K. HUIZENGA, R. M. AMIRTHALINGAM, M. HERMANS, M. J. M. BUSLAPS, T. RICHARDSON, I. M. Stress relaxation due to ultrasonic impact treatment on multi-pass welds. **Science and Technology of Welding and Joining**, v. 19, n. 6, p. 505-513, 2014.

GE, Z. HU, H. LIU, Y. A finite element analysis of a 3D auxetic textile structure for composite reinforcement. **Smart Materials and Structures**, v. 22, n. 8, p. 084005, 2013.

GERVASIO, H. DA SILVA, L. S. A probabilistic decision-making approach for the sustainable assessment of infrastructures. **Expert Systems with Applications**, v. 39, n. 8, p. 7121-7131, 2012.

GIBSON, I.; ROSEN, D.; STUCKER, B. **Additive Manufacturing Technologies: 3D Printing, Rapid Prototyping, and Direct Digital Manufacturing**. New York, USA: Springer-Verlag, 2015.

GOKULDOSS, P. K. KOLLA, S. ECKERT, J. Additive Manufacturing Processes: Selective Laser Melting, Electron Beam Melting and Binder Jetting—Selection Guidelines. **Materials**, v. 10, n. 6, 672, 2017.

GREEN, R. E. Ultrasonic measurement of Residual Stress. In: First International Symposium on Ultrasonic Materials Characterization, **National Bureau of Standards Special Publication**, p. 173-177, 1978.

GRIGORIEV, S. N. KOZOCHKIN, M. P. PORVATOV, A. N. VOLOSOVA, M. A. OKUNKOVA, A. A. Electrical discharge machining of ceramic nanocomposites: sublimation phenomena and adaptive control. **Heliyon** V. 5, n. 10., 2019.

GU, D. SHEN, Y. Processing conditions and microstructural features of porous 316L stainless steel components by DMLS. **Applied Surface Science**, v. 255, n. 5, p. 1880-1887, 2008.

GU, D. **Laser Additive Manufacturing of High-Performance Materials**: Springer-Verlag, 2015. 311 p.

GU, D. D. SHEN, Y. F. YANG, J. L. WANG, Y. Effects of processing parameters on direct laser sintering of multicomponent Cu based metal powder. **Materials Science and Technology**, v. 22, n. 12, p. 1449-1455, 2006.

GU, D. D. MEINERS, W. WISSENBAACH, K. POPRAWA, R. Laser additive manufacturing of metallic components: materials, processes and mechanisms. **International Materials Reviews**, v. 57, n. 3, p. 133-164, 2012.

GUO, Y. B. LI, W. JAWAHIR, I. S. Surface integrity characterization and prediction in machining of hardened and difficult-to-machine alloys: A state-of-art research review and analysis. **Machining Science and Technology**, v. 13, n. 4, p. 437-470, 2009.

GUZ', A. N. MAKHORT, F. G. The Physical Fundamentals of the Ultrasonic Nondestructive Stress Analysis of Solids. **International Applied Mechanics**, v. 36, n. 9, p. 1119-1149, 2000.

HAGEDORN, Y. C. BALACHANDRAN, N. MEINERS, W. WISSENBAACH, K. POPRAWA, R. SLM of net-shaped high strength ceramics: New opportunities for producing dental restorations. **22nd Annual International Solid Freeform Fabrication Symposium - An Additive Manufacturing Conference, SFF 2011**, v., n., p. 536-546, 2011.

HALL, J. Textbook of medical physiology. **Elsevier**, p. 957-960, 2011.

HAMPEL, C. A. The Encyclopedia of the Chemical Elements. **Van Nostrand Reinhold Book Corporation**, 1968.

HAN, J. XIE, J. ZHANG, Z. YANG, D. SI, M. XUE, D. Negative Poisson's ratios in few-layer orthorhombic arsenic: First-principles calculations. **Applied Physics Express**, v. 8, n. 4, 2015.

HANAKATA, P. Z. CARVALHO, A. CAMPBELL, D. K. PARK, H. S. Polarization and valley switching in monolayer group-IV monochalcogenides. **Physical Review B**, v. 94, n. 3, 2016.

HANAWA, T. Metal ion release from metal implants. **Materials Science and Engineering: C**, v. 24, n. 6, p. 745-752, 2004.

HANZL, P. ZETEK, M. BAKŠA, T. KROUPA, T. The Influence of Processing Parameters on the Mechanical Properties of SLM Parts. **Procedia Engineering**, v. 100, p. 1405-1413, 2015.

HE, B. WU, W. ZHANG, L. LU, L. YANG, Q. LONG, Q. CHANG, K. Microstructural characteristic and mechanical property of Ti-6Al-4V alloy fabricated by selective laser melting. **Vacuum**, v. 150, n., p. 79-83, 2018.

HIBBELER, R. C. **Mechanics of materials**. United States of America: Pearson Prentice Hall, 2011

HUANG, Q. LIU, X. YANG, X. ZHANG, R. SHEN, Z. FENG, Q. Specific heat treatment of selective laser melted Ti-6Al-4V for biomedical applications. **Frontiers of Materials Science**, v.9, n. 4, p. 373-381, 2015.

ILT, F. Automated support removal for SLM components. **Annual report**, 2016.

IMBALZANO, G. TRAN, P. NGO, T. D. LEE, P. V. S. Three-dimensional modelling of auxetic sandwich panels for localized impact resistance. **Journal of Sandwich Structures & Materials**, v. 19, n. 3, p. 291-316, 2017.

JIANG, J.-W. PARK, H. S. Negative poisson's ratio in single-layer black phosphorus. **Nature Communications**, v. 5, 2014.

JIANG, J.-W. PARK, H. S. Negative Poisson's Ratio in Single-Layer Graphene Ribbons. **Nano Letters**, v. 16, n. 4, p. 2657-2662, 2016.

JIANG, J. XU, X. STINGER, J. Support structures for Additive Manufacturing: a review. **Journal of Manufacturing and Materials Processing, MDPI**, v.2, n. 64, 2018

KALENTICS, N. BOILLAT, E. PEYRE, P. CIRIC-KOSTIC, S. BOGOJEVIC, N. LOGE, R. E. Tailoring residual stress profile of Selective Laser Melted parts by Laser Shock Peening. **Additive Manufacturing**, v. 16, n., p. 90-97, 2017.

KALENTICS, N. BOILLAT, E. PEYRE, P. GORNY, C. KENEL, C. LEINENBACH, C. JHABVALA, J. LOGÉ, R. E. 3D Laser Shock Peening – A new method for the 3D control of residual stresses in Selective Laser Melting. **Materials & Design**, v. 130, n., p. 350-356, 2017.

KELLER, S. CHUPAKHIN, S. STARON, P. MAAWAD, E. KASHAEV, N. KLUSEMANN, B. Experimental and numerical investigation of residual stresses in laser shock peened AA2198. **Journal of Materials Processing Technology**, v. 255, n., p. 294-307, 2018.

KEMPEN, K. VRANCKEN, B. BULS, S. THIJS, L. HUMBEECK, J. KRUTH, J.-P. Selective Laser Melting of Crack-Free High Density M2 High Speed Steel Parts by Baseplate Preheating. **Journal of Manufacturing Science and Engineering**, v. 136, n., p., 2014.

PATEL, S. A. CHHABRA, R. P. Non-Newtonian Fluids. **Kirk Othmer Encyclopedia of Chemical Technology**, Wiley, 2020.

KOU, L. MA, Y. TANG, C. SUN, Z. DU, A. CHEN, C. Auxetic and Ferroelastic Borophane: A Novel 2D Material with Negative Poisson's Ratio and Switchable Dirac Transport Channels. **Nano Letters**, v. 16, n. 12, p. 7910–7914, 2016.

KROMM, A. CABEZA, S. MISHUROVA, T. NADAMMAL, N. THIEDE, T. BRUNO, G. Residual Stresses in Selective Laser Melted Samples of a Nickel Based Superalloy. In: Seefeldt, M. (Ed.). **Residual Stresses 2018** (Materials Research Proceedings), **Ecrs-10**, v.6, p.259-264, 2018.

KRUTH, J.-P. BADROSSAMAY, M. YASA, E. DECKERS, J. THIJIS, L. HUMBEECK, J. Part and material properties in selective laser melting of metals. **16th International Symposium on Electromachining, ISEM 2010**, v., n., p., 2010.

KRUTH, J. P. Lasers and materials in selective laser sintering. **Assembly Automation**, v. 23, n. 4, p. 357-371, 2003.

KUDRYAVTSEV, Y. KLEIMAN, J. **Residual Stress Management: Measurement, Fatigue Analysis and Beneficial Redistribution**: secondary title: Springer, v. 8, p. 119-129, 2011.

LASER, C. **CL 20ES Stainless Steel**: secondary title, 2019.

LASER, C. **CL 20ES Stainless Steel**: secondary title, 2020.

URL: <https://www.ge.com/additive/sites/default/files/2019-11/316L-M2beide.pdf>

LEYENS, C.; PETERS, M. **Titanium and titanium alloys: fundamentals and applications**. Weinheim, Germany: Wiley-VCH, 2003

LI, C. LIU, J. F. GUO, Y. B. Prediction of Residual Stress and Part Distortion in Selective Laser Melting. **Procedia CIRP**, v. 45, n., p. 171-174, 2016.

LI, C. LIU, Z. Y. FANG, X. Y. GUO, Y. B. Residual Stress in Metal Additive Manufacturing. **Procedia CIRP**, v. 71, n., p. 348-353, 2018.

LI, Z. HE, J. TENG, J. WANG, Y. Internal Stress Monitoring of In-Service Structural Steel Members with Ultrasonic Method. **MDPI Materials Journal**, v. 9, n. 4, p. 223, 2016.

LIMITED, E. G. P. **A Focus on SLM and SLS Methods in 3D Printing**: Emerald Group Publishing Limited, 2015

LIU, Y. P. HU, H. A review on auxetic structures and polymeric materials. **Scientific Research and Essays**, v. 5, n. 10, p. 1052-1063, 2010.

LU, Y. J. WU, S. Q. GAN, Y. L. HUANG, T. T. YANG, C. G. LIN, J. J. LIN, J. X. Study on the microstructure, mechanical property and residual stress of SLM Inconel-718 alloy manufactured by differing island scanning strategy. **Optics and Laser Technology**, v. 75, n., p. 197-206, 2015.

MAITY, S. R.; CHAKRABORTY, S. Tool steel material selection using PROMETHEE II method. **International Journal of Advanced Manufacturing Technology**, v. 78, n. 9-12, p. 1537-1547, 2015.

MARDLING, P. ALDERSON, A. MAHY, N.J. LE MAITRE, C.L. The use of auxetic materials in tissue engineering. *Biomaterials Science*, v. 8, pp. 2074-2083, 2020.

MARTINA, F. ROY, M. J. SZOST, B. A. TERZI, S. COLEGROVE, P. A. WILLIAMS, S. W. WITHERS, P. J. MEYER, J. HOFMANN, M. Residual stress of as-deposited and rolled wire plus arc additive manufacturing Ti-6Al-4V components. **Materials Science and Technology**, v. 32, n. 14, p. 1439-1448, 2016.

MARTZ, E.O. LAKES, R.S. GOEL, V.K. PARK, J.B. Designs of an artificial intervertebral disc exhibiting a negative Poisson's ratio. *Cellular polymers*, v.24, n.3, 2005.

MATSUMOTO, Y.; HASHIMOTO, F.; LAHOTI, G. Surface Integrity Generated by Precision Hard Turning. **CIRP Annals**, v. 48, n. 1, p. 59-62, 1999.

MAY, C. A. EPOXY RESINS – CHEMISTRY AND TECHNOLOGY. **Taylor & Francis**, 1988

MEGAHED, M. MINDT, H.-W. N'DRI, N. DUAN, H. DESMAISON, O. Metal additive-manufacturing process and residual stress modeling. **Integrating Materials and Manufacturing Innovation**, v. 5, n. 1, p. 61-93, 2016.

MET, E.M. The DMLS Technology, 2017. URL: http://www.e-manufacturing.it/downloads/e-manufacturing_distinctive_features_MET.pdf

MILEWSKI, J. O. Additive Manufacturing of Metals: From Fundamental Technology to Rocket Nozzles, Medical Implants, and Custom Jewelry: **Springer International Publishing**, 2017 (Springer Series in Materials Science)

MOAT, R. J. PINKERTON, A. J. LI, L. WITHERS, P. J. PREUSS, M. Crystallographic texture and microstructure of pulsed diode laser-deposited Waspaloy. **Acta Materialia**, v. 57, n. 4, p. 1220-1229, 2009.

MOTT, P. H. ROLAND, C. M. Limits to Poisson's ratio in isotropic materials. **Physical Review B**, v. 80, n. 13, p. 132104, 2009.

MOYLAN, S. WHITENTON, E. LANE, B. SLOTWINSKI, J. Infrared Thermography for Laser-Based Powder Bed Fusion Additive Manufacturing Processes. In: Chimenti, D. E., Bond, L. J., *et al* (Ed.). **40th Annual Review of Progress in Quantitative Nondestructive Evaluation: Incorporating the 10th International Conference on Barkhausen Noise and Micromagnetic Testing, Vols 33a & 33b**, v.1581, p.1191-1196, 2014.

NARESH, K. KHAN, K. A. UMER, R. CANTWELL, W. J. The use of X-ray computed tomography for design and process modeling of aerospace composites: A review. **Materials & Design**, v. 190, n. 108553, 2020

NATIONAL HEALTH SYSTEM OF THE UNITED KINGDOM (NHS). How it's performed: Coronary angioplasty and stent insertion. **NHS website**, 2018. URL: <https://www.nhs.uk/conditions/coronary-angioplasty/>

NIEMEYER, T. C. GRANDINI, C. R. PINTO, L. M. C. ANGELO, A. C. D.; SCHNEIDER, S. G. Corrosion behavior of Ti-13Nb-13Zr alloy used as a biomaterial. **Journal of Alloys and Compounds**, v. 476, n. 1-2, p. 172-175, 2009.

NORSK TITANIUM. Advantages of RPD process, **Norsk Titanium website**, 2020. URL: <https://www.norsktitanium.com/advantages>

OYELOLA, O. CRAWFORTH, P. M'SAOUBI, R. CLARE, A. T. On the machinability of directed energy deposited Ti-6Al-4V. **Additive Manufacturing**, v. 19, n., p. 39-50, 2018.

PANICO, M. LANGELLA, C. SANTULLI, C. Development of a Biomedical Neckbrace through Tailoring auxetic shapes. **Italian Journal of Science & Engineering**, v. 1, n. 3, 2017.

PAOLETTI, I. NASTRI, M. Material Balance. **SpringerBriefs in Applied Sciences and Technology**, Springer, 2021.

PARK, H. S. KIM, S. Y. A perspective on auxetic nanomaterials. *Nano Convergence*, v. 4, n. 10, 2017.

PARRY, L. ASHCROFT, I. A. WILDMAN, R. D. Understanding the effect of laser scan strategy on residual stress in selective laser melting through thermo-mechanical simulation. **Additive Manufacturing**, v. 12, n., p. 1-15, 2016.

PORTELLA, Q. CHEMKHI, M. RETRAINT, D. Residual Stresses Analysis in AISI 316L Processed by selective Laser Melting (SLM) Treated by Mechanical Post-Processing Treatments. In: Seefeldt, M. (Ed.). **Residual Stresses 2018** (Materials Research Proceedings), **Ecrs-10**, v.6, p.271-276, 2018.

PROTASOV, C. E. SAFRONOV, V. A. KOTOBAN, D. V. GUSAROV, A. V. Experimental study of residual stresses in metal parts obtained by selective laser melting. In: Schmidt, M., Vollertsen, F., *et al* (Ed.). **Laser Assisted Net Shape Engineering 9 International Conference on Photonic Technologies Proceedings of the Lane 2016** (Physics Procedia), v.83, p.825-832, 2016.

QIN, R. ZHENG, J. ZHU, W. Sign-tunable Poisson's ratio in semi-fluorinated graphene. **Nanoscale**, v. 9, n. 1, p. 128–133, 2017.

RHO, J. Y. ASHMAN, R. B. TURNER, C. H. Young's modulus of trabecular and cortical bone material: Ultrasonic and microtensile measurements. **Journal of Biomechanics**, v. 26, p. 111-119, 1993.

RIEDER, H. DILLHOFER, A. SPIES, M. BAMBERG, J. HESS, T. **Online Monitoring of Additive Manufacturing Processes Using Ultrasound** secondary title. Prague, Czech Republic, 2014.

ROSOBORONEXPORT. AK-15 7.62 Kalashnikov assault rifle, Rosoboronexport website, 2021. URL: <http://roe.ru/catalog/sukhoputnye-vosyka/strelkovoe-oruzhie/avtomaty/ak-15/>

ROSSINI, N.S. DASSISTI, M. BENYOUNIS, K.Y. OLABI, A.G. Methods of measuring residual stresses in components. **Materials and Design**, v. 35, p. 572–588, 2012.

SABATINO, A. Auxetic prosthesis implant. Patent US20140058517A1, 2014.

SCARPA, F. ALDERSON, A. RUZZENE, M. WOJCIECHOWSKI, K. Auxetics in smart systems and structures. *Smart Materials and Structures*, n. 25, 050301, 2016.

SHIOMI, M.; OSAKADA, K. NAKAMURA, K. YAMASHITA, T. ABE, F. Residual stress within metallic model made by selective laser melting process. *Cirp Annals-Manufacturing Technology*, v. 53, n. 1, p. 195-198, 2004.

SKERTCHLY, D.: secondary title. Patent US20110214560A1, 2011.

SLM, S. **SLM 125 HL, Selective Laser Melting Machine**: secondary title, 2018.

SONG, B. DONG, S. ZHANG, B. LIAO, H. CODDET, C. Effects of processing parameters on microstructure and mechanical property of selective laser melted Ti-6Al-4V. *Materials & Design*, v. 35, n., p. 120-125, 2012.

SONG, B. DONG, S. J. LIAO, H. L. CODDET, C. Process parameter selection for selective laser melting of Ti-6Al-4V based on temperature distribution simulation and experimental sintering. *International Journal of Advanced Manufacturing Technology*, v. 61, n. 9-12, p. 967-974, 2012.

SONNTAG, R. REINDERS, J. GIBMEIER, J. KRETZER, J. P. Fatigue Performance of Medical Ti6Al4V Alloy after Mechanical Surface Treatments. *PLOS ONE*, v. 10, n. 3, 2015.

SPEARS, T. G. GOLD, S. In-process sensing in selective laser melting (SLM) additive manufacturing. *Integrating Materials and Manufacturing Innovation*, v. 5, n.2, 2016.

STEEN, W. M. MAZUMDER, J. **Laser Material Processing**: Springer-Verlag, p. 578, 2003.

STEFFENS, F. FANGUEIRO, R. Materiais auxéticos : o efeito do coeficiente de Poisson negativo. *Revista de Design, Inovação e Gestão Estratégica*, v. 3, n. 2, p., 2012.

SYSTEM, A. E. **Grade 2 Titanium**: secondary title, 2018.

SYSTEM, A. E. **Ti-6Al-4V Titanium Alloy**: secondary title, 2018.

SYSTEMS, B. **Hard Body Armor redesign**: secondary title: BAE Systems, 2018.

TANG, Z. T. LIU, Z. Q. WAN, Y. AI, X. **Study on Residual Stresses in Milling Aluminium Alloy 7050-T7451**, 2008. 169-178 p. (Advanced Design and Manufacture to Gain a Competitive Edge: New Manufacturing Techniques and Their Role in Improving Enterprise Performance)

TEKNA. **Ti64-53/20**: secondary title, 2019. URL: <http://www.tekna.com/spherical-powders/ti64-titanium-alloy>

THIJS, L. VERHAEGHE, F. CRAEGHS, T. HUMBEECK, J. V. KRUTH, J.-P. A study of the microstructural evolution during selective laser melting of Ti-6Al-4V. **Acta Materialia**, v. 58, n. 9, p. 3303-3312, 2010.

THOMAS, P. C. **CNC Machining Definition, Processes, Components & Equipment: Understanding CNC Machining**. Thomasnet, 2020.

TOP WAR. Non-Newtonian fluid as armor, *Military review and Technologies*, 2015. URL: <https://en.topwar.ru/73725-nenyutonovskaya-zhidkost-v-kachestve-broni.html>

TORONJO, A. CAMPBELL, D. CARUSO, E. Pattern for an article of footwear. Patent USD780414S1, 2015

TUCK, C. **SLM of Aluminium and Titanium alloys – some lessons learned**: secondary title, 2015.

VALENTE, E. H. GUNDLACH, C. CHRISTIANSEN, T. I SOMERS, M. A. Effect of scanning strategy during selective laser melting on surface topography, porosity and microstructure of additively manufacturef Ti-6Al-4V. **Applied Sciences**, v.9, n. 24, 2019.

VANDENBROUCKE, B. KRUTH, J. P. Selective laser melting of biocompatible metals for rapid manufacturing of medical parts. **Rapid Prototyping Journal**, v. 13, n. 4, p. 196-203, 2007.

VARY, A. Quantitative ultrasonic evaluation of mechanical properties of engineering materials. . In: First International Symposium on Ultrasonic Materials Characterization, **National Bureau of Standards Special Publication**, p. 41-53, 1978.

VTT/NURMI. Component design for Metal AM. **Digital open access repository of VTT**, 2017. URL: <https://www.slideshare.net/ErinKomi/component-design-for-metal-am>

WANG, Y. GARCEA, S. C. WITHERS, P. J. 7.6 Computed Tomography of Composites. **Comprehensive Composite Materials II**, v. 7, p. 101-118, 2018.

WANG, X.-T. WANG, B. LI, X.-W. MA, L. Mechanical properties of 3D re-entrant auxetic cellular structures. **International Journal of Mechanical Sciences**, v. 131-132, n., p. 396-407, 2017.

WIRTH, M. A. ROCKWOOD, C. A. J. Current Concepts Review - Complications of Total Shoulder-Replacement Arthroplasty*. **JBJS**, v. 78, n. 4, p. 603-616, 1996.

WU, A. S. BROWN, D. W. KUMAR, M. GALLEGOS, G. F. KING, W. E. An Experimental Investigation into Additive Manufacturing-Induced Residual Stresses in 316L Stainless Steel. **Metallurgical and Materials Transactions a-Physical Metallurgy and Materials Science**, v. 45A, n. 13, p. 6260-6270, 2014.

3DERS. **EOS and Airbus team on aerospace sustainability study for industrial 3D printing**: secondary title, 2014. URL: www.3ders.org

XU, Y. LU, Y. SUNDBERG, K. L. LIANG, J. SISSON, R. D. Effect of Annealing Treatments on the Microstructure, Mechanical Properties and Corrosion Behavior of Direct Metal Laser Sintered Ti-6Al-4V. **Journal of Materials Engineering and Performance**, v. 26, n.6, p. 2572–2582, 2017.

YADROITSEV, I. BERTRAND, P. SMUROV, I. Parametric analysis of the selective laser melting process. **Applied Surface Science**, v. 253, n. 19, p. 8064-8069, 2007.

YAMAGUCHI, H. FERGANI, O. WU, P. Y. Modification using magnetic field-assisted finishing of the surface roughness and residual stress of additively manufactured components. **Cirp Annals-Manufacturing Technology**, v. 66, n. 1, p. 305-308, 2017.

YANG, L. HARRYSSON, O. WEST, H. CORMIER, D. Design and characterization of orthotropic re-entrant auxetic structures made via EBM using Ti-6Al-4V and pure copper. **22nd Annual International Solid Freeform Fabrication Symposium - An Additive Manufacturing Conference, SFF 2011**, v., n., p. 464-474, 2011.

YANG, L. HARRYSSON, O. WEST, H. CORMIER, D. Compressive properties of Ti-6Al-4V auxetic mesh structures made by electron beam melting. **Acta Materialia**, v. 60, n. 8, p. 3370-3379, 2012.

YAP, C. Y. CHUA, C. DONG, Z. LIU, Z. ZHANG, D. LOH, L. E. SING, S. L. Review of selective laser melting: Materials and applications. **Applied Physics Reviews**, v. 2, n., p. 041101, 2015.

YU, L. YAN, Q. RUZSINSZKY, A. Negative Poisson's ratio in 1T-type crystalline two-dimensional transition metal dichalcogenides. **Nature Communications**, v. 8, 15224, 2017.

ZHOU, H. PICKETT, J. MINUT, A. Laser-induced temperature rise in a composite sandwich structure. **Journal of Mathematics and Computer Science**, v. 3, n. 2, p. 577-593, 2013.

ZHU, Z. XU, L. CHEN, G.; LI, Y. Optimization on tribological properties of aramid fibre and CaSO₄ whisker reinforced non-metallic friction material with analytic hierarchy process and preference ranking organization method for enrichment evaluations. **Materials & Design**, v. 31, n. 1, p. 551-555, 2010.

10. APPENDIX – SCIENTIFIC PRODUCTION IN PhD PERIOD (2015-2020)

1. 2017

Participation in the writing of scientific project UNIVERSAL-CNPq (number 282018), entitled:

AUXETicVAI 3D: AUXETIC COMPONENTS FOR HIGH ENERGY IMPACT ABSORPTION FABRICATED BY SLM

Abstract

Brazil has a long tradition in the defense industry, being the largest arms producer in Latin America and the 4th largest arms exporter in the world. The proposal strengthens innovation in a highly competitive and rapidly expanding sector. When conventional manufacturing methods are applied to obtain complex components, some restrictions are observed, such as high cost and the need for multiple processing steps. SLM is a flexible method due to the fact that a finished part can be obtained after a single process step, in addition to the possibility of customizing components according to different design requests, which shows the relevance of the technique. Therefore, for the manufacture of ballistic protection devices with auxetic materials via SLM it is necessary to develop all the expertise of this technology, which includes the study of existing auxetic materials and hard ceramic plates, manufacturing tests and mechanical and physical properties -chemical. Thus, a multidisciplinary group of institutions, under the leadership of UFSC, was organized to understand everything from the characterization of the particulate material, the manufacture of the specimens, to the final mechanical tests and thus obtain the mastery of the production chain of the auxetic components.

2. 2018

Oral presentation at the 2nd International Conference on Advanced Modelling of Wave Propagation in Solids: “Behavior of Ti-6Al-4V Auxetic honeycomb structure under dynamic loading”. Held at the J. Heyrovský Institute of Physical Chemistry of the Czech Academy of Sciences, Prague, Czech Republic.

BEHAVIOUR OF Ti-6Al-4V AUXETIC HONEYCOMB STRUCTURES UNDER IMPACT LOADING

R. Acevedo^{1,2*}, R. Kolman¹, J. Trnka¹

¹Institute of Thermomechanics, AS CR, vvi, Prague, Czech Republic

²Department of Mechanical Engineering, UFSC, Brazil

Typically, most of the materials have a Poisson's coefficient between 0.2 and 0.4. Poisson's coefficient is a non-dimensional ratio defined as the fraction between longitudinal elongation and lateral compression after a uniaxial traction effort. Equation 1 defines this relation:

$$\nu = -\frac{\varepsilon_{transverse}}{\varepsilon_{axial}} \quad (1)$$

This coefficient allows the characterization of matter contraction perpendicular to the applied effort direction [1]. Considering only isotropic materials, the values for this elastic constant are comprised in the $[-1, 0.5]$ interval. The maximum value of ν is 0.5 and it corresponds to the case of an incompressible material (natural rubber) while that the case $\nu = 0$ corresponds to a very little or zero lateral expansion after a compression effort, as it is observed for cork.

Nevertheless, there is a class of materials which present a negative Poisson ratio, those are called auxetic (first introduced by Evans), derived from the Greek word *auxetikos*, defined as "that which tends to increase" [2]. Auxetic behavior can be either intrinsic or obtained by several re-entrant geometries, as shown in Fig. 1 [2]. These geometries can also be extended in 3D.

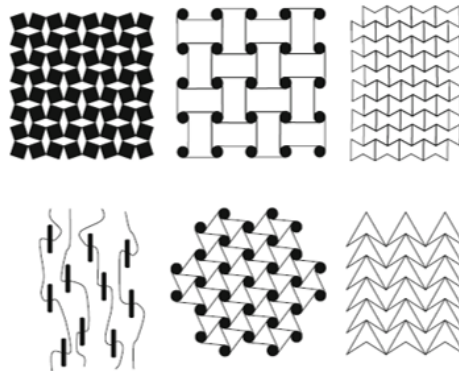


Figure 3: Geometries which show auxetic behaviour [2].

In this study, the following auxetic geometry was chosen (Fig.2), especially due to its easiness in parametrization and promising early simulation results. Elastic behaviour of this structure has been studied in [3,4].

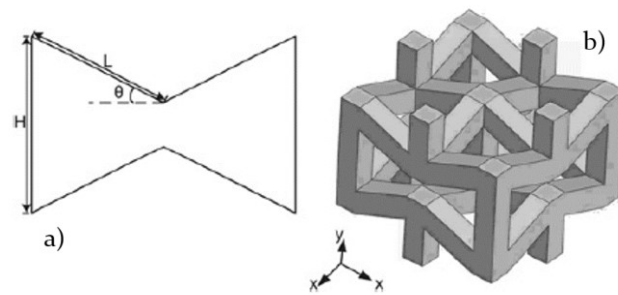


Figure 4: Auxetic geometry a) 2D detail and parameters; b) 3D rendering [3].

In this contribution, the behavior of Ti-6Al-4V auxetic structures and bulk cylinders under impact loading was studied. Using a destructive test approach (DT), these structures were impacted by a loader launched at a given height. Then, the structure response was analyzed by both a laser vibrometer and a high-speed camera system. The deformation of the structures was measured and, the corresponding energy absorption in elasto-plastic regime. Besides, this experiment will allow to access the dynamic deformation behavior of the structure under impact loading of both auxetic and bulk cylinder Ti-6Al-4V specimens.

Besides, a numerical model of the specimens will be performed using FEM method, especially with LS DYNA. Finally, agreement of experimental data and simulation data will be observed.

Keywords: Titanium alloy, Selective Laser Melting, auxetics, wave propagation, NDT.

References

1. Mott, P.H., Roland, C.M. Limits to Poisson's ratio in isotropic materials. **Physical Review B**, 80, 132104-1 – 132104-4, 2009
2. Lim, T. C. Auxetic Materials and Structures. **Engineering Materials series**, Springer, 2015.
3. Yang, L. Cormier, D. West, H. Harryson, O. Knowlson, K. Non-stochastic Ti-6Al-4V foam structures with negative Poisson's ratio. **Materials Science & Engineering A**, v. 558, p. 579–585, 2012.
4. Wang X.-T., Wang B., Li X.-W., Ma L, Mechanical properties of 3D re-entrant auxetic cellular structures, **International Journal of Mechanical Sciences**, accepted, 2017.
5. Nedomová, S. Severa, L. Buchar, J. Trnka, J. Stoklasová, P. Study of Hen's eggs behavior under impact loading, **Nova Science Publishers**, 2011.

3. 2019

Poster and oral presentation at XVIII SBPMat:

OPTIMIZATION OF Ti-6Al-4V AUXETIC STRUCTURES

Ruben Acevedo^{1,2}, Radek Kolman², Marcio C. Fredel¹, Edson C. Santos³

¹Universidade Federal de Santa Catarina (*Engenharia mecânica*),

²Thermomechanics Institute of the Czech Academy of Sciences, ³Zeiss

Abstract

Normally, the majority of materials have a Poisson's coefficient between 0.2 and 0.4. Poisson's coefficient is a non-dimensional ratio defined as the fraction between longitudinal elongation and lateral compression after a uniaxial traction effort.

This coefficient allows the characterization of matter contraction perpendicular to the applied effort direction [1]. Considering only isotropic materials, the values for this elastic constant are comprised in the $[-1, 0.5]$ interval. The maximum value of ν is 0.5 and it corresponds to the case of an incompressible material (natural rubber) while that the case $\nu = 0$ corresponds to a very little or zero lateral expansion after a compression effort, as it is observed for cork.

Nevertheless, there is a class of materials which present a negative Poisson ratio, those are called auxetic (first introduced by Evans), derived from the Greek word *auxetikos*, defined as "that which tends to increase". Auxetic behavior can be either intrinsic or obtained by several re-entrant geometries [2]. These geometries can also be extended in 3D.

In this study, an auxetic geometry was chosen, especially due to its easiness in parametrization and promising early simulation results. Elastic behavior of this structure has been studied in [3,4].

The major objective of this contribution is to optimize four structure parameters: L, H, W, and Θ . Two optimal solutions are pre-defined: 1) Minimal stiffness with minimal mass; 2) Maximal stiffness with minimal mass. Besides, the correlation between geometric parameters will be established. Finally, the effect of these parameters in Poisson's ratio will be observed.

To implement simulations and analysis, a Finite Element Method is used for prediction of mechanical behavior of the auxetic structure.

4. 2020

RESIDUAL STRESS ANALYSIS OF ADDITIVE MANUFACTURING OF METALLIC PARTS USING ULTRASONIC WAVES: STATE OF THE ART REVIEW

Acevedo, R^{1,2,*}. Sedlak, P². Kolman, R². Fredel, M¹.

¹Universidade Federal de Santa Catarina (*Engenharia mecânica*),
²Thermomechanics Institute of the Czech Academy of Sciences, ³Zeiss

Abstract

Additive manufacturing has become a major growing field in materials engineering, following a new tendency for custom, high precision and on-demand fabrication. Residual stresses are prone to appear in any production technique, which remain a challenge to be measured. These stresses can lead to a reduction on mechanical performance and even cause premature failure. Thus, a wide understanding of residual stress is critical for greater part reliability. Among Non-destructive Testing (NDT) techniques, acoustic and ultrasonic waves remain widely used to determine stresses, voids and defects in a wide array of parts. In this contribution, Ultrasonic Testing (UT) is highlighted as an alternative for measuring residual stress both during and after fabrication.

Keywords: Residual stress (RS), Additive Manufacturing (AM), Non-destructive Testing (NDT), Ultrasonic testing (UT)

II. RESIDUAL STRESS MEASUREMENT TECHNIQUES FOR Ti-6Al-4V PARTS FABRICATED USING SELECTIVE LASER MELTING: STATE OF THE ART REVIEW

Ruben Acevedo^{1,2}, Klaudia Kantarwska³, Edson C. Santos⁴, Marcio C. Fredel¹

¹Universidade Federal de Santa Catarina (*Engenharia mecânica*),

²Thermomechanics Institute of the Czech Academy of Sciences,

³University of Poznan

⁴Zeiss

Abstract

Residual stresses (RS) are self-equilibrating internal forces, originating from local differences among plastic strains, induced during thermal or mechanical processes. Due to their large thermal gradients, thermal RS are commonly seen in welded structures and additive manufactured parts. These stresses can lead to reduced mechanical performance, distortion, and even premature part failure; therefore, understanding and characterizing RS is important for improving part reliability. Over the years, different methods have been developed to measure residual stresses of components fabricated using different manufacturing processes. This paper provides a review of techniques used for measuring RS, indicating limitations, advantages, and disadvantages of each method in the case of Ti-6Al-4V components fabricated by Selective Laser Melting.

Keywords: Residual Stresses (RS), Additive Manufacturing (AM), Selective Laser Melting (SLM), Ti-6Al-4V.

Accepted at Rapid Prototyping Journal (RPJ) in June 2020.

Doi: 10.1108/RPJ-04-2019-0097